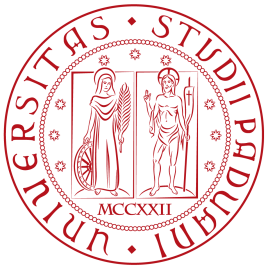

UNIVERSITÀ DEGLI STUDI DI PADOVA

Dipartamento di Fisica e Astronomia “Galileo Galilei”

Master’s Degree in Astrophysics and Cosmology

Final Dissertation

Space-Based Orbit Determination Using Passive Optical Measurements in LEO

Thesis Supervisor
Prof. Stefano Casotto

Candidate
Juan Felipe Cabrera Garcia

Academic Year 2023/24

Para Maria Beatriz, Ismael & Sofia Beatriz

Acknowledgments

I would like to begin by thanking my supervisor, Stefano Casotto, for giving me the opportunity to immerse myself in the field of astrodynamics and for guiding me through this project. His encouragement helped me overcome every obstacle that the research presented. For the valuable discussions regarding instrumentation and astrometry, I would like to thank Davide Greggio and Domenico Nardiello.

I would like to thank my parents and my sister for continuing to fill me with their love, even from a long distance.

To my flatmates, Kseniia, Mattia, Matteo, Margherita, and Demi, I thank you for giving me a home in Padova.

Finally, to my friends Juan Manuel, Daniela, Andres, Valentina C., Valentina L., Camilo, and Sofia, I thank you for giving me the most beautiful memories of this adventure.

Abstract

The increasing number of artificial objects placed in Low Earth Orbit (LEO) has created the need for improvement in the present Space Surveillance and Tracking (STT) systems, which perform Orbit Determination (OD) to estimate their trajectories. Special interest has been developed on passive optical Space-Based Space Surveillance (SBSS), since the proximity to the targets and the non-dependence to atmospheric effects, offer advantages in terms of the measurement quality and the variety of detectable objects. In this work, a passive optical SBSS satellite with a field of view (FOV) of $4^\circ \times 4^\circ$ is simulated. Focusing on Low Earth Orbit (LEO), the Starlink mega constellation is used as a test sample. A Sun-Synchronous Orbit (SSO), 100 km below the targets, is found to be the optimal orbit for their observation. The Gaussian Initial Orbit Determination (IOD) method is implemented, confirming its accuracy when dealing with purely Keplerian orbits, but showing its weakness by being highly sensitive to perturbations and measurement errors. A Weighted Least Squares (WLS) fit using a batch processor, is sought as an alternative. Considering orbits generated by a zonal geopotential with terms up to J_6, fitting a J_2 model to data perturbed by noise at the typical measurement error levels, produced estimation errors of the order on 10 km in position. The inclusion of additional observations, either following the initial set or after half an orbit, reduces the errors to a safer 5 km level. The uncertainty of the estimations is propagated with the covariance matrix, finding that a minimum of 9 measurements is required for a confident interception of the target by the observer's FOV after half an orbit, to produce a follow-up measurement.

Contents

1 Introduction

Understanding celestial motion has been sought by humankind since the earliest civilizations. For centuries, observations of the positions of different celestial bodies in the sky were recorded in order to create models that would describe their behavior. In the beginnings of the 17th century, Johannes Kepler analyzed the detailed observations of Tycho Brahe to provide an interpretation of planetary motion that marked the foundations of our current understanding of orbits. His work, later allowed Isaac Newton to formulate the mathematical description of celestial mechanics, which served as the basis for the field of orbit determination (OD).

The initial use of observations to determine an object's orbit was for bodies of the Solar System, but as time progressed, OD started to be required for both natural and artificial objects, i.e. resident space objects (RSOs). With RSOs orbiting the Earth, a special interest has been developed. The thrive of mega constellations such as Starlink has contributed to a surge in the number of satellites in orbit in the recent years. With this increased activity, space debris are introduced increasing the number of RSOs, and further raising the risk of collisions. This situation has produced the need for improving Space Surveillance and Tracking (SST)* systems which are in charge of detecting, tracking, and cataloging RSOs.

*Which is part of Space Situational Awareness (SSA).

Apart from the traditional astrometry, OD can be conducted with methods such as radio measurements, radar tracking and laser ranging which acquire the range to an object and its rate of change. Additionally, objects equipped with a Global Navigation Satellite System (GNSS) receiver can benefit from precise OD by using this technology. However, optical astrometrical measurements remain the cheapest alternative, and allow the detection of RSOs independently of their characteristics, as long as they reflect sunlight. Although OD procedures have commonly been conducted from the ground (i.e. ground-based), there is a growing interest in space-based OD. Space-Based Space Surveillance (SBSS), specifically optical SBSS, presents certain advantages over other methods, as mentioned by Utzmann and Wagner [1]. Some of them are:

- The ability to take measurements independently from the weather conditions, atmospheric effects and the time of the day.
- Coverage of all orbital regimes.
- The scalability of the system by using multiple observers in a constellation, allowing more coverage and redundancy.
- The possibility of in-situ measurements, enabling the detection of small targets such as space debris.

In this research, we focus our attention on the Low Earth Orbit (LEO) regime, which is bound by 2,000 km in altitude and includes the largest concentration of RSOs. As an interesting example, we focus on the Starlink mega constellation as targets for a SBSS optical telescope. We research the use of passive[†] optical space-based measurements, for this purpose.

The objective of this thesis is to describe a passive optical observation platform aimed at surveying and tracking targets on LEO, more specifically on the orbital shells of the Starlink constellation, and to understand its accuracy and precision limits. We do this by simulating the detection of the targets and their OD. Simulations are done using FORTRAN with the exception of the Gauss method which is implemented in MATLAB. Given the low availability of space-based images of LEO RSOs, the use of simulations is required. Measurements are taken as the results of analyzed images, leaving the study of image reduction and processing as future work.

[†]The word passive is used to avoid confusions with active, optical laser ranging measurements.

1.1 Context

Space-based optical OD has been developed since the 1990s. In their paper, Zhang et al. [2] recount some of the main missions that have been launched for this purpose. One of the earliest example is the Midcourse Space Experiment (MSX) satellite, launched by the United States, which incorporated the Space-Based Visible (SBV) [3] camera with a field of view (FOV) of $1.4° \times 5.6°$. Its success was followed in 2010 by the also American Space-Based Surveillance System (SBSS) satellite [4], which increased the FOV to $3° \times 3°$. A further American development was the Space-based Telescopes for the Actionable Refinement of Ephemeris (STARE) [5], which was launched into polar orbit and had a FOV of $2.08° \times 1.67°$. Apart from the American initiatives, Canadians have launched three successful platforms. The Microvariability and Oscillations of Stars (MOST) satellite [6], Sapphire [7], and Near-Earth Orbit Surveillance Satellite (NEOSSat) [8], all with similar FOVs to the SBV. An example image taken by NEOSSat is shown in Figure 1.1, where its colleague Sapphire is shown in conjunction with the Orbcomm 35 satellite. As evidenced from the Figure, the high relative velocity between the observer and the target results in the formation of a streak that depicts the target's motion. From this, the only positions that can be associated to a moment in time, are the edges of the streak. As we will see, all the measurements that we will propose in this work, will be done for the edges of streaks. Studies of the detection and analysis of streaks for this purposes have been conducted by Virtanen et al. [9].

Proposals for future passive optical SBSS have been developed, from which we highlight the ESA VISDOMS (Verification of In-Situ Debris Optical Monitoring from Space) with its instrument the Space-Based Optical Component (SBOC) [10]. Additionally, one of the most interesting private initiatives is the development of the FLAMINGO constellation by the German company Vyoma [11].

Relevant previous works regarding the use of passive optical SBSS have been published by Scire et al. [12] and Stechowsky et al. [13]. While proposals of using the already onboard star trackers in satellites for SBSS have been done by Spiller et al. [14].

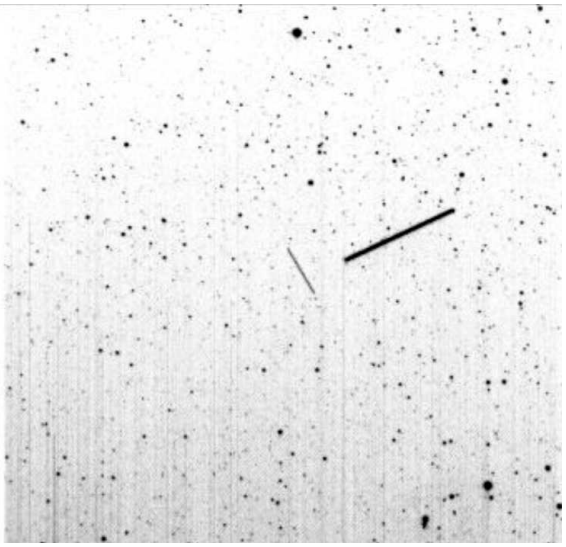

Figure 1.1: NEOSSat image. 1 second exposure of a conjunction between Sapphire and Orbcomm 35, taken from [8].

1.2 Thesis Structure

This work presents the following structure:

- Chapter 2 describes the modeling of the observer and the target's orbits and discusses the constraints used to simulate target detections.
- Chapter 3 shows the description of the Starlink constellation as a sample target for our simulations.
- Chapter 4 details the process of designing the observer's orbit and pointing direction in order to satisfy our requirements.
- Chapter 5 discusses the use of classical Initial Orbit Determination (IOD) methods, in particular the Gauss method, used in our simulations.
- Chapter 6 expands the study to Statistical Orbit Determination (SOD) by considering a batch processor to implement a Weighted Least Squares (WLS) method.
- Chapter 7 presents the conclusions of the research and suggests future work.

2

Simulations of the Observations

In order to simulate our space-based optical observations, we must begin with the modeling of the orbits of both the observed object and the observer. From here, we can build the tools to establish how the observer would visualize the objects. In this chapter, we describe two methods for modeling orbital motion of our objects, then we establish a set of constraints indicating when a given target can be seen and measured astrometrically by the observer, and finally we comment on how angular measurements are handled based on the reference frame in which they are taken.

2.1 Orbits Dynamical Modeling

We describe two models for propagating the orbital states of our objects of interest. Traditional integration of the equations of motion will serve as our main tool for describing the motion of our objects. We will consider a geopotential including the first six zonal terms, which play the most important perturbations of a classical Keplerian orbit. Additionally, we will employ Simplified General Perturbations-4 (SGP4) the analytical propagator that allow us to propagate multiple trajectories from available two-line element sets (TLEs). The latter method is useful because it allows quicker propagation of multiple objects which are useful to analyze the effectiveness of a given proposed observer at measuring a large population of targets.

2.1.1 Equations of Motion with zonal perturbations

The equations of motion are described by the following expression

$$\dot{\mathbf{X}}(t) = \mathbf{F}(\mathbf{X}(t)), \tag{2.1}$$

with $\mathbf{X}(t)$ being the state vector, given by position $\mathbf{r}$ and velocity $\dot{\mathbf{r}}$, and $\mathbf{F}$ the force model.

$$\mathbf{X}(t) = [\mathbf{r}(t), \dot{\mathbf{r}}(t)]^\top \tag{2.2}$$

$$\mathbf{F}(\mathbf{X}) = \left[\dot{r}_i, \dot{r}_j, \dot{r}_k, \frac{\partial U(\mathbf{r})}{\partial r_i}, \frac{\partial U(\mathbf{r})}{\partial r_j}, \frac{\partial U(\mathbf{r})}{\partial r_k}\right]^\top. \tag{2.3}$$

U stands for the gravitational potential, and we will follow the steps described by Casotto [15] to define it. When handling a point with mass M, U takes the classical Newtonian form of

$$U = \frac{GM}{\Delta}, \tag{2.4}$$

where G is the gravitational constant and Δ the distance between the object's location and the point mass source. Aided by the illustration in Figure 2.1, the distance can be written as $\Delta = \sqrt{r^2 - 2rr'\cos\gamma + r'^2}$. The reciprocal distance, can then be expressed in terms of spherical harmonics Y_n^m and Y_n^{m*}

$$\frac{1}{\Delta} = \frac{1}{r}\sum_{n=0}^{\infty}\sum_{m=-n}^{n}\frac{4\pi}{2n+1}\left(\frac{r'}{r}\right)^n Y_n^m(\theta,\varphi)Y_n^{m*}(\theta',\varphi'). \tag{2.5}$$

We seek to obtain the potential generated by an extended source, so we must integrate equation 2.4 on the volume V occupied by the body of mass

$$U(r,\theta,\varphi) = G\iiint_{V'}\frac{dM'}{\Delta} = \frac{G}{r}\sum_{n=0}^{\infty}\sum_{m=-n}^{n}\frac{4\pi}{2n+1}Y_n^m(\theta,\varphi)\iiint_{V'}\left(\frac{r'}{r}\right)^n Y_n^{m*}(\theta',\varphi')dM'. \tag{2.6}$$

Introducing the Stokes coefficients $K_{nm} = K_{nm}^c + iK_{nm}^s$ which encompass the triple integral of the spherical harmonics, we reduce our expression to

$$U(r,\theta,\varphi) = \frac{GM}{r}\sum_{n=0}^{\infty}\sum_{m=-n}^{n}\left(\frac{a_e}{r}\right)^n K_{nm}Y_n^m(\theta,\varphi), \tag{2.7}$$

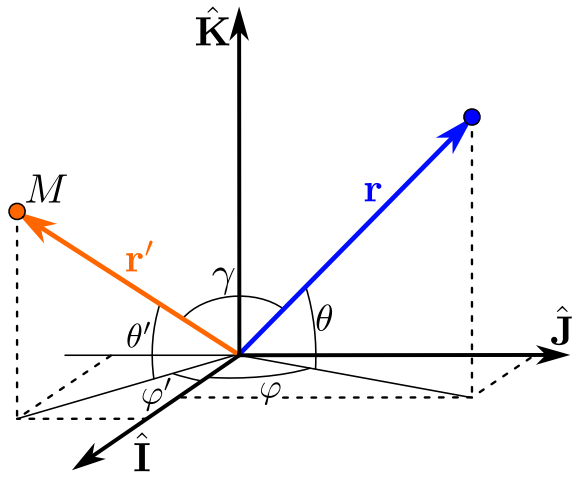

Figure 2.1: Vector representation of a point-like mass and a point in space experiencing its gravitational pull. Angles are defined with respect to the axes on the reference frame which in our case is defined as inertial since we assume Earth as axially symmetric and ignore its rotation. Angle γ used to obtain the distance Δ is formed by both position vectors.

where a_e is the scale factor representing the typical size of the body, in our case the average Earth radius. From here, we use the real-valued Stokes coefficients defined with $m \geq 0$

$$C_{nm} + iS_{nm} = (2 - \delta_{0m})N_n^m K_{nm}, \tag{2.8}$$

and the spherical harmonics represented with the associated Legendre polynomials P_n^m

$$Y_n^m(\theta, \varphi) = N_n^m e^{im\varphi} P_n^m(\sin\theta), \tag{2.9}$$

where both expressions have N_{nm} as a normalization factor. We then rewrite expression 2.7 as

$$U(r, \theta, \varphi) = \frac{GM}{r} \sum_{n=0}^{\infty} \sum_{m=0}^{n} \left(\frac{a_e}{r}\right)^n (C_{nm} \cos m\varphi + S_{nm} \sin m\varphi) P_n^m(\sin\theta). \tag{2.10}$$

Now, by approximating the Earth as symmetric along its rotation axis, or in other words assuming a zonal potential, we further reduce our expression by taking $m = 0$ to

$$U(r, \theta, \varphi) = \frac{GM}{r} \sum_{n=0}^{\infty} \left(\frac{a_e}{r}\right)^n C_{n0} P_n(\sin\theta), \tag{2.11}$$

we then adopt $J_n = -C_{n0}$ to get

$$U(r,\theta,\varphi) = \frac{GM}{r}\left\{1 - \sum_{n=1}^{\infty} J_n \left(\frac{a_e}{r}\right)^n P_n(\sin\theta)\right\}, \tag{2.12}$$

where we used the fact that $J_0 = -1$. Additionally, knowing that $J_1 = 0$, we can write the zonal potential up to J_2 which dominates over the higher order terms:

$$U(r,\theta,\varphi) = \frac{GM}{r}\left\{1 - J_2\left(\frac{a_e}{r}\right)^2\left(\frac{3}{2}\sin^2\theta - \frac{1}{2}\right)\right\}. \tag{2.13}$$

This expression can be easily written in Cartesian coordinates

$$U(\mathbf{r}) = \frac{GM}{r}\left\{1 - J_2\frac{a_e^2}{r^3}\frac{1}{2}(3r_k^2 - r^2)\right\}, \tag{2.14}$$

and then we can obtain the partial derivatives

$$\begin{aligned}
\frac{\partial U}{\partial r_i} &= -\frac{GMr_i}{r^3}\left\{1 + \frac{3}{2}J_2\left(\frac{a_e}{r}\right)^2\left(1 - 5\left(\frac{r_k}{r}\right)^2\right)\right\} \\
\frac{\partial U}{\partial r_j} &= -\frac{GMr_j}{r^3}\left\{1 + \frac{3}{2}J_2\left(\frac{a_e}{r}\right)^2\left(1 - 5\left(\frac{r_k}{r}\right)^2\right)\right\} \\
\frac{\partial U}{\partial r_k} &= -\frac{GMr_k}{r^3}\left\{1 + \frac{3}{2}J_2\left(\frac{a_e}{r}\right)^2\left(3 - 5\left(\frac{r_k}{r}\right)^2\right)\right\}.
\end{aligned} \tag{2.15}$$

This J_2 model is simple enough to produce a rapid fit of a target's orbit as it will be described later on chapter 6. Nevertheless, for a more complete simulation of the the target's *true* orbit, we wish to include more terms of the expansion on equation 2.12. When including six zonal terms, the partial derivatives on 2.15, which is what we essentially need for the integration, are written in vector form as

$$\frac{\partial U}{\partial \mathbf{r}} = -\frac{GM}{r^3}\mathbf{r} + \sum_{n=2}^{6} \mathbf{a}_{J_n}, \tag{2.16}$$

where the expressions for the $\mathbf{a}_{J_n}$ coefficients, taken from Shaub and Junkins [16], are shown in Appendix A.

In order to obtain an object's trajectory, the integration of the equations of motion given

by 2.1 is performed numerically using the Shampine and Gordon ODE Solver [17]. The gravitational constants used for integrating come from the JGM-3 model [18] and are summarized on table 2.1.

Constant	**Value**
GM	$398,600.4415\ \mathrm{km}^3/\mathrm{s}^2$
a_e	6378.1363 km
J_2	1.0826360×10^{-3}
J_3	$-2.5324353 \times 10^{-6}$
J_4	$-1.6193312 \times 10^{-6}$
J_5	$-2.2771610 \times 10^{-7}$
J_6	5.3964849×10^{-7}

Table 2.1: Gravitational parameters used for the numerical integration of the force model as given by the JGM-3 Earth geopotential model [18].

2.1.2 SGP4

To efficiently model the dynamics of multiple objects in orbit, we choose the Simplified General Perturbations (SGP) models, specifically the refined Simplified General Perturbations-4 (SGP4) propagator, which is used to estimate position and velocity of near-Earth orbiting objects. The SGP models were initially developed in the 1960's based on Lane's drag theory [19], SGP4 was originally introduced by K. Cranford as stated by Lane and Hoots (1979) [20] and it was released for FORTRAN IV on *Spacetrack Report No.3* (1980) [21]. The model incorporates Brouwer's solution for the motion of near-Earth Satellites under a geopotential that considers the zonal harmonics J_2, J_3, J_4, and J_5 [22], but SGP4 presents a series of simplifications with respect to the original SGP. These are namely retaining only the long- and short-periodic terms in position that do not contain eccentricity as a factor, and only the main terms that modeled the secular effect of drag [23]. For this work we use a more recently revised version of SGP4, published by D. Vallado et al. (2006) [24], on it the user may choose the desired standards of Earth's gravitational constants. The WGS-84 version, described in Table 2.2 is selected for this work, when running SGP4.

Constant	Symbol	Value
Gravitational constant	μ	$398,600.5\ \mathrm{km}^3/\mathrm{s}^2$
Earth's radius	$R_\oplus$	6378.136 km
Zonal terms	$\bar{C}_2$	-0.4841685×10^{-3}
⋮	$\bar{C}_3$	0.95706390×10^{-6}
⋮	$\bar{C}_4$	0.53699587×10^{-6}

Table 2.2: WGS-84 constants. The WGC-84 standard constants released by the World Geodetic System committee on 1984 [25].

TLEs

SGP4 is compatible with the North American Aerospace Defense Command (NORAD) element sets, better known as TLEs. This format, also dated to the initial development of the SGP models, encodes the orbital state of an object by providing ten values. Six of them, written on the second line, represent classical orbital elements: inclination (i), right ascension of the ascending node (Ω), eccentricity (e), argument of the perigee (ω), mean anomaly (M), and mean motion ($\bar{n} = \sqrt{\mu/\bar{a}^3}$) which contains the mean semi-major axis ($\bar{a}$)*. The first line contains three more values required to describe the effects of perturbations on the motion, which are: mean motion rate ($\dot{n}/2$), mean motion acceleration ($\ddot{n}/6$), and a drag parameter (B^*)†. Time is included in UTC format and additional fields are reserved for the object's and observation's identification. An example TLE with the description of its fields is shown in Figure 2.2.

Card#	Satellite Number	Class	International Designator	Yr	Epoch Day of Year (plus fraction)	Mean Motion Rate (rev/day/2)	Mean Motion Acceleration (rev/day²/6)	B* (/Earth Radius)	Eph	Elem Num	Chk Sum
			Yr Lch# Piece			S	S S E	S. S E			
1	44713	U	19074A	24074.35538811		.00000160 3	00000+0	86230-4	0	999 7	
Card#	Satellite Number		Inclination (deg)		Right Ascenssion of Ascending Node (deg)	Eccentricity	Argument of Perigee (deg)	Mean Anomaly (deg)	Mean Motion (rev/day)		Epoch Rev	Chk Sum
2	44713		53.0510		202.7679	0001240	93.1757	266.9374	15.06402460		23942	2

Figure 2.2: TLE Structure. Example of a two line element set from a StarLink satellite. Downloaded from `https://celestrak.org/NORAD/elements/`.

*We should clarify that in fact all the values presented are mean, not only $\bar{a}$.

†$B^* = \frac{1}{2}\frac{c_D A}{m}\rho_0 R_\oplus$, with ρ_0 as the atmospheric density at perigee, c_D the drag coefficient, A the cross-sectional area, and m the mass.

Precision and Accuracy

It is convenient to discuss the actual limitations of SGP4 propagation in terms of its precision and accuracy. To begin, by simply considering the structure of the TLE data (see Figure 2.2) we can identify the limitations of the amount of decimal places chosen to describe each element. As discussed by Vallado [26], the time epoch is given with eight decimal places, eccentricity with seven and all the angles with four. The epoch then has an uncertainty of $\pm 4.3 \times 10^{-4}$ s which for LEO satellites travelling at ~ 7 kms^{-1} translates in to a position uncertainty of $\sim \pm 3$ m. The eccentricity's uncertainty introduces errors in position under the meter for LEO but around 2 m for GEO ($\Delta r \approx a\Delta e$). Lastly, the limitation of four decimal places in the angles (i.e. $i,\ \Omega,\ \omega,$ and M) would introduce an uncertainty at epoch of 6 m for LEO and up to 35 m for GEO.

Regarding SGP4's ability to predict orbits accurately, we can refer to a study published by Kelso on 2007 [27], where SGP4 propagation is compared to precision ephemerides of the GPS constellation (see Figure 2.3a). The errors are presented for each dimension on the RTN (Radial, Along-track, Cross-track) coordinate system of the reference trajectory. An additional consistency analysis of the TLEs is done by comparing them to their own predictions using SGP4 (see Figure 2.3b). Some of the results are seen in Figure 2.3, where it is clearly seen that the error is dominated by the along-track component. A clear bias is also present in the errors and according to the paper, the bias differs from case to case. The accuracy of the propagation in general remains within the 10 km of error, and the consistency of the TLEs under SGP4 is lost after propagating to far from the epoch. However, for simulation purposes, the use of TLE's and SGP4 remains self consistent if propagations remains close to the epoch. Specifically a 2 day window centered on the epoch shows sufficiently low error.

2.1.3 Coordinate transformation

SGP4 uses a "True Equator Mean Equinox" (TEME) coordinate system. This results inconvenient when relating the results of the propagator to external data, and general applications require transforming the coordinates to a standard Earth-centered inertial (ECI) system. The Geocentric Celestial Reference System (GCRS) is the current standard for near-Earth objects, and it uses axes which are very close to the frame of Fundamental Katalog 5 (FK5) J2000. The transformation of a vector from TEME to J2000 requires

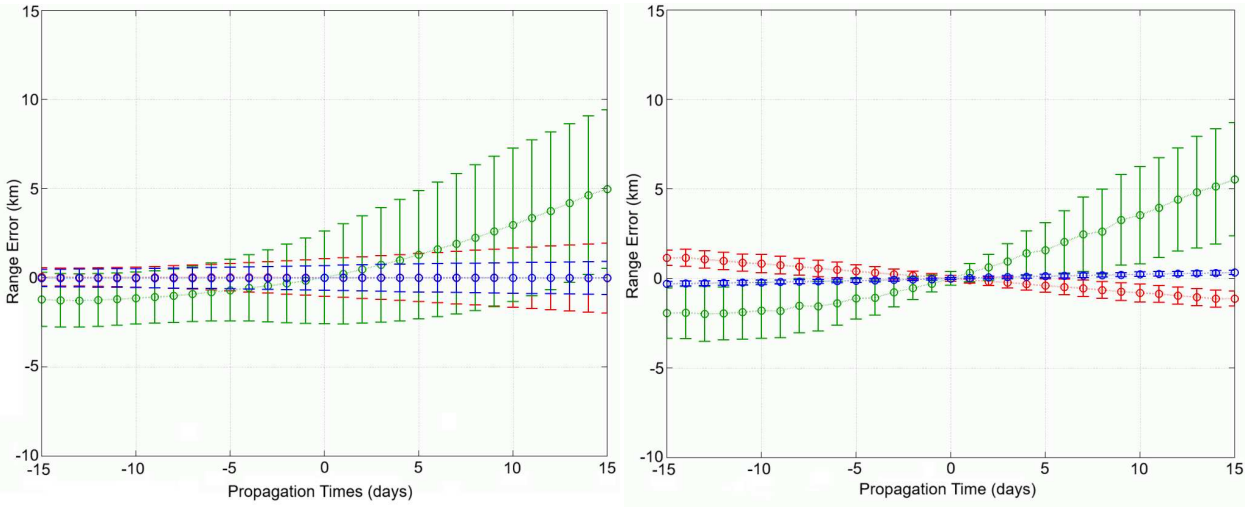

(a) SGP4 compared to true trajectory.

(b) TLEs consistency under SGP4.

Figure 2.3: SGP4 Validation. Taken from Kelso [27]. Data for GPS satellite PNR28, radial errors are shown in red, along-track errors in green, and cross-track errors in blue. **(a)** Average errors of SGP4 with respect to the true orbit, obtained from the precise ephemerides of the GPS constellation. **(b)** Average errors of propagating each TLE $\pm$ 15 days and comparing these results to the TLEs at the respecting epoch.

3 steps which are illustrated in Figure 2.4: rotating to True of Date (TOD), multiplying by the nutation matrix to get to Mean of Date (MOD), and multiplying by the precession matrix. The explanation of the set of rotations will be made with the convention of **ROT1**, **ROT2**, and **ROT3** representing rotations about the X, Y, and Z axes respectively.

Following indications given by Seago and Vallado [28], the TOD frame is related to TEME by the Equation of the Equinoxes ($Eq_{Equinox}$) but the kinematic correction is not considered, leaving only the geometric interpretation. So $Eq_{Equinox} \approx \Delta\Psi \cos(\varepsilon)$, where $\Delta\Psi$ is the nutation in longitude, and ε the obliquity given by its mean value plus its nutation ($\varepsilon = \bar{\varepsilon} + \Delta\varepsilon$), and the transformation is the following

$$\mathbf{r}_{TOD} = \mathbf{ROT3}(-Eq_{Equinox})\mathbf{r}_{TEME} \tag{2.17}$$

The MOD frame is related to TOD by the nutation matrix which is built by the following rotations

$$[\mathbf{N}] = \mathbf{ROT1}(-\bar{\varepsilon})\mathbf{ROT3}(\Delta\Psi)\mathbf{ROT1}(\varepsilon) \tag{2.18}$$

Finally, the MOD differs from the standard GCRS by the precession matrix, defined

by the precession angles ζ, Θ, and z, applied on the following rotations

$$[\mathbf{P}] = \mathbf{ROT3}(\zeta)\mathbf{ROT2}(-\Theta)\mathbf{ROT3}(z) \tag{2.19}$$

The final transformation is

$$\mathbf{r}_{J2000} = [\mathbf{P}][\mathbf{N}]\mathbf{ROT3}(-Eq_{Equinox})\mathbf{r}_{TEME} \tag{2.20}$$

On this work, the nutation angles are obtained from the IAU 1980 nutation model while the IAU 1976 model provides the precession matrix[‡].

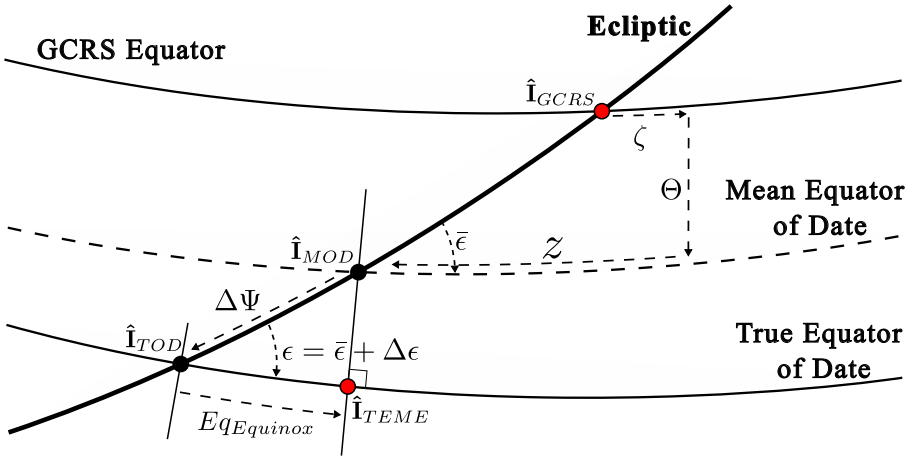

Figure 2.4: TEME Coordinate System. Geometry of the "True Equator Mean Equinox" (TEME) and angles that relate it to the True of Date (TOD), Mean of Date (MOD) and GCRS frames.

2.2 Observations Modeling

After understanding how to model both observer and target object's orbit via the propagation of TLEs with SGP4, and transforming the output to standard coordinates, we end up with the ephemerides that describe timelines of our objects' state vectors evolution in a proper reference frame. With this in hand we may proceed to understand how a target object can be "seen" by the observer, first from a geometric point of view, and then by the apparent brightness/magnitude received by the observer.

[‡]Subroutines `iau_NUTM80` and `iau_PMAT76` from the SOFA Software Collection [29], are implemented.

2.2.1 Target's Geometric Visibility

From a geometric perspective, the visibility of a target object by the observer requires two basic conditions. The presence of the target inside the observer's field of view (FOV), and the existence of a clear line of sight (LOS) between the observer and the target.

The Field of View

The simplest approach is to consider a FOV with the shape of a cone, defined by an observing direction ($\hat{\mathbf{O}}$) and a FOV size, which we measure with the angular radius of the cone (θ_{FOV}). Given the position vectors of the observer ($\mathbf{r}_{obs}$) and the target ($\mathbf{r}_{tar}$), we can define our LOS vector, which can also be referred as range vector ($\boldsymbol{\rho} = \mathbf{r}_{tar} - \mathbf{r}_{obs}$). Determining when the target is in the observer's FOV is then done by calculating the angle between $\hat{\mathbf{O}}$ and $\boldsymbol{\rho}$, which we define as θ, and comparing it to θ_{FOV}. With Figure 2.5 to illustrate, the FOV condition is given by the following expression

$$\begin{aligned} \theta &= \arccos \frac{\hat{\mathbf{O}} \cdot \boldsymbol{\rho}}{|\boldsymbol{\rho}|} \\ \text{inside FOV}(\theta) &= \begin{cases} \mathit{True} & \theta < \theta_{FOV} \\ \mathit{False} & \theta \geq \theta_{FOV} \end{cases} \end{aligned} \tag{2.21}$$

Line of Sight

In order to have a clear LOS between the observer and the target, we must reassure that the Earth does not occult them. To verify this we consider a spherical Earth, and define its radius as $R_{\oplus}$ from which we calculate its angular radius ($\theta_{\oplus}$) as seen by the observer. The angular separation between the LOS ($\boldsymbol{\rho}$) and the observer to Earth vector ($-\mathbf{r}_{obs}$), which we label $\theta_{T\oplus}$, is then compared to $\theta_{\oplus}$. All these calculations are simplified due to the fact that we use a geocentric reference frame. The following procedure is illustrated in Figure

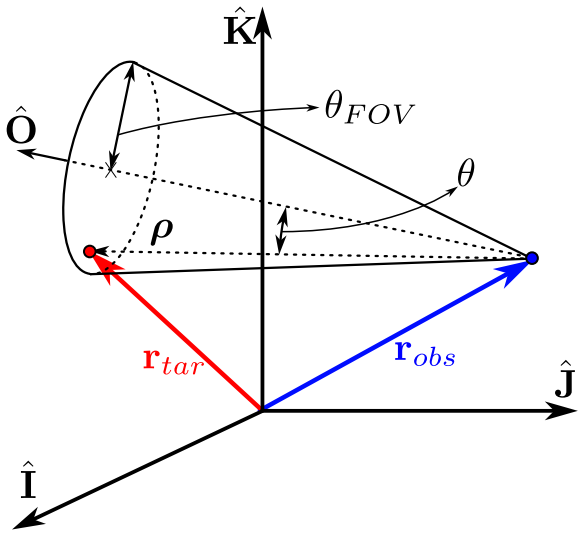

Figure 2.5: FOV geometry. Position vectors for the observer and target are drawn in blue and red respectively. The LOS vector is also shown which in this case is inside the cone that defines the FOV, along its direction $\hat{\mathbf{O}}$ and aperture θ_{FOV}. "θis the angle between the LOS and $\hat{\mathbf{O}}$. FOV condition is described in equation 2.21

2.6.

$$\begin{aligned} \theta_{\oplus} &= \arcsin \frac{R_{\oplus}}{|\mathbf{r}_{obs}|} \\ \theta_{T\oplus} &= \arccos \frac{-\mathbf{r}_{obs} \cdot \boldsymbol{\rho}}{|\mathbf{r}_{obs}||\boldsymbol{\rho}|} \\ \text{Occultation}(\theta_{T\oplus}, \theta_{\oplus}) &= \begin{cases} True & \theta_{T\oplus} \leq \theta_{\oplus} \\ False & \theta_{T\oplus} > \theta_{\oplus} \end{cases} \end{aligned} \tag{2.22}$$

Although the premise of the occultation function is to detect when the Earth gets in the way of our line of sight, cases when the target is seen by the observer with the Earth as background are also detected with our function serving the correct purpose. This being since in practice the measurements require a star background and the presence of Earth´s reflecting brightness on the frame would hinder the observation.

2.2.2 Exclusion Angles

Given the optical nature of our observations, we use optical sensors (e.g., CCDs) that would get saturated when pointed towards the Sun, the Earth, the Moon or other bright

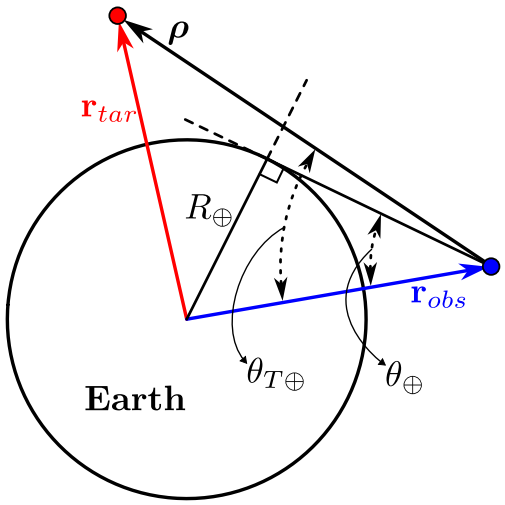

Figure 2.6: Occultation. Position vectors for the observer and target are drawn in blue and red respectively. The geometrical description of angles $\theta_{T\oplus}$ and $\theta_\oplus$ is shown. The occultation condition is described in equation 2.22.

sources. For this reason, the specifications of the optical systems on board establish the so called exclusion angles to define the minimum angular distance that exist between our LOS with the target measured and the LOS with the bright source.

Solar Exclusion Angle

The angle between the incoming sunlight direction (**S**) and **ρ**, which we label $\theta_{T\odot}$ must have a minimum value ($\alpha_\odot$), which is known as the solar exclusion angle, this depends on the optical system specifications. The expression for the target-observer-sun angle is shown below. An exception to this condition is produced when the observer is eclipsed by the Earth, since it could observe in any direction where the LOS is not obstructed by Earth. The eclipsing of the observer is determined by equation 2.29 with $\mathbf{r}_{obs}$ instead of $\mathbf{r}_{obj}$, an example is shown in Figure 2.7.

$$\theta_{T\odot} = \arccos \frac{-\mathbf{S}\cdot\boldsymbol{\rho}}{|\boldsymbol{\rho}||\mathbf{S}|} \geq \alpha_\odot \tag{2.23}$$

Terrestrial Exclusion Angle

Following the same principle of the sun, the sunlight reflected by the Earth is to be avoided in our measurements. Since we have already restricted our observations to have a star

background in Section 2.2.1, our concern now would be what could happen to observations where the target is seen very close to the limb of the Earth, relative to the observer. The inclusion of a terrestrial exclusion angle ($\alpha_{\oplus}$) which has to be measured from the limb of the Earth and determined by the characteristics of the optical system is required. With this consideration we can update the geometric occultation condition stated at the end of equation 2.22

$$\theta_{T\oplus} \leq \theta_{\oplus} + \alpha_{\oplus} \tag{2.24}$$

Naturally fulfilling this condition implies the fulfillment of the previous occultation condition. However, given a case where the Section of the limb of the Earth in question is not illuminated (i.e. experiences night), this condition could be ignored, and the geometric occultation condition would prevail.

Additional Exclusion Angles

A complete simulation requires the consideration of additional exclusion angles due to other bright sources that might be present on the FOV. Other than the solar and terrestrial exclusion angles, lunar, planetary and galactic (which refers to the center of the galaxy as a considerably bright region of the sky) exclusion angles may have to be considered. For simulation purposes, in this project, to the solar and terrestrial counter parts, we will only add the lunar exclusion angle ($\alpha_{\leftmoon}$) to our observing constraints.

2.2.3 Limiting Magnitude

One of the most important considerations for the optical observations is the object's brightness as measured by the observer's detector. Considering our observation being done on the visual band, we quantify brightness with apparent visual magnitude (m_{V}) given by

$$m_{\mathrm{V}} = -2.5 \log_{10} \left(\frac{F_{\mathrm{V}}}{F_{\mathrm{V},0}} \right), \tag{2.25}$$

where F stands for the radiation flux, which is defined as the total energy from the visual band wavelengths that crosses a unit area perpendicular to the direction of incoming light per unit time [30]. The flux on the denominator $F_{\mathrm{V},0}$ refers to the reference flux which would correspond to magnitude 0. Depending on the detector's specification and exposi-

tion time used, a minimum brightness or limiting magnitude, can be detected and creates a new constraint to our observations.

Naturally most RSOs don't emit light on their own, meaning that the observed magnitude results from the reflected sunlight. The reflected brightness given as visual magnitude (m_V) is modeled with the following expression, presented by McCue et al. in 1971 [31]

$$m_{\mathrm{V}} = -26.58 - 2.5 \log_{10} \left(\frac{A\gamma F(\Phi)}{R^2} \right), \tag{2.26}$$

where A is the cross-sectional area, γ the reflectivity, R the distance between observer and target, and $F(\Phi)$ a function related to the object's shape and orientation, that depends on the phase angle Φ (illustrated in Figure 2.7).

$$\Phi = \arccos \frac{\boldsymbol{\rho} \cdot \mathbf{S}}{|\boldsymbol{\rho}||\mathbf{S}|} = 180^\circ - \theta_{T\oplus} \tag{2.27}$$

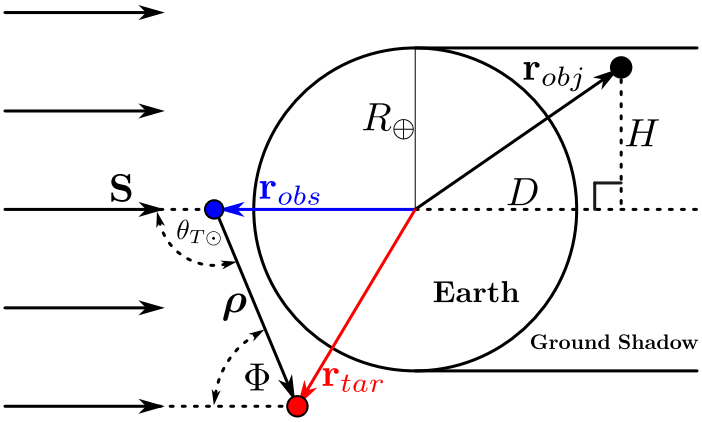

Figure 2.7: Phase Angle and Eclipsing. Position vectors for the observer and target are drawn in blue and red respectively. With the sunlight direction vector **S** and the LOS, we define the phase angle Φ and its complementary angle $\theta_{T\oplus}$, required for the sunlight effect constraint described in Section 2.2.2. The geometry for the eclipsing situation of a generic object is also drawn to illustrate equation 2.29.

The derivation of this expression is straightforward, considering that the reflected light comes from the Sun, hence the inclusion of the Sun's apparent visual magnitude $m_{\mathrm{V},\odot} \approx -26.58$ and the term that diminishes it considering the RSO's size, shape, orientation and material, without forgetting the inverse squared law in relation to the observer's distance.

The phase function $F(\Phi)$ has well known expressions for flat, cylindrical and spherical shapes. A common choice that allows to ignore the modeling of the target´s attitude is the spherical shape. Also by considering a diffuse sphere, the shape of the magnitude-phase curve (see Figure 1 of [31]) resembles the other geometries while keeping a conservative approach. The following is the phase function for a diffuse sphere given by Russell [32].

$$F(\Phi) = \frac{2}{3\pi^2}[(\pi - \Phi)\cos\Phi + \sin\Phi] \tag{2.28}$$

It is necessary to remark that the target clearly requires being hit by sunlight to reflect the radiation that allows it to be visible. Therefore, we must also constraint the observations to when the target is not being eclipsed by Earth. The eclipsing condition, which is also required when considering the exception to the sunlight effect constraint (as mentioned in Section 2.2.2), can be analyzed with a simplified model of the Sun casting a straight ground shadow within which our orbiting objects would be eclipsed. The choice of this simplification comes from the fact that the examples taken on this work are at LEO, and their closeness to Earth makes unnecessary to consider the small time window when the Earth would only partially eclipse the Sun and they would be on the penumbra. The following expressions (also used in [33]) model the ground shadow.

$$\begin{aligned} D &= \mathbf{r}_{obj} \cdot \mathbf{S} \\ H^2 &= |\mathbf{r}_{obj}|^2 - D^2 \\ \text{is eclipsed}(D, H^2) &= \begin{cases} \mathit{False} & D \leq 0 \\ \mathit{False} & D > 0 \text{ and } H^2 \geq R_\oplus^2 \\ \mathit{True} & D > 0 \text{ and } H^2 < R_\oplus^2 \end{cases} \end{aligned} \tag{2.29}$$

Illustration of the geometry is shown in Figure 2.7. Equation 2.29 is written with notation for a generic object, to know if the target is being illuminated by the Sun, $\mathbf{r}_{tar}$ must be taken instead of $\mathbf{r}_{obj}$.

2.2.4 Constraints Summary

To summarize the various constraints presented on this Section regarding a simulated space-based observation, we enumerate them.

1. The target must be inside field of view. Equation 2.21 must be *True*.

2. LOS must be clear from occultation. Equation 2.22 must be *False*.

3. The target must be illuminated by the Sun. Equation 2.29 for $\mathbf{r}_{tar}$ must be *False*.

4. Sunlight effect must not be present on the detector. Relation 2.23 must be *True*, unless equation 2.29 for $\mathbf{r}_{obs}$ is *True*.

5. Other exclusion angle constraints (i.e. terrestrial and lunar) must be respected.

6. Apparent magnitude obtained from equation 2.26 must be under the limiting magnitude of the detector.

2.3 Angular Measurements

We must remember that optical observations can only provide us with reliable information about the angular position of a given target. For this reason, although our simulations directly give the full state vectors, our orbit determination methods must be fed by angles-only data, in order to then obtain the state vectors. In practice, space-based observations can be performed in two ways, first inertial pointing, which involves steering the satellite to point at a certain direction keeping a fixed stellar background. In the other hand, considering satellites which can not be steered, we must have body-fixed pointing, where we consider a satellite body-fixed reference system such as the RTN. On this Section, we explain how to calculate the angular information later used by the orbit determination methods.

2.3.1 Inertial Reference Frame

With inertial pointing, we easily obtain angular measurements in the ECI frame. There are two angles used to describe positions on a spherical projection of the sky in an ECI frame. Declination (δ) measures the angle from the equatorial plane to the object and ranges from $-\frac{\pi}{2}$ to $+\frac{\pi}{2}$, while Right Ascension (α) is the angle eastward along the celestial equator of the object from the March equinox, which in our case is defined by the J2000 Epoch. Traditionally these angles are given degrees, arc-minutes, and arc-seconds for δ, and hours, minutes and seconds for the case of α; however, the calculations below require them both measured in radians. It must be mentioned that although the angles that

we just introduced are defined to be measured from the center of the Earth, in general stellar catalogs give this angles with respect to the barycenter of the solar system, meaning that all Earth-based (or in our case space-based from Earth orbit) measurements that refer to stellar catalogs, require specific corrections.

When observing an object's projection on the celestial sphere from Earth's surface, we use topocentric versions of α and δ labeled with the sub index t, i.e. α_t, δ_t. in our case having space-based observations we consider the sub index s which refers to sensor centered. The values for α_s and δ_s along with their rates $\dot{\alpha}_s$ and $\dot{\delta}_s$ can be easily be calculated from our LOS vector $\hat{\boldsymbol{\rho}} = [\rho_i, \rho_j, \rho_k]^\intercal$ and its rate[§] $\dot{\boldsymbol{\rho}} = [\dot{\rho}_i, \dot{\rho}_j, \dot{\rho}_k]^\intercal$ following this relations

$$\begin{aligned} \alpha_s &= \arctan\left(\frac{\rho_j}{\rho_i}\right) & \delta_s &= \arctan\left(\frac{\rho_k}{\sqrt{\rho_i^2 + \rho_j^2}}\right) \\ \dot{\alpha}_s &= \frac{\rho_i\dot{\rho}_j - \rho_j\dot{\rho}_i}{\rho_i^2 + \rho_j^2} & \dot{\delta}_s &= \frac{\dot{\rho}_k - |\dot{\boldsymbol{\rho}}|\sin\delta_s}{\sqrt{\rho_i^2 + \rho_j^2}} \end{aligned} \tag{2.30}$$

The relative angular velocity of the target with respect to the observer is given by

$$\omega_{Inertial} = \sqrt{\dot{\alpha_s}^2 \cos^2(\delta_s) + \dot{\delta_s}^2} \tag{2.31}$$

2.3.2 Body-Fixed Reference Frame

Similar to topocentric observations, body-fixed observations refer to a local rotating set of axes, centered on the satellite, that define a body-fixed reference frame. In this work we use the RTN frame, defined by a *radial* ($\hat{\mathbf{R}}$) axis, an *along-track* or *transverse* ($\hat{\mathbf{T}}$) axis, and a *cross-track* or *normal* ($\hat{\mathbf{N}}$) direction. Ignoring the *obs* sub index, knowing that $\mathbf{r}$ refers to the observer's state, we have the following

$$\begin{aligned} \hat{\mathbf{R}} &= \mathbf{r}/|\mathbf{r}| \\ \hat{\mathbf{T}} &= \hat{\mathbf{N}} \times \hat{\mathbf{R}} \\ \hat{\mathbf{N}} &= \mathbf{r} \times \dot{\mathbf{r}}/|\mathbf{r} \times \dot{\mathbf{r}}| \end{aligned} \tag{2.32}$$

[§]Defined analogously to $\boldsymbol{\rho}$, by the subtraction of velocities: $\dot{\boldsymbol{\rho}} = \dot{\mathbf{r}}_{tar} - \dot{\mathbf{r}}_{obs}$

On this reference we also define two angles which are analogous to δ and α. Elevation (*el*) is defined analogously to the declination, but concerning the angular distance from the *pseudo* local horizon (i.e. plane formed by $\hat{\mathbf{T}}$ and $\hat{\mathbf{N}}$) to the object. Regarding the azimuth (*Az*), this is the analogue to the right ascension, it is measured from $\hat{\mathbf{T}}$ but in contrast to α, the positive direction is clockwise. The first step to obtain *el* and *Az* is to project the LOS vector to the RTN frame

$$\boldsymbol{\rho}_{RTN} = (\boldsymbol{\rho} \cdot \hat{\mathbf{R}})\hat{\mathbf{R}} + (\boldsymbol{\rho} \cdot \hat{\mathbf{T}})\hat{\mathbf{T}} + (\boldsymbol{\rho} \cdot \hat{\mathbf{N}})\hat{\mathbf{N}} \tag{2.33}$$

For the velocity in the RTN frame we can not just simply project $\dot{\mathbf{r}}_{LOS}$ in to RTN, since RTN is a rotating frame so we must account for additional angular velocity perceived by the observer. We refer to this corrected velocity as $\dot{\boldsymbol{\rho}}_{rot}$, and calculate it as

$$\dot{\boldsymbol{\rho}}_{rot} = \dot{\boldsymbol{\rho}} - \boldsymbol{\omega} \times \boldsymbol{\rho} \tag{2.34}$$

Where the angular velocity of the rotating reference frame $\boldsymbol{\omega}$ must be calculated accordingly to the satellite's motion. An expression for $\boldsymbol{\omega}$ is given by Casotto [34], and to obtain it we start with the time derivatives of the three unit vectors that define the RTN frame

$$\begin{aligned}
\frac{d\hat{\mathbf{R}}}{dt} &= \frac{1}{r}(\dot{\mathbf{r}} \cdot \hat{\mathbf{T}})\hat{\mathbf{T}} \\
\frac{d\hat{\mathbf{T}}}{dt} &= \frac{r}{h}(\ddot{\mathbf{r}} \cdot \hat{\mathbf{N}})\hat{\mathbf{N}} - \frac{1}{r}(\dot{\mathbf{r}} \cdot \hat{\mathbf{T}})\hat{\mathbf{R}} \\
\frac{d\hat{\mathbf{N}}}{dt} &= -\frac{r}{h}(\ddot{\mathbf{r}} \cdot \hat{\mathbf{N}})\hat{\mathbf{T}}
\end{aligned} \tag{2.35}$$

Where $r = |\mathbf{r}|$ and $h = |\mathbf{r} \times \dot{\mathbf{r}}|$. Additionally, the time derivatives of the unit vectors must result from the cross product between the angular velocity vector and the unit vectors

them selves

$$\begin{aligned}\frac{d\hat{\mathbf{R}}}{dt} &= \boldsymbol{\omega} \times \hat{\mathbf{R}} \\ \frac{d\hat{\mathbf{T}}}{dt} &= \boldsymbol{\omega} \times \hat{\mathbf{T}} \\ \frac{d\hat{\mathbf{N}}}{dt} &= \boldsymbol{\omega} \times \hat{\mathbf{N}}\end{aligned} \tag{2.36}$$

Then both sides are left-multiplied vectorially by the respective unit vector

$$\begin{aligned}\hat{\mathbf{R}} \times \frac{d\hat{\mathbf{R}}}{dt} &= \hat{\mathbf{R}} \times (\boldsymbol{\omega} \times \hat{\mathbf{R}}) = (\boldsymbol{\omega} \cdot \hat{\mathbf{T}})\hat{\mathbf{T}} + (\boldsymbol{\omega} \cdot \hat{\mathbf{N}})\hat{\mathbf{N}} \\ \hat{\mathbf{T}} \times \frac{d\hat{\mathbf{T}}}{dt} &= \hat{\mathbf{T}} \times (\boldsymbol{\omega} \times \hat{\mathbf{T}}) = (\boldsymbol{\omega} \cdot \hat{\mathbf{R}})\hat{\mathbf{R}} + (\boldsymbol{\omega} \cdot \hat{\mathbf{N}})\hat{\mathbf{N}} \\ \hat{\mathbf{N}} \times \frac{d\hat{\mathbf{N}}}{dt} &= \hat{\mathbf{N}} \times (\boldsymbol{\omega} \times \hat{\mathbf{N}}) = (\boldsymbol{\omega} \cdot \hat{\mathbf{R}})\hat{\mathbf{R}} + (\boldsymbol{\omega} \cdot \hat{\mathbf{T}})\hat{\mathbf{T}}\end{aligned} \tag{2.37}$$

The sum of these three equations allows us to solve for $\boldsymbol{\omega}$

$$2\boldsymbol{\omega} = \hat{\mathbf{R}} \times \frac{d\hat{\mathbf{R}}}{dt} + \hat{\mathbf{T}} \times \frac{d\hat{\mathbf{T}}}{dt} + \hat{\mathbf{N}} \times \frac{d\hat{\mathbf{N}}}{dt} \tag{2.38}$$

Now we can replace the derivatives from equations 2.35

$$2\boldsymbol{\omega} = \frac{1}{r}(\dot{\mathbf{r}} \cdot \hat{\mathbf{T}})(\hat{\mathbf{R}} \times \hat{\mathbf{T}}) + \frac{r}{h}(\ddot{\mathbf{r}} \cdot \hat{\mathbf{N}})(\hat{\mathbf{T}} \times \hat{\mathbf{N}}) - \frac{1}{r}(\dot{\mathbf{r}} \cdot \hat{\mathbf{T}})(\hat{\mathbf{T}} \times \hat{\mathbf{R}}) - \frac{r}{h}(\ddot{\mathbf{r}} \cdot \hat{\mathbf{N}})(\hat{\mathbf{N}} \times \hat{\mathbf{T}}) \tag{2.39}$$

which simplifies to

$$\boldsymbol{\omega} = \frac{r}{h}(\ddot{\mathbf{r}} \cdot \hat{\mathbf{N}})\hat{\mathbf{R}} + \frac{1}{r}(\dot{\mathbf{r}} \cdot \hat{\mathbf{T}})\hat{\mathbf{N}} \tag{2.40}$$

This expression calculates the instantaneous angular velocity vector of the rotating RTN frame. As it is observed, additional to the complete state vector of the satellite (i.e. $\mathbf{r}$ and $\dot{\mathbf{r}}$), the acceleration $\ddot{\mathbf{r}}$ is required for this calculation.

Going back to equation 2.34, the corrected velocity calculated and then projected into the rotating frame is

$$\dot{\boldsymbol{\rho}}_{RTN} = (\dot{\boldsymbol{\rho}}_{rot} \cdot \hat{\mathbf{R}})\hat{\mathbf{R}} + (\dot{\boldsymbol{\rho}}_{rot} \cdot \hat{\mathbf{T}})\hat{\mathbf{T}} + (\dot{\boldsymbol{\rho}}_{rot} \cdot \hat{\mathbf{N}})\hat{\mathbf{N}} \tag{2.41}$$

Having the cartesian representation of $\boldsymbol{\rho}_{RTN}$ and $\dot{\boldsymbol{\rho}}_{RTN}$, Az and el are obtained slightly differently to α and δ in equation 2.30

$$\begin{aligned} Az &= \arctan\left(\frac{-\rho_N}{\rho_T}\right) & el &= \arctan\left(\frac{\rho_R}{\sqrt{\rho_T^2 + \rho_N^2}}\right) \\ \dot{Az} &= \frac{\rho_N\dot{\rho}_T - \rho_T\dot{\rho}_N}{\rho_T^2 + \rho_N^2} & \dot{el} &= \frac{\dot{\rho}_R - |\dot{\boldsymbol{\rho}}_{RTN}| \sin el}{\sqrt{\rho_T^2 + \rho_N^2}} \end{aligned} \tag{2.42}$$

Similarly to the inertial case, we have a relative angular velocity, this time as it would be seen by the observer on its rotating RTN reference frame

$$\omega_{RTN} = \sqrt{\dot{Az}^2 \cos^2(el) + \dot{el}^2} \tag{2.43}$$

3

Target Constellation

Testing our simulated orbit determination system requires modeling situations where our orbiting observer would perform optical measurements on realistic targets. For this, a natural approach would be to generate synthetic targets that would resemble what can be found in reality. In our case, we decide on a different approach, since the number of LEO satellites has risen considerably in the recent years and their orbital data is available. In this work, we focus our attention on the Starlink mega constellation as a target for our modeled observer. The high number of satellites in a considerably narrow orbital shell makes the proper vigilance of this targets relevant. In this chapter we characterize the constellation, to better understand how we must then design the orbit of our observing platform.

3.1 The Starlink Constellation

As of April 2024, starting from May 24th 2019, the privately owned aerospace company Space Exploration Technologies Corporation (SpaceX) had placed close to 6000 satellites in LEO with the purpose of building a mega-constellation of around 12,000* "Starlink" internet providing satellites [36]. Being the largest satellite constellation ever to be as-

*Some sources more recently claim the intention of further expanding the constellation to an eventual size of 42,000 satellites[35].

sembled, it is of high interest to evaluate the possibility of using a passive optical SBSS platform, capable of acquiring accurate orbital information about as many assets as possible as a mean of supporting the situational awareness for its orbital shell and its vicinity.

Satellite Sizes

The Starlink satellites have been developed in different versions. Starlink Block v1.5, is the version that accounts for the majority of the currently operating satellites and it has been stated that they have approximately the size of a table [35]. A more recent and larger iteration is now being started to be launched. For the purposes of our simulations, we must have an idea of the size of the objects on interest, since it is a variable that determines our simulated observed visual magnitude. Trying to be conservative, without an extensive detailed simulation of how our targets would in reality reflect the sunlight, we choose the already mentioned diffuse sphere phase angle function (equation 2.28) along with reflected magnitude expression described in equation 2.26, with a chosen value of $A\gamma = 0.1$ m^2 for the product between the cross-sectional area and the reflectivity.

3.1.1 Characterization of the Constellation

In order to understand the way the constellation has been designed, we perform an analysis using orbital information of 5663 satellites acquired from the TLE's published by CelesTrak [37] on the 4th of April 2024. The Starlink constellation uses the Walker geometry, a configuration described by John Walker [38], which consists in grouping satellites in equally spaced orbital planes at the same inclination. Walker-star is the geometry that corresponds a near polar inclination, while Walker-delta (which is the case for Starlink) uses less inclined planes. Starlink employs this structure using multiple inclinations, meaning that its made of a set of Walker geometries. The key advantage of a Walker constellation is the maximization of ground coverage, with the minimum number of satellites required, making it ideal for communication systems.

Inclinations

To begin, we identify the different inclination on the analyzed data. Figure 3.1 shows the results of plotting the inclination's histogram, where satellites are grouped in 5 groups

according to this parameter. The average inclinations found are: 53.06° for group 1, 70.00° for group 2, 97.66° for group 3, 53.21° for group 4, and 43.00° for group 5. The naming convention for the groups is chosen to be consistent with previous analyses done by McDowell [39] and Krebs [40].

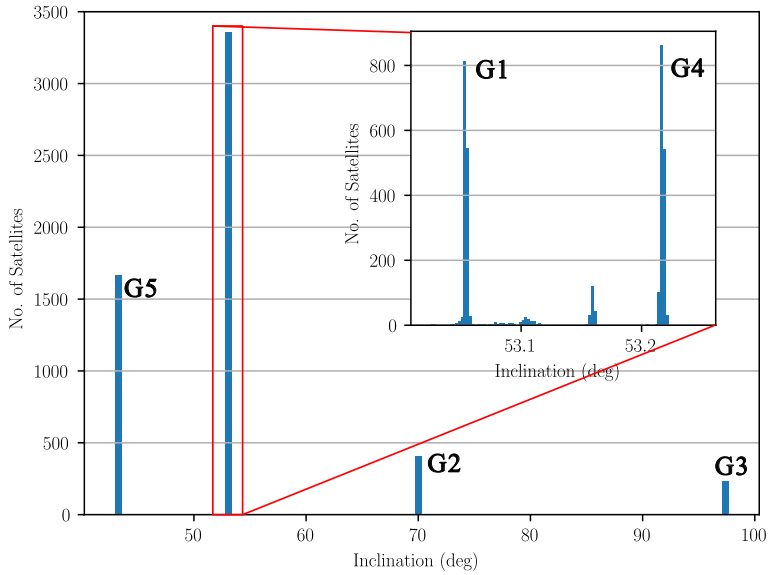

Figure 3.1: Starlink's inclinations histogram. Inclinations are taken from the TLEs and their frequencies are plotted. A zoom is performed on the tallest bar, where two distinct populations are identified. Satellites are labeled into 5 groups according to the inclination as shown.

Altitudes

Concerning the altitudes of the constellation, we produce another histogram (Figure 3.2) for the altitudes and a color code for their respective inclinations group. For this we only consider satellites close to their nominal altitude, since the data also shows satellites that are were recently launched and their orbits are still being raised, or in the other hand are now at the end of their life cycles and are now decaying to eventually burn in the atmosphere. The histograms clearly shows that the groups are also segregated by altitude, which means that the satellites are arranged in 5 shells. In order to filter out the outliers we present the median altitude for each group: 554.4 km for group 1, 579.2 km for group 2, 570.1 km for group 3, 546.9 km for group 4, and 566.2 km for group 5.

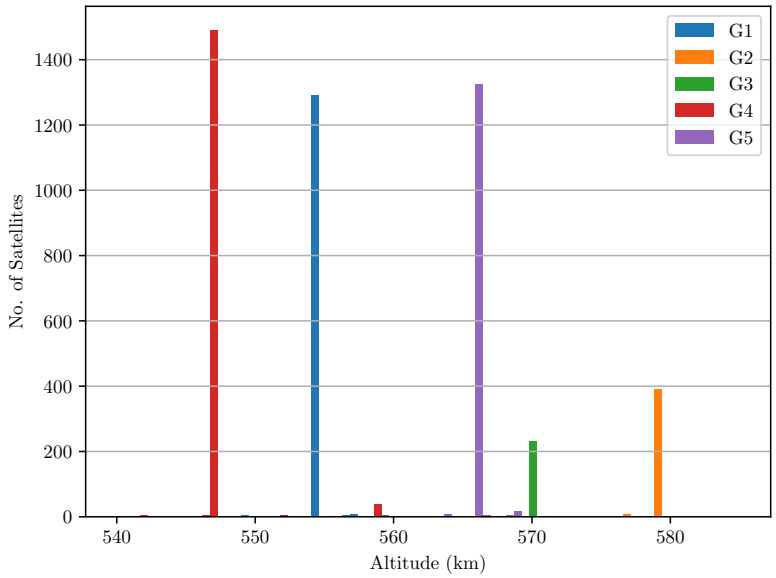

Figure 3.2: Starlink's altitudes histogram. Following the grouping shown in Figure 3.1, we observe how for each inclination there is a respective altitude, forming a total of 5 orbital shells.

The altitude, along with the inclination allows as to obtain information about the orbital planes' precession rate. Equation 3.1 shows us how to obtain it by setting J_2 and $R_\oplus$ to the values in Table **??**, and having $n = \sqrt{\mu/a^3}$ as the mean motion.

$$\dot{\Omega} = -\frac{3}{2} J_2 \left(\frac{R_\oplus}{a(1-e^2)} \right)^2 n \cos i. \tag{3.1}$$

When looking at the eccentricity values of all 5663 satellites, we get an average of 2×10^{-4} with a standard deviation of 6×10^{-4}, which allows us to treat our orbits as circular and consider $e = 0$ in the calculations of the precession rate. In particular we can recognize that group 3 has an inclination larger than 90° which implies a retrograde motion; when substituting the values already mentioned on equation 3.1, a precession rate of 0.983658 °/day is found. This value is very close to the idealized 0.9856 °/day that dictate the movement of the sun around the ECI reference frame according to Boain [41]. We may conclude then that the satellites belonging to group 3 are set in sun-synchronous orbits, as it was also stated by Iemole [42].

Groups 1 and 4, which account for 60% of all the satellites, and have very close inclinations around 53°, also show to have the same precession rate. In a similar analysis to

the one conducted by McDowell [39], Figure 3.3 shows how the same precession rate, represented by the straight line for $\dot{\Omega} = -4.4735°/\text{day}$, adjusts to both clusters on the inclination-altitude plane.

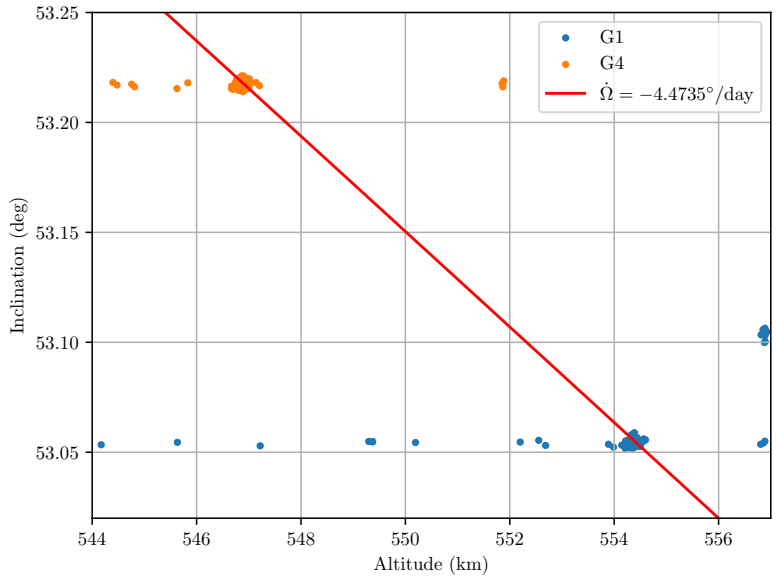

Figure 3.3: Precession rate of groups 1 and 4. Inclination and altitude obtained from Starlink's TLEs, with the line of constant precession rate adjusting well to both clusters of satellites.

RAAN

A final aspect to be analyzed regarding the structure of the Starlink constellation is the different orbital planes that make up each one of the defined groups. To do this, we look at the distribution of the satellites' right ascension of the ascending node (RAAN), again taking it from the TLEs. The proper analysis of this orbital element requires some pre-possessing, since as it was made evident on the last Section, the precession rate for these altitudes and inclinations, is in the order of degrees per day. Given the nature of the TLEs not being published with common epoch, and rather spanning a period of around 1 day, without a proper correction, the values of RAAN wouldn't help us distinguishing the different orbital planes. For this reason we correct the RAAN of each satellite to a common epoch using SGP4.

The resulting values of RAAN are shown in histograms for each of the given groups.

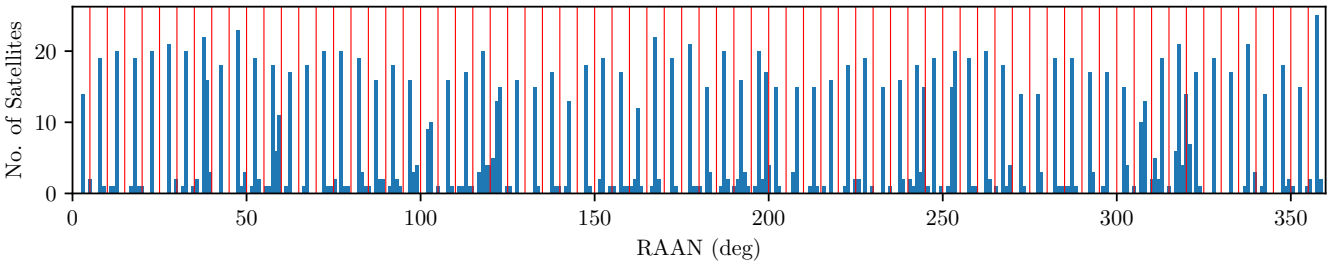

Figure 3.4: Group 1 RAAN histogram. Group 1 Starlink satellites, which correspond to an inclination of 53.06°, are divided according to their RAAN in to orbital planes, a total of 72 equally spaced orbital planes are found with an average of $\sim$ 22 satellites each.

As an example, group 1 is shown in Figure 3.4 while the other groups can be found in Figures B.1–B.4 on appendix B.

Constellation Summary

The following table summarizes the structure of the Starlink constellation.

Group No.	i (deg)	h (km)	No. of Planes	Satellites per Plane	No. of Satellites
1	53.00	554.4	72	22	1613
2	70.00	579.2	21	18	405
3	97.66	570.1	5	47	233
4	53.21	546.9	72	24	1745
5	43.00	566.2	28	60	1667
Total					**5663**

Table 3.1: Starlink constellation summary. Information taken from TLEs on April 4th, 2024.

Comparing these results with information available on the matter, we see that group 1 is described in an authorization application document submitted to the Federal Communications Commission (FCC) [43]. In there, an orbital shell with nominal altitude of 550 km, inclination of 53°, and 72 orbital planes with 22 satellites each is requested for authorization, these are parameters that are consistent with our findings.

4

Observer's Orbit Design

Based on the characteristics of the Starlink constellation presented in the previous chapter, we now set out to determine the optimal orbit for our observing satellite and the direction in which it should point.

4.1 Choosing the Observer's Orbit

Being concerned with finding a suitable orbit for our observation platform, we perform various simulations by propagating the TLEs of all our targets along with our potential observer for a time window of 48 hours using SGP4. All this, with the objective of obtaining statistics of the amount and the quality of the possible observations.

4.1.1 Simulation Parameters

The FOV of our observing instrument, as described in Section 2.2, is key for defining the capabilities of the system. To choose a reasonable FOV, we refer to operational SBSS systems performing similar tasks. The Canadian Sapphire satellite [7] whose optical design was based on US's Space-Based Visible (SBV) telescope [3] uses a FOV of 1.4$\times$ 1.4°, although the SBV can be increased to 1.4$\times$ 5.6° by using multiple CCDs. Other works have proposed similar FOVs such as Utzmann et al. [1] with 3 $\times$ 3°. Based on

these examples, we propose a FOV of a 4° diameter cone, which would correspond to $\theta_{FOV} = 2°$, following the convention from Section 2.2.1. Although such a wide FOV is ideal for surveillance activities, precise tracking of RSOs would benefit from a smaller FOV that could increase the precision of astrometric measurements. In particular, assuming a separation of $\sim$ 2000 km between observer and target, a 4096 $\times$ 4096 pixel sensor would require a FOV of $\sim$ 0.1° for one pixel to distinguish meter level changes on the target's position perpendicular to the LOS direction.

Assuming that we have full control of our observing satellite, and we could point its telescope to any direction we need, for an initial approach, we will ignore the FOV and simply gather all the information about all possible observations on all directions. Later we will need to develop an observation strategy to know where and how to take measurements.

Angular Rate and Limiting Magnitude

When considering the fact that our measurements involve objects that move at high velocities relative to each other, we need to consider a maximum relative angular velocity value for the measurement to be useful. Assuming that measurements would be performed in one of the two pointing methods introduced in Section 2.3 (i.e. inertial or body-fixed), the crossing of the target across the FOV must take enough time for us to obtain sufficient information to determine an orbit. An initial orbit determination (IOD) method such as the Gauss method, requires three astrometrical measurements to produce a result, in our observation scheme, these observations would come from the edges of the streaks, left by the target's movement with respect to a stellar background after a certain exposure time. Based on this, we set a maximum angular rate of 13 arc-minutes/s, which considering the size of our FOV, would allow for a target to cross it in almost 18.5 seconds if it moved in a straight line through the center of the FOV. For illustration, at this rate, an object would take $\sim$ 2.4 seconds to move across the Moon as seen from Earth. Naturally, this new constraint would be applied to $\omega_{Inertial}$ or ω_{RTN} (defined in equations 2.31 and 2.43 respectively) depending on the pointing mode. It is worth noting that with a LEO observer in an almost circular orbit, the difference between both rates is at most 3.8 arc-minutes/s.

If we establish 6 second exposures, followed by 6 seconds for readout and reduction, we

can obtain essentially a streak edge and hence a measurement, with a cadence of 6 seconds. For the 18 seconds that the target would spend inside the FOV we would always obtain the 3 measurements required for IOD. According to the proposed system by Utzmann et al. [1], a 2k $\times$ 2k detector with onboard data reduction can achieve a frame period of 1.5 s/frame, which is more than enough for our proposed cadence. Moreover, regarding the maximum detectable magnitude, by referring to the available information on the Canadian satellite NEOSSat [8], GEO objects with magnitude 16 can be detected with exposures of less than 10 seconds. Considering our 6 second exposures, and the fact that we would always deal with streaks that spread light across more pixels than a point source captured statically, we set our limiting magnitude to $m_V = 14$.

Exclusion Angles

Going back to the constraints that we presented in Section 2.2.4, after the addition of the angular rate constraint and the definition of the limiting magnitude, we are only left with establishing the exclusion angles to be considered in our simulations. For our case, as already mentioned, we will consider the solar, terrestrial and lunar exclusion angles. The values we use are again taken from the NEOSSat example [8], where $\alpha_{\odot} = 45°$ (meaning a maximum phase angle of $\Phi = 135°$), $\alpha_{\oplus} = 10°$, and $\alpha_{☾} = 4°$. Table 4.1 summarizes the parameters for the simulations.

Parameter	**Value**
max angular rate	13 arc-minutes/s
limiting m_V	14
$\alpha_{\odot}$	45°
$\alpha_{\oplus}$	10°
$\alpha_{☾}$	4°

Table 4.1: Parameters for Simulation. These parameters define the constraints mentioned in Section 2.2.4.

4.1.2 Simulation Strategy

As mentioned before, we want to obtain information from a 48 hour propagation of the entire constellation using SGP4. To be consistent with the 6 second cadence established in the last Section, we take this value as our step size, meaning that we get a total of

28,800 time instances. For each time instance, the observability of each target is evaluated with respect to the observer, if the target appears visible, according to the established constraints, the apparent magnitude, along with the right ascension and declination and their respective rates are obtained.

From the set of simulated observations, we calculate the number of possibilities to observe a target per day and the percentage of observable targets, within our observation window, from the total sample. Additionally, we are interested in knowing about the possibility of performing follow-up observations to the detected objects, so we also seek to maximize the chances of observing a target more than once.

Choosing a Nearby Orbit

An initial approach to the space-based observation problem, would be to situate the observer in an orbit close to the potential targets. Naturally, optical measurements require a stellar background to determine the target's angular position, so having an altitude below the aimed targets would be reasonable. Since the bast majority of Starlink's satellites have an inclination close to 53° (i.e. groups 1 and 4), situating a sensor at this inclination but a slightly lower altitude is a reasonable choice. The difference in altitude also provides a difference in the precession rates of the line of nodes between the observer and the targets. This eventually leads to the observer being able to sweep along all the orbital planes of the constellation.

Choosing a Sun-Synchronous Orbit (SSO)

In the other hand, although not being that intuitive, a sun-synchronous orbit (SSO), when it is specifically set in a dawn-dusk plane, is the classical choice for space surveillance applications as explained by Oswald et al. [44]. Although its use has been focused widely for observation of the geostationary (GEO) orbital regime, it has also found utility for LEO targets. In fact, already mentioned examples such as the SBV, NEOSSat, SAPPHIRE and even proposed ones such as ESA VISDOMS, all use the SSO design as conveniently compiled by Yunpeng et al. [45]. The reasons for this preference are mainly the possibility of ensuring the proper illumination of the targets at all times if we have an observer

pointing in an anti-sun direction. Being a SSO, the observing satellite will remain in the dawn-dusk plane, very close the terminator line, where the phase angle Φ for the targets is minimized, providing a higher apparent brightness and at the same time allowing to get closer to very inclined targets due to the high value of the inclinations required in SSOs.

Additionally to the two inclinations presented, we include the inclination of 70° to be also evaluated; not only it would make sense given that group 2 has this same inclination, but it could also give us a better illustration of the effects that varying the inclination has on the performance of a potential observing platform.

Choosing an Altitude

With these considerations, we wish to compare these three inclinations for our observer, but moreover, we must choose an appropriate altitude from where to observe. As already mentioned, we would prefer to locate our observer on an orbit below that of our targets. However, considering that the Starlink constellation as evidenced in Figure 3.2 is located in the lower part of the LEO regime, we are quite limited when it comes to this choice. We would not like our altitude to be very similar to the one of the targets, as the orbital periods could get too close, and the encounters that would allow the measurements would essentially happen repeatedly, with a certain limited set of targets, leaving others unobserved for long periods of time. Conversely, below 550 km we do not have a lot of room to place a satellite before the atmospheric drag starts to play a substantial role and limits our operability.

We set out to evaluate two different altitudes for our observers, 500 km which is only 50 km under the nominal altitude of Starlink, and 450 km, which is 100 km below. Although it would require persistent station-keeping maneuvers, this altitude is still achievable. In summary we will compare 6 different orbits for our observer, they are listed in Table 4.2. The shape of the orbits is set to be circular, while the same value of RAAN is chosen for all cases corresponding to the dawn-dusk plane for the epoch of the simulation. We decide to keep this same value of RAAN not only for the SSO orbits, since in all cases it maximizes the chances of observing well illuminated targets for longer time periods.

Inclination (deg)	Altitude (km)	RAAN (deg)
53.0000	450	282.7371
53.0000	500	282.7371
70.0000	450	282.7371
70.0000	500	282.7371
97.2139	450	282.7371
97.4015	500	282.7371

Table 4.2: Observer Orbits to be Evaluated. The eccentricity is set to be 0, while the value of the RAAN is chosen to correspond to the dawn-dusk plane at the epoch $JD = 2460403.95851397$, which is April 3rd, 2024 at 11:00:15.607 UTC.

4.1.3 Orbit Evaluation Results

To begin, the 48 hour simulation is run for each case, and we record every time that a target becomes available to be observed by our platform, considering the established constraints but disregarding any FOV. This means that any given target recorded by this statistic, could be observed after a certain slewing maneuver to point the telescope at it. The number of observations per day is recorded as it is shown in Figure 4.1a. Additionally, we keep track of all the targets that had at least 1 valid observation opportunity, and obtain a percentage of the observed targets from our full sample. These percentages are presented in Figure 4.1b.

As seen in Figure 4.1, the increment of the inclination favors both the number of observable targets and the coverage of the constellation. Both values are maximized at the SSOs, and although for the observations per day, the 500 km altitude has a slight advantage over 450 km (38,596 to 37,960 obs/day); for the percentage of coverage, the 450 km altitude clearly presents its self as a better candidate (80.58 % to 54.20 %). The explanation for this difference comes from the difference of altitudes between the observer and the targets. Essentially having a larger difference, the 450 km orbit has a farther orbital period to the one of the targets so in the time period of simulation, the higher desynchronization allows for the observation of a wider variety of targets.

After analyzing the coverage percentage segmented by the defined groups of the Starlink constellation, as seen in Figure 4.2, the dominance of the 450 km high SSO is confirmed. Group 4 has the lowest coverage with 76.49 % while groups 2 and 3 have cover-

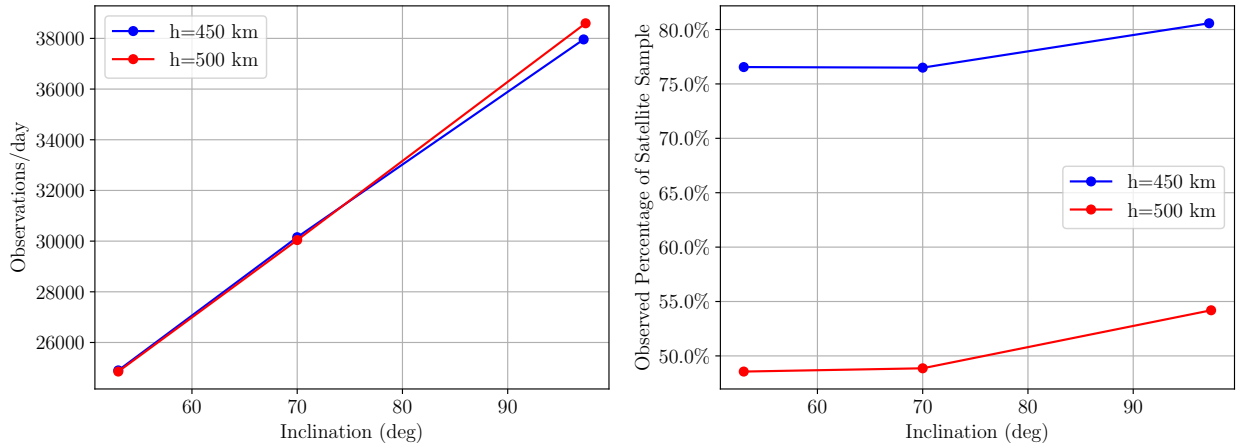

(a) Recorded observations per day.

(b) Observed targets from sample.

Figure 4.1: Observation Statistics of Starlink Constellation from Different Observing Orbits. The data is obtained from a 48 hour propagation where all possible observations that satisfy the constraints disregarding the FOV are recorded.

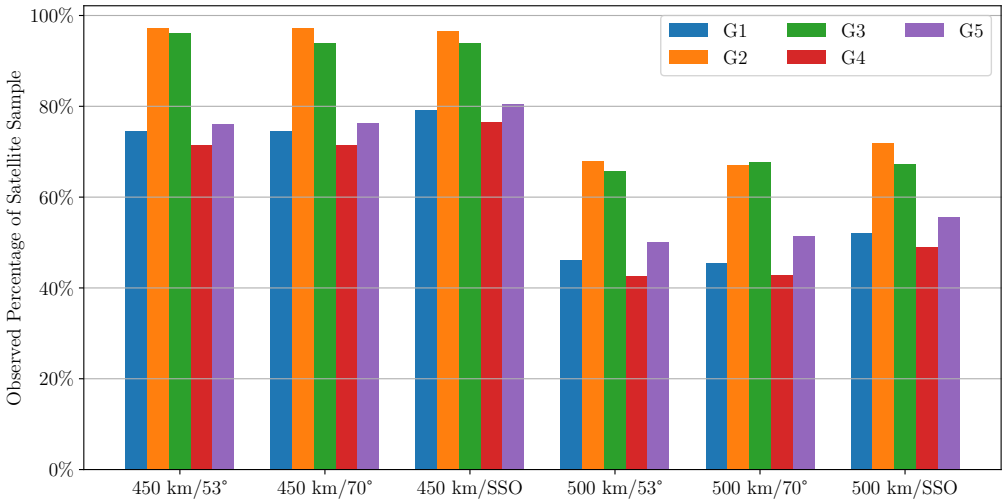

Figure 4.2: Observed Starlink Satellites by Group from Different Observing Orbits. The percentages presented in Figure 4.1b are segmented into the defined groups of the constellation. Horizontal axis shows altitude and inclination of observer's orbit.

ages over 90 % during the simulation period. It is interesting to see how same pattern for the coverage of each group is kept in every observer orbit evaluated. A clear relationship between these percentage values and the altitude of each group (shown in Figure 3.2) is observed, this suggests the same explanation given for Figure 4.1b about the difference in observer and target orbital period.

Following this analysis, we have found sufficient evidence to choose the 450 km high SSO as a proper orbit to place our observing platform. In the 48 hours simulated, the coverage of the Starlink constellation was 80.58 %, corresponding to 4563 out of 5663 targets. From now on, we will focus on this orbit only.

4.1.4 Follow-up Observations

Moving on from the choice of our observer's orbit, it is relevant to evaluate the possibility of follow-up observations on the targets, without the need of changing the orbit of the observer. For this purpose, we record each individual valid observation for the 4563 observed targets during the simulation. Grouping these observations by target, we obtain the histograms in Figure 4.3.

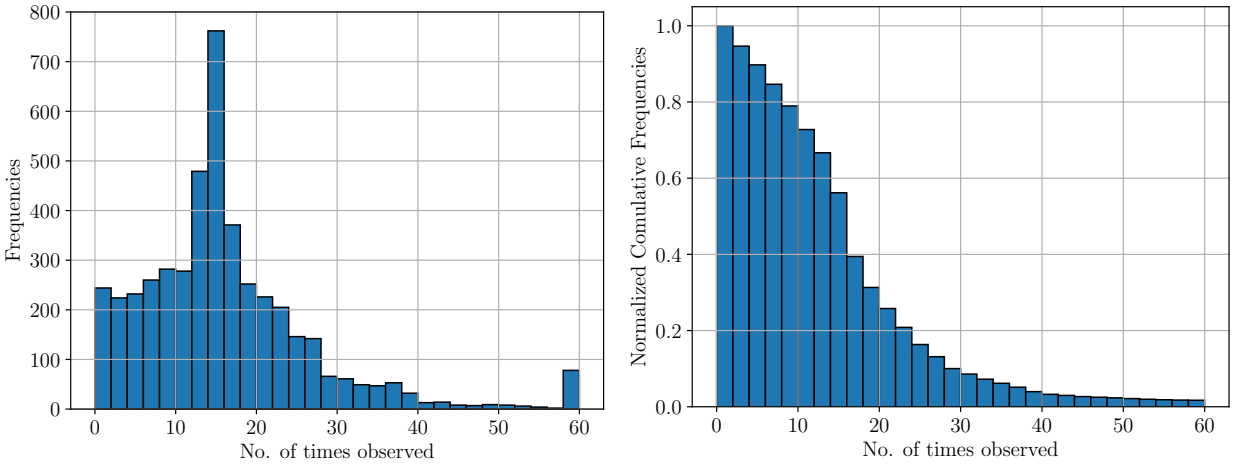

(a) Observation repetitions histogram.

(b) Comulative normalized histogram.

Figure 4.3: Follow-up Observations Histograms. Repetitions histogram for Starlink constellation observations in a 48 hour simulation from a 450 km high SSO observer.

When looking at the cumulative histogram in Figure 4.3b, we identify that 98 % of the observed targets are observed more than once, 76 % at least 10 times, and 28 % at least 20 times. These results are relevant because considering a single observation opportunity, and the fact that initially, we would not be tracking a given target, but rather recording its crossing of the FOV, we can take a limited amount of measurements. IOD methods

require at least 3 measurements, but if we want higher accuracy, we need to employ other methods such as least-squares fitting, and for this we must include more measurements, and we can only do that with follow-up observations. Knowing that almost every target evaluated has at least one follow-up chance, and that three quarters can be observed at least 10 times, gives us some confidence on the choice of the observing orbit's capacity to yield accurate results.

Slew Rate

A factor to be taken into account is the ability that our telescope would have to be reoriented in order to capture the next time a target would become visible. With an incorporated attitude control system, our observing satellite must be able to determine its pointing direction and change it according to a desired task to be performed. The slew rate is the speed at which the satellite can change its pointing direction, and to know what are our requirements on this regard, we obtain the histogram in Figure 4.4 from the complete set of contiguous follow-up observations. Essentially, the histogram stops at $\sim$ 3.83 arc-minutes/s, which is the rate required to cover the largest possible angular distance (i.e. 180°) in half an orbital period of the observer*, the latter being $\sim$ 47 minutes.

According to Abbasi et al. [8], NEOSSat has an active tracking mode that performs well for slew rates up to 90 arc-seconds/s, but making purely gyroscopic slews without the feed-back of star trackers, a rate of 220 arc-seconds/s could be achieved. With this in mind, we consider that most contiguous follow-up observations every half orbit could be achieved using available slewing technologies.

4.2 Choosing an Observing Direction

One of the key features that the observing telescope must have, is the ability to operate not only as a tracking device, which takes measurements of a known object as it follows its trajectory, but also in surveillance mode. The latter would refer to the mode of surveilling the platform's vicinity in the search for uncatalogued objects. Whenever the platform is

*This would also be the slew rate required to keep a body-fixed attitude at this altitude.

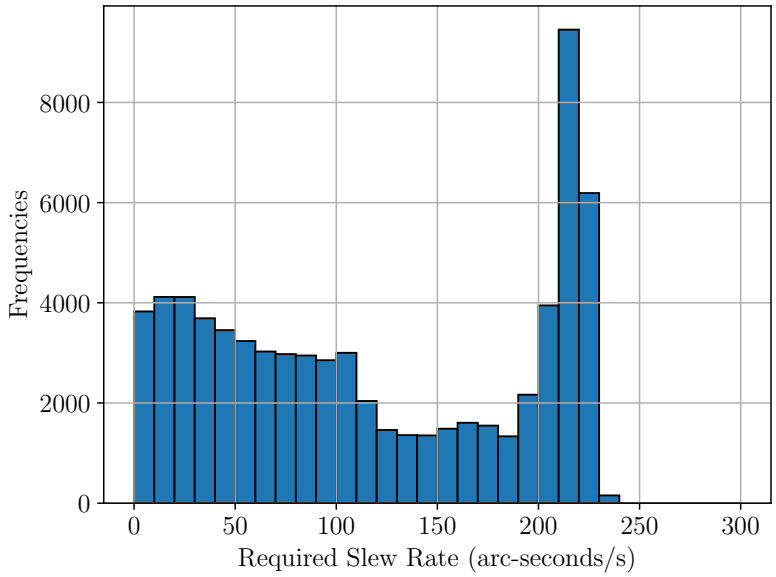

Figure 4.4: Minimum Slew Rate for Contiguous Follow-Up Observations. The histogram records the minimum slew rate required for each pair of contiguous follow-up observations.

acting in surveillance mode, we must decide on the best direction to point the telescope in order the maximize the chances of detecting our targets. As mentioned on chapter 2, there are two approaches for this task, first is pointing to a fixed direction in the sky, i.e. inertial pointing, and second is maintaining a constant pointing direction in the body-fixed (i.e., spacecraft-fixed) reference frame.

4.2.1 Inertial Pointing

The main advantages presented by an inertial pointing approach is the possibility of keeping the background stellar field static. Since ultimately, the background stars are used to perform the required astrometry on our target's streak edges, having them close to point sources in the acquired images allows for more precise measurements. The optimal pointing direction in this case needs to offer the highest chance of targets crossing the FOV. To begin, Figure 4.5 shows the amount of measurements acquired on all sky directions, using the Starlink sample and the chosen SSO observing satellite. Here we can clearly see an empty circle that corresponds to the sun and its entire exclusion solid angle. The most interesting region of the sky appears to be the anti-solar direction, where the highest concentration of measurements is found.

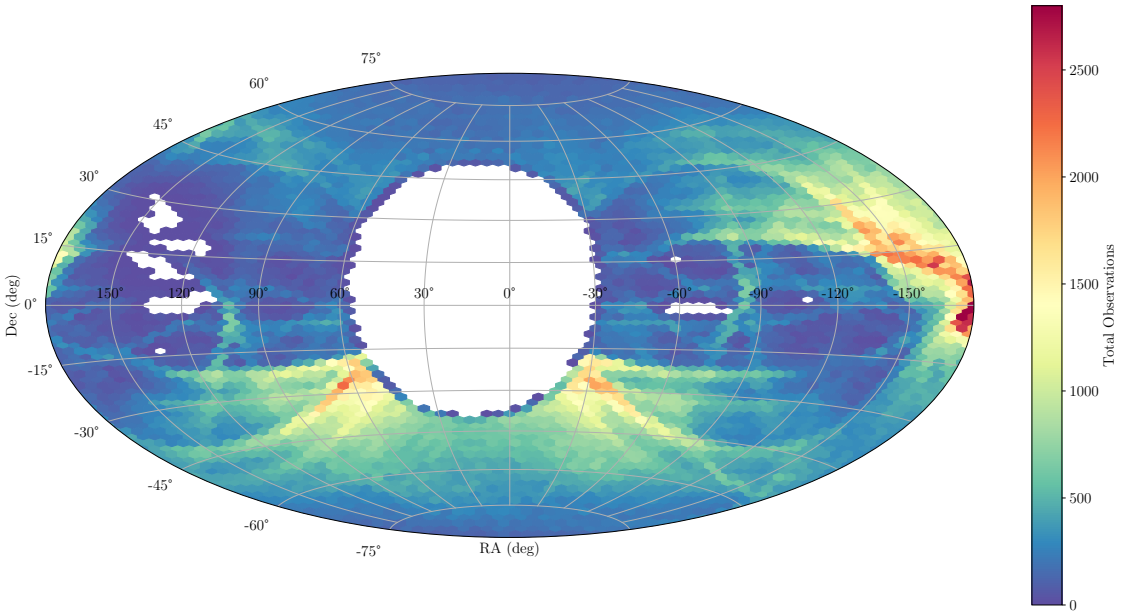

Figure 4.5: Observation density with inertial pointing. The data is obtained from a 48 hour propagation of the Starlink sample, as observed from a 450 km high SSO observer. Empty region corresponds to solar exclusion angle.

To find the best direction, we focus on the anti-solar region, which we define between $-10°$ and $10°$ of declination, and from $174°$ to $200°$ in right ascension. In Figure 4.6a we present the total streaks made up of at least 3 observations on each FOV for this region, while Figure 4.6b shows the percentage of the simulated sample that gets properly measured on each FOV.

The results displayed in Figure 4.6 clearly lean towards the FOV with declination of $4°$ and right ascension of $192°$. This particular FOV registered 988 streaks that covered almost 17% of our target sample. When considering the samples observed group by group, the least sampled group on this FOV is group 3 with 14.2% of targets, while the best covered group is group 4 with 23.2%. Given the low percentage of targets detected, if an inertial pointing strategy was to be taken, regular changed on the pointing direction could be performed to increase the overall coverage of the targets. In reality, the perspective would change if we extended our interest to other RSO populations, since any direction would contain detectable objects. The identification of correct target is in fact one of the problems faced by Space Tracking and Surveillance (SST).

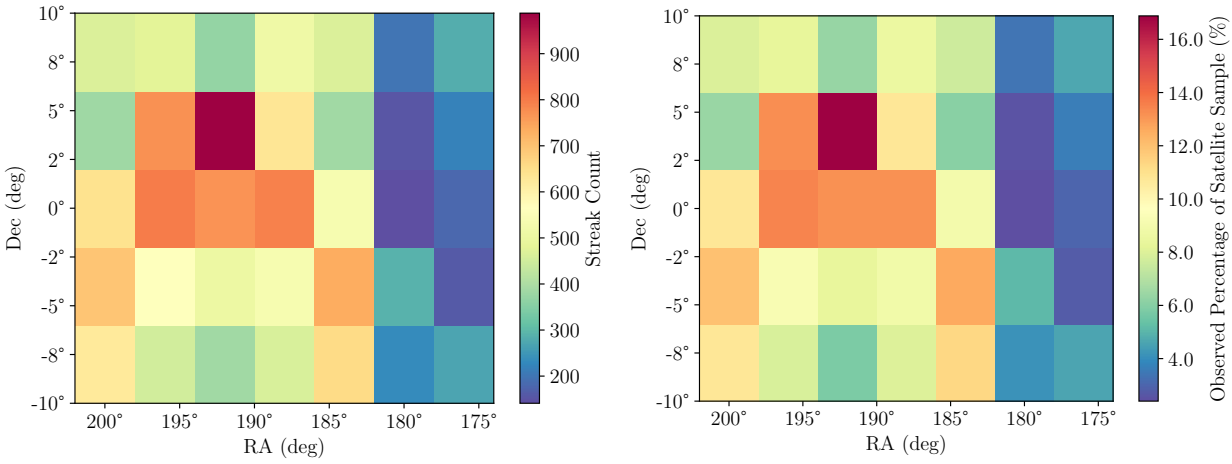

(a) Streak count.

(b) Observed targets from sample.

Figure 4.6: Statistics on different FOVs using inertial pointing. Total streaks and total unique targets among the Starlink sample are recorded for 35 FOVs from a 450 km high SSO observer.

4.2.2 Body-Fixed Pointing

The body-fixed strategy has the drawback of a constantly moving stellar background. With this consideration, the background stars used for astrometry would also appear as streaks, requiring their edges to be used, potentially lowering the achievable precision. Defining the body-fixed RTN frame as in Section 2.3.2, we produce the same analysis done for the inertial pointing, but referring to the local satellite-centered elevation and azimuth. The resulting count of valid observations for each direction is shown in Figure 4.7, where we see a clear concentration of measurements on low elevations. In fact, the outer ring of the plot which corresponds to FOVs centered at $-8°$, whose edges are almost at the edge of the terrestrial exclusion angle. Because of the SSO set in a dawn-dusk plane, we do not observe measurements around $Az = 90°$, where the solar exclusion angle of $45°$ makes appearance.

Following the same procedure as in the inertial pointing, we narrow the search zone to directions in all azimuths but elevation between $-10°$ and $10°$. Counting all the streaks formed by more than 3 observations and recording every unique target detected from our sample, we obtain Figure 4.8. Most observations are concentrated along the observer's trajectory, i.e. directly in front and behind, although in front, gets the advantage. By focusing on $el = -8°$, which has the better numbers, we see the largest streak count slightly

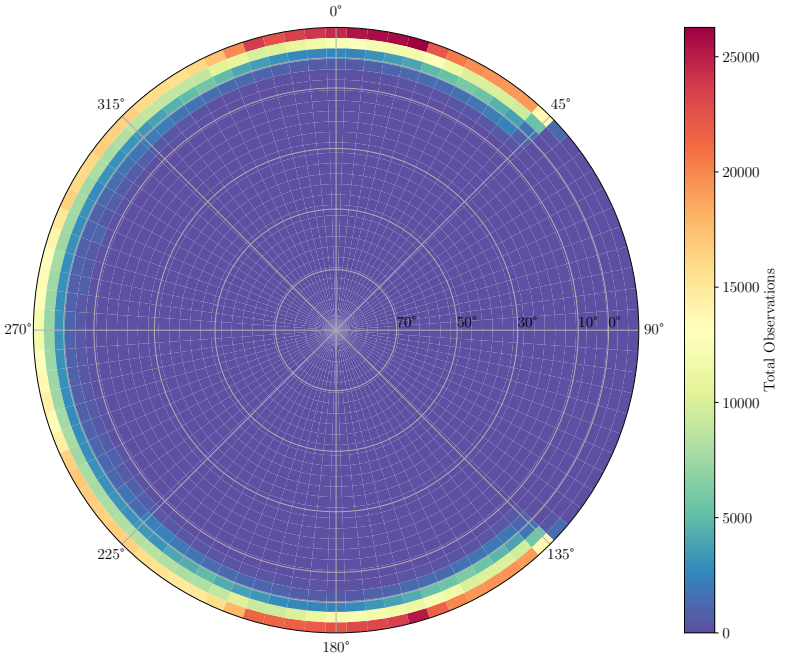

Figure 4.7: Observation density with body-fixed pointing. The data is obtained from a 48 hour propagation of the Starlink sample, as observed from a 450 km high SSO observer. Elevation and azimuth are represented with respect to the local horizon, and the along-track direction is defined at $Az = 0°$.

to the right of $Az = 0°$. However, 56.8% of the sample is the maximum targets observed by a FOV, and is seen directly on $Az = 0°$. With 4763 streaks, only 63 less than the FOV at $Az = 4°$, the FOV centered at $Az = 0°$ and $el = -8°$, seems to be the better candidate.

When looking at the results group by group, we see that for the selected direction, the least covered group is group 4 with 55.9% while group 2 achieves 72.8%. These are much higher values than the ones obtained with inertial pointing, and achieving a complete observation of the full sample could be achieved by sweeping other azimuth values close to 0° and 180°.

As mentioned at the beginning of this Section, the apparent motion of the stellar background is concerning for the required astrometry. In the RTN reference frame, the angular rate in the background stars results from the cross product between then LOS normalized vector of the FOV ($\hat{\boldsymbol{\rho}}$) and the angular velocity vector $\boldsymbol{\omega}$ described on equation 2.40. This value naturally gets maximized when $Az = 0°$ or 180°, which is unfortunately our region of interest. Due to this, we are left with an angular rate of 230.6 arc-seconds/s in the

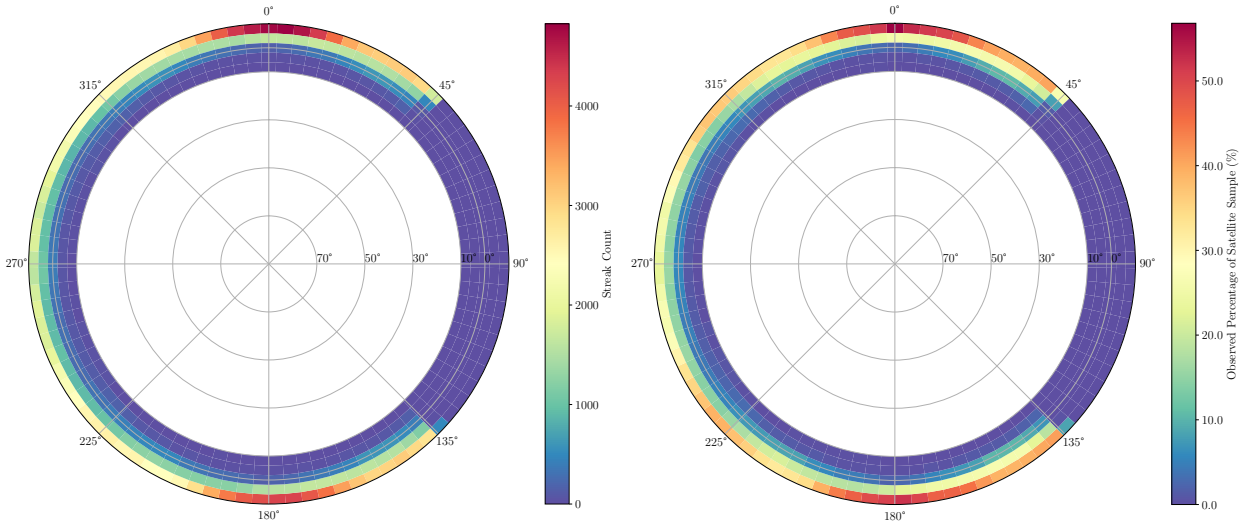

(a) Streak count.

(b) Observed targets from sample.

Figure 4.8: Statistics on different FOVs using body-fixed pointing. Total streaks and total unique targets among the Starlink sample are recorded for 445 FOVs, from a 450 km high SSO observer.

stellar background, which is equivalent to 3.8 arc-minutes/s. At our cadence of 6 seconds per observation (being the start or end of a target streak), the background stars would extend to streaks with length of $\sim$ 23 arc-minutes or one tenth the diameter of our FOV. Faster exposures could be considered to minimize the length of these background streaks, although this would limit the maximum magnitudes detectable for both the stars and the targets.

5

Initial Orbit Determination

A simple approach to be considered in our orbit determination problem, is the use of the classical initial orbit determination (IOD) methods that have been developed since Kepler´s descriptions of planetary motion and Newton's analytical framework for its understanding. In this chapter we will focus on the Gauss method, one of the first practical methods developed to obtain an object's orbit from angles-only measurements.

An important remark that must be done regarding the method to be exposed is the neglect of relativistic aberration. Following the principles of special relativity, any presence of relative motion between an observer and a light source results in a shift in the direction from where the light falls upon the observer. This naturally alters the ideal geometrical reasoning employed in these methods. Although aberration's effect, explicitly on the LOS, would not be that significant when considering the stellar background that would be used for the astrometry, the errors produced become relevant for our purposes and in a more realistic situation the effect would require being addressed.

5.1 The Gauss Method

The Gauss method, initially proposed by the Carl F. Gauss himself in 1801, was built on the limitation of not being able to measure an object's distance, but only knowing its

projection to spherical coordinates at a given time. Considering the need of deriving six orbital elements (the six components of an object's dynamical state vector), the same number of independent measured values is required. Since one single measurement provides two values, a minimum of three observations is required for the task. The following description of the method is based on the one done by Casotto [46], who references Bucerius [47] and Montenbruck [48].

The premise of the method is the condition that the three geocentric (in the original problem, heliocentric) position vectors of the target at the time of each measurement belong to the same plane and therefore satisfy

$$c_1\mathbf{r}_1 + c_2\mathbf{r}_2 + c_3\mathbf{r}_3 = \mathbf{0} \tag{5.1}$$

a condition first noted by Pierre Bouguer in 1733. With one of the three coefficients being redundant, we choose $c_2 = -1$. Since we measure the target's $\mathbf{r}_i$ positions from an observing satellite with position vectors give by $\mathbf{r}_{Oi}$*, the targets position vectors are then given by

$$\mathbf{r}_i = \rho_i\hat{\boldsymbol{\rho}}_i + \mathbf{r}_{Oi}, \quad i = 1,2,3 \tag{5.2}$$

where ρ_i and $\hat{\boldsymbol{\rho}}_i$ come from the previously introduced LOS vector for each observation. From the astrometrical measurements of right ascension (α) and declination (δ) we obtain the LOS unit vector as

$$\begin{aligned} \hat{\rho}_i &= \cos\delta\cos\alpha \\ \hat{\rho}_j &= \cos\delta\sin\alpha \\ \hat{\rho}_k &= \sin\delta \end{aligned} \tag{5.3}$$

Putting these equations together, we reach what would be the *fundamental equation* of the Gauss method

$$c_1\rho_1\hat{\boldsymbol{\rho}}_1 + c_2\rho_2\hat{\boldsymbol{\rho}}_2 + c_3\rho_3\hat{\boldsymbol{\rho}}_3 = -c_1\mathbf{r}_{O1} - c_2\mathbf{r}_{O2} - c_3\mathbf{r}_{O3} \tag{5.4}$$

*For briefness, here we change the convention used in Chapter 2 from $\mathbf{r}_{tar}$ to $\mathbf{r}_i$ and from $\mathbf{r}_{obs}$ to $\mathbf{r}_{Oi}$.

From this point, each range ρ can be isolated as

$$\begin{aligned} c_1\rho_1 + (c_1\mathbf{r}_{O1} + c_2\mathbf{r}_{O2} + c_3\mathbf{r}_{O3}) \cdot \boldsymbol{\xi}_1 = 0 \\ c_2\rho_2 + (c_1\mathbf{r}_{O1} + c_2\mathbf{r}_{O2} + c_3\mathbf{r}_{O3}) \cdot \boldsymbol{\xi}_2 = 0 \\ c_3\rho_3 + (c_1\mathbf{r}_{O1} + c_2\mathbf{r}_{O2} + c_3\mathbf{r}_{O3}) \cdot \boldsymbol{\xi}_3 = 0 \end{aligned} \tag{5.5}$$

where the vectors $\boldsymbol{\xi}_1$, $\boldsymbol{\xi}_2$, and $\boldsymbol{\xi}_3$ are defined from the LOS unit vectors, hence from the measurements

$$\begin{aligned} \boldsymbol{\xi}_1 &= \frac{\hat{\boldsymbol{\rho}}_2 \times \hat{\boldsymbol{\rho}}_3}{\hat{\boldsymbol{\rho}}_1 \cdot (\hat{\boldsymbol{\rho}}_2 \times \hat{\boldsymbol{\rho}}_3)} \\ \boldsymbol{\xi}_2 &= \frac{\hat{\boldsymbol{\rho}}_3 \times \hat{\boldsymbol{\rho}}_1}{\hat{\boldsymbol{\rho}}_1 \cdot (\hat{\boldsymbol{\rho}}_2 \times \hat{\boldsymbol{\rho}}_3)} \\ \boldsymbol{\xi}_3 &= \frac{\hat{\boldsymbol{\rho}}_1 \times \hat{\boldsymbol{\rho}}_2}{\hat{\boldsymbol{\rho}}_1 \cdot (\hat{\boldsymbol{\rho}}_2 \times \hat{\boldsymbol{\rho}}_3)} \end{aligned} \tag{5.6}$$

Notice that equations 5.5 form a system with three equations and five unknowns which are ρ_1, ρ_2, ρ_3, c_1 and c_3. To obtain a solution for this system we will require more equations and for this we will rewrite the c constants in terms of other geometrical variables.

Returning to equation 5.1 with $c_2 = -1$, we isolate c_1 by multiplying scalarly by a vector to cancel the term that includes c_3, i.e. a vector which is perpendicular to $\mathbf{r}_3$ but not to $\mathbf{r}_1$ or $\mathbf{r}_2$. This vector is $\mathbf{r}_3 \times (\mathbf{r}_3 \times \dot{\mathbf{r}}_3)$ which is more conveniently expressed as $\mathbf{r}_3 \times \mathbf{h}$ with $\mathbf{h}$ being the angular momentum vector. Then, solving for c_1 and repeating the same procedure for c_3, results in

$$\begin{aligned} c_1 &= \frac{\mathbf{r}_2 \cdot (\mathbf{r}_3 \times \mathbf{h})}{\mathbf{r}_1 \cdot (\mathbf{r}_3 \times \mathbf{h})} = \frac{(\mathbf{r}_2 \times \mathbf{r}_3) \cdot \mathbf{h}}{(\mathbf{r}_1 \times \mathbf{r}_3) \cdot \mathbf{h}} \\ c_3 &= \frac{\mathbf{r}_2 \cdot (\mathbf{r}_1 \times \mathbf{h})}{\mathbf{r}_3 \cdot (\mathbf{r}_1 \times \mathbf{h})} = \frac{(\mathbf{r}_2 \times \mathbf{r}_1) \cdot \mathbf{h}}{(\mathbf{r}_3 \times \mathbf{r}_1) \cdot \mathbf{h}} \end{aligned} \tag{5.7}$$

A further simplification can be done by considering that vectors $\mathbf{r_i} \times \mathbf{r_j}$ and $\mathbf{h}$ are collinear, hence

$$
\begin{aligned}
c_1 &= \frac{|\mathbf{r}_2 \times \mathbf{r}_3|}{|\mathbf{r}_1 \times \mathbf{r}_3|} = \frac{A_{23}}{A_{13}} \\
c_3 &= \frac{|\mathbf{r}_2 \times \mathbf{r}_1|}{|\mathbf{r}_3 \times \mathbf{r}_1|} = \frac{A_{21}}{A_{13}}
\end{aligned}
\tag{5.8}
$$

Where we include

$$
A_{ij} = \frac{1}{2}|\mathbf{r}_i \times \mathbf{r}_j| \tag{5.9}
$$

as the area of the triangle formed by vectors $\mathbf{r}_i$ and $\mathbf{r}_j$.

Following Kepler's second law, the area of a sector S_{ij} contained between vectors $\mathbf{r}_i$ and $\mathbf{r}_j$ is obtained from the time difference between them

$$
S_{ij} = \frac{1}{2}h(t_j - t_i) \tag{5.10}
$$

With this definition we can rewrite c_1 and c_3 as

$$
\begin{aligned}
c_1 &= \frac{S_{13}/A_{13}}{S_{23}/A_{23}}\frac{S_{23}}{S_{13}} = \frac{S_{13}/A_{13}}{S_{23}/A_{23}}\frac{(t_3 - t_2)}{(t_3 - t_1)} \\
c_3 &= \frac{S_{13}/A_{13}}{S_{21}/A_{21}}\frac{S_{21}}{S_{13}} = \frac{S_{13}/A_{13}}{S_{21}/A_{21}}\frac{(t_1 - t_2)}{(t_3 - t_1)}
\end{aligned}
\tag{5.11}
$$

Now by introducing the *sector-to-triangle* ratio (STT), represented by y_{ij}, as

$$
y_{ij} = \frac{S_{ij}}{A_{ij}} \tag{5.12}
$$

along with the time intervals τ_1, τ_2 and τ_3

$$
\tau_1 = t_1 - t_2, \qquad \tau_2 = t_3 - t_1, \qquad \tau_3 = t_3 - t_2 \tag{5.13}
$$

we obtain our final expressions for the c constants

$$
c_1 = \frac{y_{13}}{y_{23}}\frac{\tau_3}{\tau_2}, \qquad c_2 = -1, \qquad c_3 = -\frac{y_{13}}{y_{12}}\frac{\tau_1}{\tau_2} \tag{5.14}
$$

In terms of the STT ratios we can now express the system on 5.5 as

$$\begin{aligned}
(\rho_1 + a_{11})y_{12}y_{13}\tau_3 - a_{12}y_{12}y_{23}\tau_2 - a_{13}y_{13}y_{23}\tau_1 &= 0 \\
a_{21}y_{12}y_{13}\tau_3 - (\rho_2 + a_{22})y_{12}y_{23}\tau_2 - a_{23}y_{13}y_{23}\tau_1 &= 0 \\
a_{31}y_{12}y_{13}\tau_3 - a_{32}y_{12}y_{23}\tau_2 - (\rho_3 + a_{33})y_{13}y_{23}\tau_1 &= 0
\end{aligned} \tag{5.15}$$

Where we have introduced the auxiliary variables

$$\begin{aligned}
a_{11} &= \boldsymbol{\xi}_1 \cdot \mathbf{r}_{O1}, \quad a_{21} = \boldsymbol{\xi}_2 \cdot \mathbf{r}_{O1}, \quad a_{31} = \boldsymbol{\xi}_3 \cdot \mathbf{r}_{O1} \\
a_{12} &= \boldsymbol{\xi}_1 \cdot \mathbf{r}_{O2}, \quad a_{22} = \boldsymbol{\xi}_2 \cdot \mathbf{r}_{O2}, \quad a_{32} = \boldsymbol{\xi}_3 \cdot \mathbf{r}_{O2} \\
a_{13} &= \boldsymbol{\xi}_1 \cdot \mathbf{r}_{O3}, \quad a_{23} = \boldsymbol{\xi}_2 \cdot \mathbf{r}_{O3}, \quad a_{33} = \boldsymbol{\xi}_3 \cdot \mathbf{r}_{O3}
\end{aligned} \tag{5.16}$$

5.1.1 The Equations of Gauss

Now we have removed the c constants and introduced the STT ratios y_{12}, y_{13} and y_{23} as unknowns. We would still require three additional equations in order to have a solvable system. To accomplish this task we begin by considering that $h = \sqrt{\mu p}$, with $\mu = GM$ being the gravitational parameter and p the semilatus rectum of the orbit. Additionally, equation 5.9 can be expressed as $A = \frac{1}{2} r_i r_j \sin \Delta f$, where Δf is the angle between vectors $\mathbf{r}_i$ and $\mathbf{r}_j$, which in our context is represented by the true anomaly. With these two considerations, we can rewrite the STT ratio as

$$y_{ij} = \frac{\sqrt{\mu p}\Delta t}{r_i r_j \sin \Delta f} \tag{5.17}$$

Now, by using Lagrange coefficients F and $\dot{F}$ in terms of the true anomaly Δf and the eccentric anomaly ΔE between $\mathbf{r}_i$ and $\mathbf{r}_j$, we can find the following expression for p

$$p = \frac{r_i r_j (1 - \cos \Delta f)}{r_i + r_j - 2\sqrt{r_i r_j} \cos \frac{\Delta f}{2} \cos \frac{\Delta E}{2}} \tag{5.18}$$

and replacing it back in equation 5.17 we arrive to

$$y_{ij}^2 = \frac{\mu (\Delta t)^2}{2 r_i r_j \cos^2 \frac{\Delta f}{2} \left(r_i + r_j - 2\sqrt{r_i r_j} \cos \frac{\Delta f}{2} \cos \frac{\Delta E}{2} \right)} \tag{5.19}$$

For a more compact expression we introduce the following auxiliary variables

$$
\begin{aligned}
m_{ij} &= \frac{\mu(\Delta t)^2}{8 r_i r_j \sqrt{r_i r_j}\cos^3\frac{\Delta f}{2}} = \frac{\mu(\Delta t)^2}{2^{3/2}(r_i r_j + \mathbf{r}_i \cdot \mathbf{r}_j)^{3/2}} \\
l_{ij} &= \frac{r_i + r_j}{4\sqrt{r_i r_j}\cos\frac{\Delta f}{2}} - \frac{1}{2} = \frac{r_i + r_j}{2^{3/2}\sqrt{r_i r_j + \mathbf{r}_i \cdot \mathbf{r}_j}} - \frac{1}{2}
\end{aligned}
\tag{5.20}
$$

and putting them together, we get to the *first equation of Gauss*

$$
\boxed{y_{ij}^2 = \frac{m_{ij}}{l_{ij} + \sin^2\frac{\Delta E}{4}}} \tag{5.21}
$$

With this equation we have introduced ΔE as an additional unknown, so we need another expression to remove it. For this we use the Lagrange coefficient G, where again its expression in terms of Δf and ΔE, we find that

$$
1 - \frac{1}{y_{ij}} = \frac{1}{\Delta t}\sqrt{\frac{a^3}{\mu}}(\Delta E - \sin\Delta E) \tag{5.22}
$$

Then to remove a we use

$$
y_{ij} = \frac{\sqrt{\mu}\Delta t}{2\sqrt{a r_i r_j}\cos\frac{\Delta f}{2}\sin\frac{\Delta E}{2}} \tag{5.23}
$$

which comes from rewriting equation 5.17 but considering the following relation between the true and eccentric anomalies

$$
\sin\frac{\Delta f}{2} = \sqrt{\frac{ap}{r_i r_j}}\sin\frac{\Delta E}{2} \tag{5.24}
$$

By cubing equation 5.23 and multiplying it by equation 5.22 we reach

$$
y_{ij}^3 - y_{ij}^2 = \frac{\mu(\Delta t)^2}{8 r_i r_j \sqrt{r_i r_j}\cos^3\frac{\Delta f}{2}}\frac{\Delta E - \sin\Delta E}{\sin^3\frac{\Delta E}{2}} \tag{5.25}
$$

Where the first fraction on the rhs corresponds to the auxiliary variable m_{ij}, this way we arrive to the *second equation of Gauss*

$$
\boxed{y_{ij}^2(y_{ij} - 1) = m_{ij}\frac{\Delta E - \sin\Delta E}{\sin^3\frac{\Delta E}{2}}} \tag{5.26}
$$

The following step is the non trivial task of solving the system formed by the two equations of Gauss. To do so, we define

$$w = \frac{\Delta E - \sin \Delta E}{\sin^3 \frac{\Delta E}{2}} \tag{5.27}$$

as the fraction in the *second* equation, and

$$x = \sin^2 \frac{\Delta E}{4} \tag{5.28}$$

as the term in the first equation. The task would be to derive an expression for $w(x)$. We start from the derivative of w with respect to x expressed as

$$\frac{dw}{dx} = \frac{dw}{dE}\frac{dE}{dx} \tag{5.29}$$

Which produces

$$\sin^2 \frac{\Delta E}{2}\frac{dw}{dx} = 8 - 6w \cos \frac{\Delta E}{2} \tag{5.30}$$

This can then be rewritten in terms of the variable x instead of ΔE

$$2x(1-x)\frac{dw}{dx} + 3(1-2x)w - 4 = 0 \tag{5.31}$$

At this point, the solution to the differential equation is identified as a special form of Gauss hypergeometric function $F(\alpha, \beta; \gamma; x)$ normalized to 4/3, with parameters $\alpha = 3$, $\beta = 1$ and $\gamma = 5/2$.

$$w(x) = \frac{4}{3}F\left(3, 1; \frac{5}{2}; x\right) \tag{5.32}$$

By writing $x = m_{ij}/y_{ij}^2 - l_{ij}$ according to the *first* equation, we can now define a new function to express w

$$W(y_{ij}, l_{ij}, m_{ij}) = \frac{4}{3}F\left(3, 1; \frac{5}{2}; \frac{m_{ij}}{y_{ij}^2} - l_{ij}\right) \tag{5.33}$$

In the end we replace this result back in the *second* equation and we arrive to the *combined equation of Gauss*

$$\boxed{y_{ij}^2(y_{ij} - 1) - m_{ij}W(y_{ij}, l_{ij}, m_{ij}) = 0} \tag{5.34}$$

With this additional relation, which can be written for all three STT ratios, we can find a solution to our orbit determination problem.

5.1.2 First-Order Guess

The search for a solution was originally sought in an iterative procedure that requires an initial guess for the ranges ρ_1, ρ_2, and ρ_3. We will produce this guess by analysing the expansion of the Lagrange coefficients F and G expressed in terms of the time interval $\tau = t_i - t_j$ given as follows

$$\begin{aligned} F(t_i, t_j) &= 1 - \frac{1}{2}u_j\tau^2 + ... \\ G(t_i, t_j) &= \tau - \frac{1}{6}u_j\tau^3 + ... \end{aligned} \tag{5.35}$$

with $u_j = \mu/r_j^3$. Position vectors $\mathbf{r}_1$ and $\mathbf{r}_2$ are written as

$$\begin{aligned} \mathbf{r}_1 &= F(t_1, t_2)\mathbf{r}_2 + G(t_1, t_2)\dot{\mathbf{r}}_2 \\ \mathbf{r}_3 &= F(t_3, t_2)\mathbf{r}_2 + G(t_3, t_2)\dot{\mathbf{r}}_2 \end{aligned} \tag{5.36}$$

By replacing equations 5.36 in to the expressions for c_1 and c_3 in 5.7, we reach

$$\begin{aligned} c_1 &= \frac{G(t_3, t_2)}{F(t_1, t_2)G(t_3, t_2) - G(t_1, t_2)F(t_3, t_2)} \\ c_3 &= \frac{G(t_1, t_2)}{F(t_3, t_2)G(t_1, t_2) - G(t_3, t_2)F(t_1, t_2)} \end{aligned} \tag{5.37}$$

Then with the approximations in 5.35, we obtain the first order approximations for the c constants, denoted by the additional sub index "$_1$"

$$\begin{aligned} c_{11} &= \frac{\tau_3}{\tau_2} - \frac{1}{6}u_2\tau_1\tau_3\left(1 + \frac{\tau_3}{\tau_2}\right) \\ c_{31} &= -\frac{\tau_1}{\tau_2} - \frac{1}{6}u_2\tau_1\tau_3\left(1 - \frac{\tau_1}{\tau_2}\right) \end{aligned} \tag{5.38}$$

Our only unknown for these estimation of the c constants is u_2 for which we require a value of r_2. To determine this value we will set up a system of two equations and two

unknowns. To begin, we write ρ_2 from its equation on 5.5, as

$$\rho_2 = c_1 a_{21} - a_{22} + c_3 a_{23} \tag{5.39}$$

Then considering the approximations on 5.38 we write a first order approximation of ρ_2

$$\rho_{21} = A_2 - \frac{B_2}{r_2^3} \tag{5.40}$$

with

$$\begin{aligned} A_2 &= \frac{1}{\tau_2}(\tau_3 a_{21} - \tau_1 a_{23}) - a_{22} \\ B_2 &= \frac{\mu}{2}(\tau_3 a_{21} - \tau_1 a_{23})\frac{\tau_1 \tau_3}{\tau_2} \end{aligned} \tag{5.41}$$

Then we square the relation on 5.2 for $j = 2$

$$r_2^2 = \rho_2^2 + 2(\hat{\boldsymbol{\rho}}_2 \cdot \mathbf{r}_{O2})\rho_2 + r_{O2}^2 \tag{5.42}$$

By rearranging both equations we find the following system with unknowns ρ_2 and r_2

$$\begin{aligned} r_2^3 \rho_2 - A_2 r_2^3 + B_2 &= 0 \\ r_2^2 - \rho_2^2 - 2(\hat{\boldsymbol{\rho}}_2 \cdot \mathbf{r}_{O2})\rho_2 - r_{O2}^2 &= 0 \end{aligned} \tag{5.43}$$

and by removing the ρ_2 we arrive to the well know *Gauss-Lagrange equation*

$$\boxed{r_2^8 - A r_2^6 + B r_2^3 - C = 0} \tag{5.44}$$

with

$$\begin{aligned} A &= [A_2 + 2(\hat{\boldsymbol{\rho}}_2 \cdot \mathbf{r}_{O2})]A_2 + r_{O2}^2 \\ B &= [2A_2 + 2(\hat{\boldsymbol{\rho}}_2 \cdot \mathbf{r}_{O2})]B_2 \\ C &= B_2^2 \end{aligned} \tag{5.45}$$

The eight degree polynomial in the Gauss-Lagrange equation can have up to three real positive roots, which implies some caution when selecting the correct one. Once we have an initial guess for r_2 we can calculate the constants c_{11} and c_{31} from 5.38 and by solving

the ranges from equations 5.5 we can obtain initial values for each range as follows

$$\begin{aligned}\rho_{11} &= -a_{11} + \frac{1}{c_{11}}a_{12} - \frac{c_{31}}{c_{11}}a_{13} \\ \rho_{21} &= -a_{22} + c_{11}a_{21} + c_{31}a_{23} \\ \rho_{31} &= -a_{33} - \frac{c_{11}}{c_{31}}a_{31} + \frac{1}{c_{31}}a_{32}.\end{aligned} \tag{5.46}$$

After this, we can also produce an estimate for all three STTs by applying the first equation of Gauss 5.21 as

$$y_{ij1} = \sqrt{\frac{m_{ij1}}{l_{ij1} + \sin^2 \frac{\Delta E_{ij1}}{4}}} \tag{5.47}$$

where we would use the estimated ranges to estimate the target's positions, which then can be used to obtain the values of m_{ij1} and l_{ij1} from relations 5.20. As for the eccentric anomaly ΔE_{ij}, we can approximate it as $\Delta E_{ij} \cong \Delta f_{ij}$ such that we can introduce the following approximation

$$\sin^2 \frac{\Delta E_{ij1}}{4} \cong \frac{1}{2} - \frac{1}{2^{2/3}}\sqrt{1 + \hat{\mathbf{r}}_{i1} \cdot \hat{\mathbf{r}}_{j1}}. \tag{5.48}$$

On Choosing the Correct Root

As previously mentioned, the Gauss-Lagrange equation shown on 5.44 can have up to three real positive roots and identifying the correct one is crucial for a correct resolution of the IOD problem. One of these solutions is always the distance of the observer to the origin, which leads to the trivial solution of the observer determining its own orbit, this solution must be rejected. The problem of having multiple roots has been addressed analytically by Charlier [49] and Danby [50], who found that depending on the positions of the observer and the target with respect to the central body (i.e. Earth or Sun), four regions that determine the behavior of the problem can be identified. Following the illustration in Figure 5.1, the shaded regions A and C represent where the polynomial has two non-spurious solutions which might be both larger than the trivial solution (i.e. region C) or both smaller (ie. region A). As for the regions B and D they admit one single non-spurious solution.

When we consider the type of observations we are handling, we see that most of our

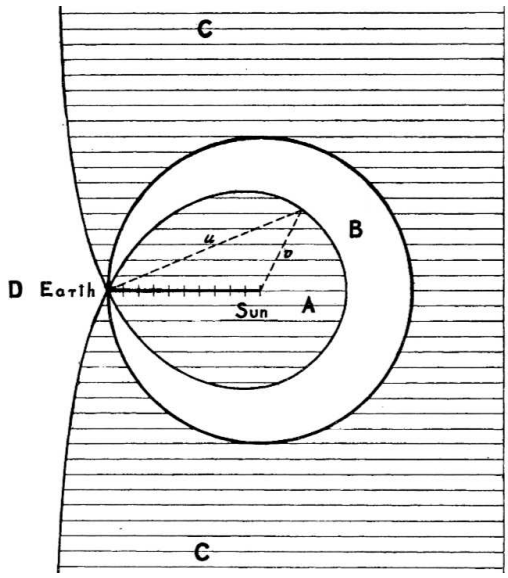

Figure 5.1: Charlier's Problem Classification. Taken from Charlier [49]. Regions A and C yield two non spurious roots to equation 5.44 while regions B and D produce a single one.

configurations lie in region C, since most observations concentrate on our observer's local horizon. For this reason we mostly find situations where we have our trivial root and two others. Here, we have attempted to follow the procedure proposed by Wie and Ahn [51] to choose the correct root after approximating the polynomial 5.44 to the form $r_2^8 - Ar_2^6$, meaning that an approximate value for the root would be $r_2 \approx \sqrt{|A|}$. However, we can identify that this procedure always estimates the larger of the two possible roots, and observing our targets from such a close distance, we are almost always finding that our correct root is the intermediate one. By applying Wie and Ahn's alternative approximation of the the polynomial $(r_2^8 - C)$, which is intended for long arcs, we get closer to our correct root. But as a safety measure we settle for using the *a priori* information of our targets, setting an estimate of the root based on the target's nominal altitude, which is then refined using the Newton-Raphson method.

5.1.3 Iterative Procedure

Gathering all the tools presented up to this point, we can now describe the algorithm that one should follow to solve the IOD problem using the original Gauss method. The first step is to produce the initial guess, which is done following the description on the previous subsection. The guessed ranges can be used directly to obtain initial values for the target's

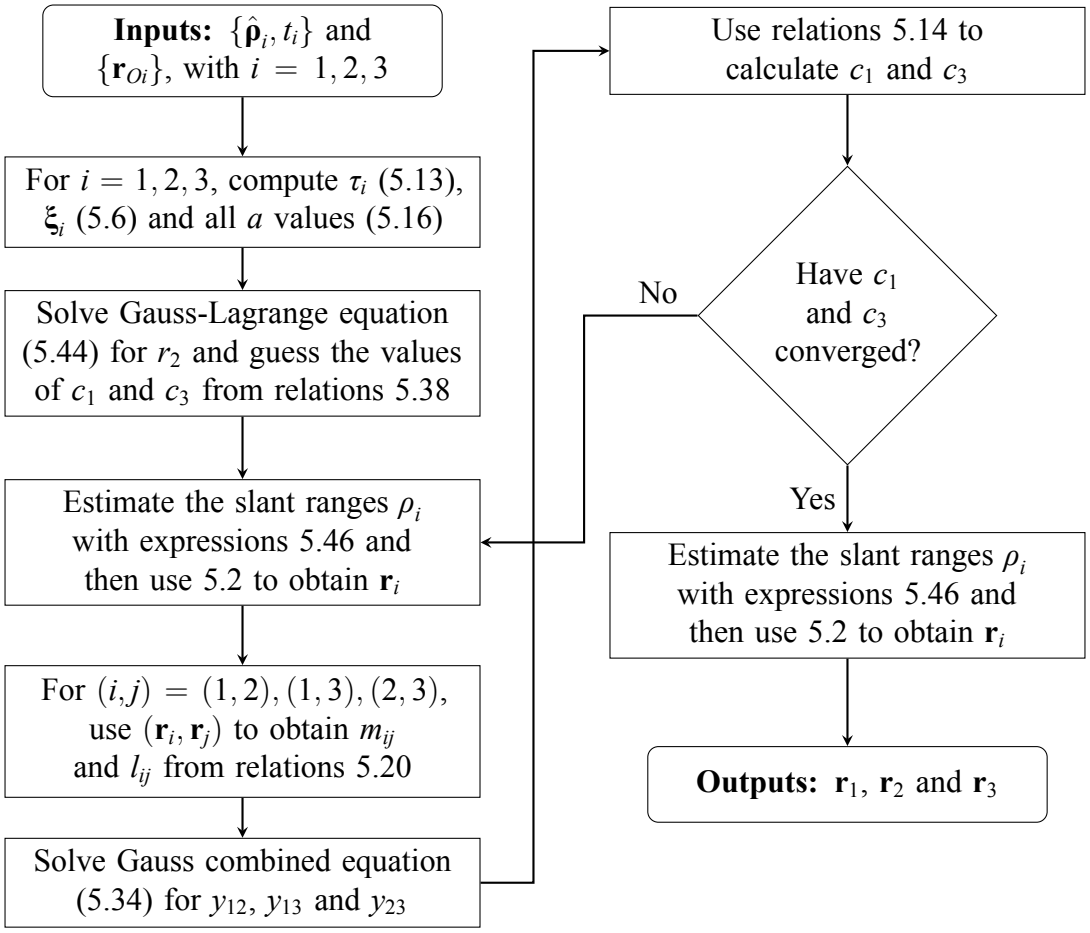

Figure 5.2: Gauss method. Classical Gauss method for IOD following an iterative procedure.

positions $\mathbf{r}_i$ by inserting them into the relationship in equation 5.2. From here, each one of the three pairs of distances $(\mathbf{r}_i, \mathbf{r}_j)$ is used to obtain values for m_{ij} and l_{ij} using the relations in 5.20 and correspondingly solve the combined equation of Gauss (Eq. 5.34) for each y_{12}, y_{13} and y_{23}. These values of the STTs can now be used in the relations 5.14 to improve the values of c_1 and c_3. Following this, the process is repeated since the new c values are used to improve the ranges with the equations 5.46. The loop is repeated until the c coefficients show no appreciable changes. This procedure is illustrated in the flow chart in Figure 5.2.

5.2 Gauss-Casotto Method

An alternative to the traditional method presented in the previous Section was presented by Casotto [46]. This new method is based on addressing the problem as a system of six non-linear equations with six unknowns. This is a more straightforward approach that might avoid some convergence problems that could arise when handling an iterative scheme based on the separation of loosely coupled equations, like the one we just presented. As previously addressed, the system would be composed by the three equations on 5.5 and three combined equations of Gauss for each STT. The following would be the vector of unknowns $\mathbf{z}$

$$\mathbf{z} = (\rho_1 \quad \rho_2 \quad \rho_3 \quad y_{12} \quad y_{13} \quad y_{23})^\top. \tag{5.49}$$

As established by the relations on 5.14, the three STTs can be reduced to two unknowns, making one of our six unknowns redundant. However, by leaving all six unknowns, the system looks symmetric and in a better form than it would if we were to represent it with five unknowns. The six by six system goes as follows

$$\boxed{\begin{aligned}
(\rho_1 + a_{11})y_{12}y_{13}\tau_3 - a_{12}y_{12}y_{23}\tau_2 - a_{13}y_{13}y_{23}\tau_1 &= 0 \\
a_{21}y_{12}y_{13}\tau_3 - (\rho_2 + a_{22})y_{12}y_{23}\tau_2 - a_{23}y_{13}y_{23}\tau_1 &= 0 \\
a_{31}y_{12}y_{13}\tau_3 - a_{32}y_{12}y_{23}\tau_2 - (\rho_3 + a_{33})y_{13}y_{23}\tau_1 &= 0 \\
y_{12}^2(y_{12} - 1) - m_{12}(\rho_1,\rho_2)W[y_{12}, l_{12}(\rho_1,\rho_2), m_{12}(\rho_1,\rho_2)] &= 0 \\
y_{13}^2(y_{13} - 1) - m_{13}(\rho_1,\rho_3)W[y_{13}, l_{13}(\rho_1,\rho_2), m_{13}(\rho_1,\rho_3)] &= 0 \\
y_{23}^2(y_{23} - 1) - m_{23}(\rho_2,\rho_3)W[y_{23}, l_{23}(\rho_1,\rho_2), m_{23}(\rho_2,\rho_3)] &= 0
\end{aligned}} \tag{5.50}$$

where the m and l auxiliary variables, as they were defined on 5.20, are both functions of the ranges since each range can be transformed in to a target's position vector via relation 5.2. Being a nonlinear system of equations, the solution can be found by an iterative method such as Newton-Raphson. For this, the full system on 5.50 is defined by the vector function $\mathbf{F}$ as

$$\mathbf{F}(\mathbf{z}) = \mathbf{0} \tag{5.51}$$

From it, partial derivatives with respect to the unknowns can be computed to produce the gradient vector function $\partial\mathbf{F}(\mathbf{z})/\partial\mathbf{z}$. Starting from an initial guess of the unknowns vector,

the solution is refined by applying the following scheme

$$\mathbf{z}_{n+1} = \mathbf{z}_n - \left(\left. \frac{\partial \mathbf{F}(\mathbf{z})}{\partial \mathbf{z}} \right|_{\mathbf{z}_n} \right)^{-1} \mathbf{F}(\mathbf{z}_n) \tag{5.52}$$

The gradient vector must be evaluated on the current values for $\mathbf{z}_n$ and the procedure continues until convergence is achieved. The initialization of this procedure can be done with the same first-order guess described earlier, particularly the values for $\mathbf{z}_0$ would come from relations 5.46 and 5.47. Alternatively to implementing the Newton-Raphson scheme by obtaining the analytical form of each partial derivative, other modern tools such as the symbolic equations solver offered by MATLAB (which we use in this work), allow for an efficient resolution of the system.

5.3 Analysis of the Results

The evaluation of this method is done by choosing 100 random observation windows from the Starlink data generated in Chapter 4 to evaluate the observer's orbit. We focus on the observations with respect to our already chosen SSO orbit at 450 km of altitude. The choice of the samples is done by keeping the proportions between the 5 inclination groups introduced on Section 3.1.1. The SGP4-generated data provide us with the initial conditions that we then numerically propagate with a given force model in order to produce the two additional measurements required to perform our method.

5.3.1 Length of Arc

The time separation between measurements is one of the most crucial aspects determining the convergence and accuracy of the Gauss method. In a work presented by Celletti and Pinzari [52], the Gauss method was applied to various objects from the asteroid belt and the Kuiper's belt. It was shown that while increasing the time intervals favored the success of the method for the Kuiper's objects, it did the opposite for the asteroids. This tells us that the behavior is not absolute so we must examine it for our case. Considering our proposed FOV and the expected angular velocities of the targets, the cadence rate of 6 seconds mentioned on the analysis in Chapter 4 is our starting point. However, we explore its vicinity by considering equally-spaced observations by intervals of 3, 6, 12 and 24 seconds. The errors presented in this Section are obtained by taking the estimated

position of the target at all three times, and comparing it to the true position using the true RTN frame. To gather a total error we calculate the root mean square (RMS) of all three positions in all 100 samples.

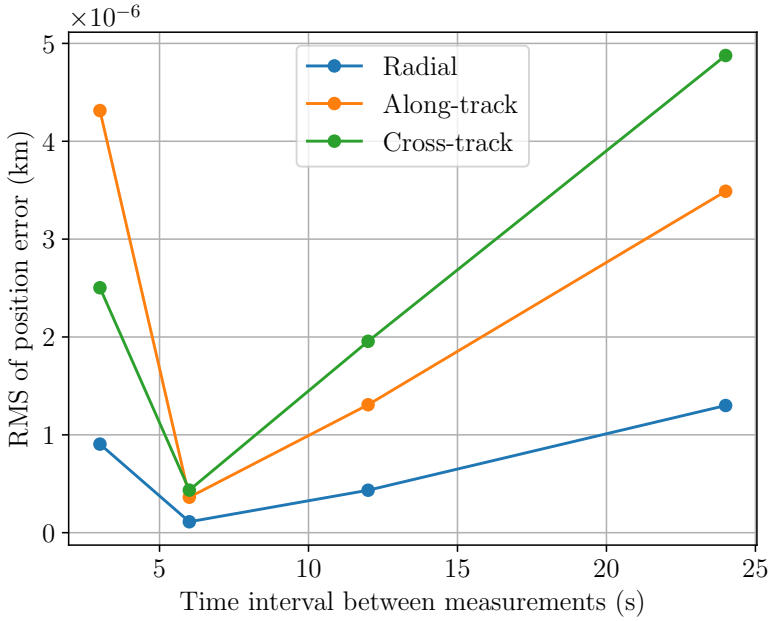

Figure 5.3: Gaussian Estimation Error on Keplerian Orbits. RMS error in the RTN frame with respect to the true trajectory, the gauss method is run over 3 equally separated measurements, changing the time interval.

To begin, we produce observations with the classical Keplerian model, and by running the method on all 100 samples we get the results presented in Figure 5.3. Here we see promising results, since the RMS of the errors is situated on the millimeter level for all three directions. Even for the runs where the time interval is 6 seconds, the error goes below the millimeter. One thing to mention about these results is the radial error being lower than the other two directions. Additionally, it is interesting to see how the error minimizes at a certain interval which is not on the extrema. This result supports the already mentioned findings of Celletti and Pinzari where it was seen that increasing or decreasing the observation interval does not directly imply if the method will perform better or worse. Moreover, this behavior also shows similarities to results presented by Dichter and Wojcik [53], where Monte Carlo simulations of ground-based observations on a LEO target are done with different observation time intervals and a regime where closer-spaced

observations may lead to more accurate solutions is identified.

Naturally, we would like to evaluate the performance in more realistic situations, so we begin by including the J2 perturbation in our numerically propagated synthetic scenario, from which we obtain the measured positions. By performing the same analysis we just did but with J2 perturbed orbits, we get the results in Figure 5.4 where the first notable difference with respect to the pure Keplerian (truth) orbits, is a significant increment of the RMS errors. Although the tendency of the radial component having a lower error than the rest is maintained, we are looking at errors around 100 km which is quite far from our desired accuracy. When looking at the data we can also see that it has a high dispersion so there are errors at orders of magnitude as high as 10^4 km and as low as 10^{-2} km. In any case, we can say that the Gauss method is not reliable for cases like these, where the perturbations to the Keplerian orbit are significant and we require higher precision.

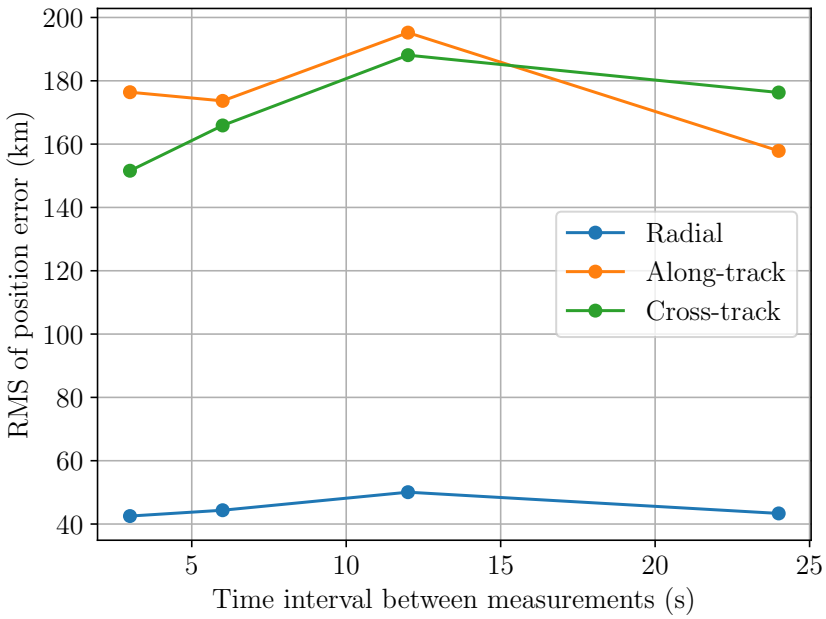

Figure 5.4: Gaussian Estimation Error on J2 Perturbed Orbits. RMS error in the RTN frame with respect to the true trajectory, the gauss method is applied on three equally separated measurements, changing the time interval.

5.3.2 Sensitivity Analysis

The effect of the J2 perturbation on the propagated positions reaches the order of 10^{-5} km after 3 seconds, and reaches the meter level (10^{-3} km) with the 24 second interval. In order to better understand how this changes amplify through the Gaussian method to the error levels we saw in Figure 5.4, we perform a sensitivity analysis. For this we choose observations separated by 6 seconds and start with the purely Keplerian positions. The positions are then independently corrupted with a random Gaussian noise with different levels on the standard deviation σ. After spanning a range of σ from 10^{-8} to 10^{-3} km, the IOD is performed 10 times for each member of the sample. The resulting RMS errors for each direction are presented in Figure 5.5.

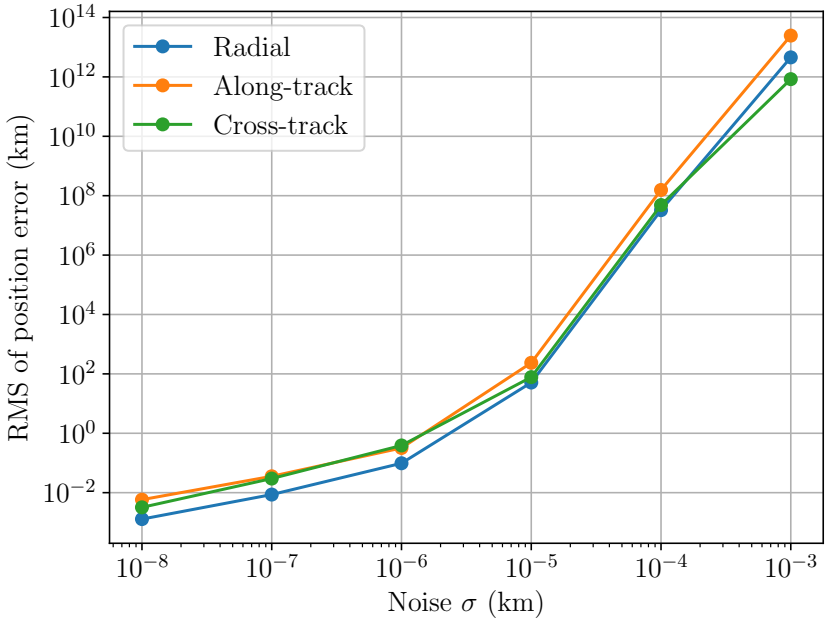

Figure 5.5: Sensitivity to Noise of Gaussian Estimation on Keplerian Orbits. RMS error in the RTN frame with respect to the true trajectory, the gauss method is applied on three measurements separated by 6 seconds, corrupting the Keplerian positions with different levels of noise.

As expected, the error increases along with the noise level, but it is relevant to point out how a sub millimetric noise level, as small as 10^{-8} km, already produces errors on the meter level. Then we observe an exponential growth and at the noise levels close to the known perturbation of J2, we see errors as high as 10^{12} km. From this, we have shown that in our observing configuration the Gauss method is highly sensitive to measurement errors

and even small departures from the Keplerian orbit, produce significant inaccuracies on the estimated state. This finding is also mentioned in the work by Dichter and Wojcik [53] and it suggests that realistic scenarios, where the full geopotential play a relevant role, must be dealt with methods different from the classical ones.

6

Statistical Orbit Determination

A more realistic approach to the orbit determination problem is to opt for a statistical method (SOD). The IOD method presented in t previous chapter, relied on the properties of an ideal Keplerian motion; although all orbital motions are dominated by these laws, in many situations additional perturbative forces are strong enough to become significant. In these cases, applying an IOD method produces high errors and a different approach is required. One of the main advantages of statistical orbit determination is the ability to fit any given force model to the available observations. In the case we are studying, which concerns LEO, we consider a J_2 perturbation as it was explained in section 2.1, the force model ruled by the potential in equation 2.14 can be fitted to a series of observations, for which we use the Least Squares method that we will describe in this chapter. The following procedures are based on those presented by Casotto [15] and Schutz et al. [54].

6.1 Linearization of the Model

To begin, we define $\mathbf{X}(t)$ as the n-dimensional dynamical state vector, built from both positions and velocities at a given time t as $\mathbf{X}(t) = (\mathbf{r}(t), \dot{\mathbf{r}}(t))^\top$. Naturally, our goal is to estimate this vector which in our case is six-dimensional, meaning that we can set $n = 6$. As mentioned previously, the evolution of the state vector is governed by the force model

F as

$$\dot{\mathbf{X}}(t) = \mathbf{F}(\mathbf{X}, \mathbf{P}, t), \tag{6.1}$$

where we have included the vector **P** which contains the constant parameters of the model. In our case **F** is given by the expression in 2.3, and following the potential in equation 2.14, the model parameters would be GM, J_2 and a_e. However, we will take the values given in table 2.1 as known and we will abstain from estimating them.

In contrast to the IOD methods presented previously, the SOD allows for a general set of observables that make up one observation. To describe the observations we have the p-dimensional vector $\mathbf{Y}_i = \mathbf{Y}(t_i)$, with $i = 1, ..., l$. This means that a total of l observations with p observable components are used. In general $p < n$ hence the need of more than one observation to produce an estimation. The requirement is given by $m > n$ with $m = p \times l$, in our case where we use angles-only measurements, meaning that $p = 2$ and $n = 6$ so as in the IOD case, we require at least 3 observations. The relationship between the observations and the dynamical state is given by the measurement model **G** as

$$\mathbf{Y}(t) = \mathbf{G}(\mathbf{X}, \mathbf{Q}, t) + \boldsymbol{\varepsilon}(t), \tag{6.2}$$

where the vector **Q** includes the geometrical parameters for the measurement model and $\boldsymbol{\varepsilon}$ encompasses the errors of each measurement. For angle-only, the measurement model comes from the relations mentioned in 2.30, where we can see that there are no geometrical parameters so we can neglect **Q**. Knowing that our observables are right ascension (α) and declination (δ) such that $\mathbf{Y}(t) = (\alpha(t), \delta(t))^\top$, we can explicitly write

$$\mathbf{G}(\mathbf{X}, t) = \begin{pmatrix} G_\alpha \\ G_\delta \end{pmatrix} = \begin{pmatrix} \text{atan2}(\hat{\rho}_j, \hat{\rho}_i) \\ \text{atan2}\left(\hat{\rho}_k, \sqrt{\hat{\rho}_i^2 + \hat{\rho}_j^2}\right), \end{pmatrix} \tag{6.3}$$

where we are taking the components of the LOS vector $\hat{\boldsymbol{\rho}}$, with $\boldsymbol{\rho}(t) = \mathbf{r}(t) - \mathbf{r}_O(t)$, and using the atan2 function to avoid placing the target on the wrong quadrant. The dependence to the dynamical state comes from using the target's position **r** to calculate $\boldsymbol{\rho}$. Clearly, the model also requires knowledge of the observer's position $\mathbf{r}_O$, and in fact this value can also be estimated using this method. In our case however, we will assume this to be well determined, since the onboard GNSS-navigation system of our observing platform may perform orbit determination with sub-decimeter accuracy, by using State Space Rep-

resentation (SSR) corrections as it has been shown by Darugna et al. [55].

To linearize the problem, we define $\mathbf{X}(t)$ as the target's true trajectory and $\mathbf{X}^*(t)$ as the reference trajectory, which perfectly follows the force model. From here, we introduce variations in the trajectory ($\delta\mathbf{X}$) and the measurements ($\delta\mathbf{Y}$), such that

$$\begin{aligned} \mathbf{X}(t) &= \mathbf{X}^*(\mathbf{P}, t) + \delta\mathbf{X}(t) \\ \mathbf{Y}(t) &= \mathbf{G}(\mathbf{X}^*, t) + \delta\mathbf{Y}(t). \end{aligned} \tag{6.4}$$

By assuming that $\delta\mathbf{X}$ is small, the force model can be expanded to first order as

$$\dot{\mathbf{X}}(t) = \mathbf{F}(\mathbf{X}^*, \mathbf{P}, t) + \left[\frac{\partial \mathbf{F}}{\partial \mathbf{X}}\right]^* \delta\mathbf{X}(t). \tag{6.5}$$

Similarly, the measurement model gets expanded to first order as

$$\mathbf{Y}_i = \mathbf{G}(\mathbf{X}^*, t_i) + \left[\frac{\partial \mathbf{G}}{\partial \mathbf{X}}\right]_i^* \delta\mathbf{X}(t_i) + \boldsymbol{\varepsilon}_i, \tag{6.6}$$

the partial derivatives are denoted with a $*$ meaning that they are evaluated on the reference trajectory. Furthermore, by writing

$$\dot{\mathbf{X}}^* = \mathbf{F}(\mathbf{X}^*, \mathbf{P}, t) \tag{6.7}$$

along with

$$\dot{\mathbf{X}} = \dot{\mathbf{X}}^* + \delta\dot{\mathbf{X}} \tag{6.8}$$

we can solve for the variations as

$$\begin{aligned} \delta\dot{\mathbf{X}}(t) &= \left[\frac{\partial \mathbf{F}}{\partial \mathbf{X}}\right]^* \delta\mathbf{X}(t) \\ \delta\mathbf{Y}_i &= \left[\frac{\partial \mathbf{G}}{\partial \mathbf{X}}\right]_i^* \delta\mathbf{X}(t_i) + \boldsymbol{\varepsilon}_i. \end{aligned} \tag{6.9}$$

For briefness, from now on we denote the variations with lower cases: $\mathbf{x} = \delta\mathbf{X}$, $\dot{\mathbf{x}} = \delta\dot{\mathbf{X}}$

and $\mathbf{y}_i = \delta\mathbf{Y}_i$. The previous equations can now be rewritten as

$$\begin{aligned} \dot{\mathbf{x}}(t) &= \mathrm{A}(t)\mathbf{x}(t) \\ \mathbf{y}_i &= \tilde{\mathrm{H}}_i\mathbf{x}_i + \boldsymbol{\varepsilon}_i \end{aligned} \tag{6.10}$$

where

$$\begin{aligned} \mathrm{A}(t) &= \left[\frac{\partial\mathbf{F}(t)}{\partial\mathbf{X}(t)}\right]^* \\ \tilde{\mathrm{H}}_i &= \left[\frac{\partial\mathbf{G}}{\partial\mathbf{X}}\right]_i^*. \end{aligned} \tag{6.11}$$

The calculation of $\mathrm{A}(t)$ will be discussed in t next Section along with the state transition matrix, but to obtain $\tilde{\mathrm{H}}_i$ we can directly differentiate the expressions in 6.3. As already mentioned, the measurement model $\mathbf{G}$ only depends to the positions $\mathbf{r}$ when considering its dependence on the dynamical state, hence $\tilde{\mathrm{H}}_i$ will have the following shape

$$\tilde{\mathrm{H}}_i = \begin{pmatrix} \frac{\partial G_\alpha}{\partial r_i} & \frac{\partial G_\alpha}{\partial r_j} & \frac{\partial G_\alpha}{\partial r_k} & 0 & 0 & 0 \\ \frac{\partial G_\delta}{\partial r_i} & \frac{\partial G_\delta}{\partial r_j} & \frac{\partial G_\delta}{\partial r_k} & 0 & 0 & 0 \end{pmatrix} \tag{6.12}$$

with the expressions for the derivatives in terms of the components of the LOS vector

$$\begin{aligned} \frac{\partial G_\alpha}{\partial r_i} &= -\frac{\hat{\rho}_j}{\hat{\rho}_i^2 + \hat{\rho}_j^2} & \frac{\partial G_\delta}{\partial r_i} &= -\frac{\hat{\rho}_k}{\hat{\rho}_i^2 + \hat{\rho}_j^2 + \hat{\rho}_k^2}\frac{\hat{\rho}_i}{\sqrt{\hat{\rho}_i^2 + \hat{\rho}_j^2}} \\ \frac{\partial G_\alpha}{\partial r_j} &= \frac{\hat{\rho}_i}{\hat{\rho}_i^2 + \hat{\rho}_j^2} & \frac{\partial G_\delta}{\partial r_j} &= -\frac{\hat{\rho}_k}{\hat{\rho}_i^2 + \hat{\rho}_j^2 + \hat{\rho}_k^2}\frac{\hat{\rho}_j}{\sqrt{\hat{\rho}_i^2 + \hat{\rho}_j^2}} \\ \frac{\partial G_\alpha}{\partial r_k} &= 0 & \frac{\partial G_\delta}{\partial r_k} &= \frac{\sqrt{\hat{\rho}_i^2 + \hat{\rho}_j^2}}{\hat{\rho}_i^2 + \hat{\rho}_j^2 + \hat{\rho}_k^2}. \end{aligned} \tag{6.13}$$

In order to apply a least squares scheme, we must relate a deviation in the *i*-th observation $\mathbf{y}_i$ with a deviation in the initial state $\mathbf{x}_0 = \mathbf{x}(t_0)$. For this, we begin by relating $\mathbf{x}_0$ to any $\mathbf{x}(t)$

$$\mathbf{x}(t) = \frac{\partial\mathbf{X}(t)}{\partial\mathbf{X}_0}\mathbf{x}_0. \tag{6.14}$$

The partial derivative that quantifies the sensitivity to perturbations in the initial state is

what we know as the *dynamical state transition matrix* $\Phi_{xx}(t,t_0)$. In general, this matrix along with the *parameter state transition matrix* $\Phi_{xp}(t,t_0)$ make up the *system state transition matrix* (STM) $\Phi(t,t_0)$. In our case, since we are neglecting the parameter variability, we can directly say that $\Phi(t,t_0) = \Phi_{xx}(t,t_0)$ and therefore

$$\mathbf{x}(t) = \Phi(t,t_0)\mathbf{x}_0. \tag{6.15}$$

From here, we reach an expression for the variation in the i-th observation

$$\mathbf{y}_i = \tilde{\mathrm{H}}_i\Phi(t_i,t_0)\mathbf{x}_0 + \boldsymbol{\varepsilon}_i. \tag{6.16}$$

In the end, by defining the matrix $\mathrm{H}_i = \tilde{\mathrm{H}}_i\Phi(t_i,t_0)$, we obtain the system

$$\mathbf{y}_i = \mathrm{H}_i(t_i,t_0)\mathbf{x}_0 + \boldsymbol{\varepsilon}_i, \quad i = 1,...,l \tag{6.17}$$

which can be used in a least squares scheme to estimate the initial state deviation $\mathbf{x}_0$.

6.1.1 State Transition Matrix Calculation

A fundamental step of this procedure is the non trivial task of calculating the STM. Although we have defined it as $\partial\mathbf{X}(t)/\partial\mathbf{X}_0$, this expression can not be evaluated explicitly. The procedure to be followed begins by taking the derivative of equation 6.1 with respect to the initial state

$$\frac{\partial\dot{\mathbf{X}}(t)}{\partial\mathbf{X}_0} = \left[\frac{\partial\mathbf{F}}{\partial\mathbf{X}}\right]^* \frac{\partial\mathbf{X}(t)}{\partial\mathbf{X}_0}. \tag{6.18}$$

Then we interchange the order of differentiation and substitute matrix A

$$\frac{d}{dt}\left(\frac{\partial\mathbf{X}(t)}{\partial\mathbf{X}_0}\right) = \mathrm{A}(t)\frac{\partial\mathbf{X}(t)}{\partial\mathbf{X}_0}. \tag{6.19}$$

Here we have reached a differential equation for the STM

$$\dot{\Phi}(t,t_0) = \mathrm{A}(t)\Phi(t,t_0), \quad \Phi(t_0,t_0) = \mathrm{I}. \tag{6.20}$$

Where the initial condition is trivially set as the identity matrix.

Taking our force model as given in equation 2.3, but labeling $\mathbf{v}$ for the first three entries

and $\mathbf{a}$ for the last three, we have $\mathbf{F} = (\mathbf{v}, \mathbf{a})^\top$. With this notation we can write matrix A, which is 6×6, in terms of four 3×3 sub-matrices as

$$\mathrm{A} = \begin{pmatrix} 0 & \mathrm{I} \\ \frac{\partial \mathbf{a}}{\partial \mathbf{r}} & \frac{\partial \mathbf{a}}{\partial \mathbf{v}}. \end{pmatrix} \tag{6.21}$$

By also subdividing the STM in the same way, we have

$$\Phi = \begin{pmatrix} \Phi_{rr} & \Phi_{rv} \\ \Phi_{vr} & \Phi_{vv} \end{pmatrix} \tag{6.22}$$

which allow as to write equation 6.20 as the system

$$\begin{aligned} \dot{\Phi}_{rr} &= \Phi_{vr}, & \dot{\Phi}_{rv} &= \Phi_{vv} \\ \dot{\Phi}_{vr} &= \frac{\partial \mathbf{a}}{\partial \mathbf{r}}\Phi_{rr} + \frac{\partial \mathbf{a}}{\partial \mathbf{v}}\Phi_{vr}, & \dot{\Phi}_{vv} &= \frac{\partial \mathbf{a}}{\partial \mathbf{r}}\Phi_{rv} + \frac{\partial \mathbf{a}}{\partial \mathbf{v}}\Phi_{vv} \end{aligned} \tag{6.23}$$

with initial conditions

$$\begin{aligned} \Phi_{rr}(t_0, t_0) &= \mathrm{I}, & \Phi_{rv}(t_0, t_0) &= 0 \\ \Phi_{vr}(t_0, t_0) &= 0, & \Phi_{vv}(t_0, t_0) &= \mathrm{I}. \end{aligned} \tag{6.24}$$

From here we are only missing the expressions to compute $\partial\mathbf{a}/\partial\mathbf{r}$ and $\partial\mathbf{a}/\partial\mathbf{v}$. By looking at the explicit components of $\mathbf{a}$, which are written in 2.15, we see no dependence on $\mathbf{v}$ so we can immediately set $\partial\mathbf{a}/\partial\mathbf{v} = 0$. As for $\partial\mathbf{a}/\partial\mathbf{r}$, we have the following symmetric matrix

$$\frac{\partial \mathbf{a}}{\partial \mathbf{r}} = \begin{pmatrix} U_{xx} & U_{xy} & U_{xz} \\ U_{xy} & U_{yy} & U_{yz} \\ U_{xz} & U_{yz} & U_{zz} \end{pmatrix}. \tag{6.25}$$

Whose explicit entries come from taking the derivatives of the expressions in 2.15 with

respect to each position component and result in

$$
\begin{aligned}
U_{xx} &= -\frac{GM}{r^5}\left\{r^2 - 3r_i^2 + \frac{3}{2}J_2 a_e^2\left[1 - 5\left(\frac{r_i}{r}\right)^2 - 5\left(\frac{r_k}{r}\right)^2 + 35\left(\frac{r_k r_i}{r^2}\right)^2\right]\right\} \\
U_{xy} &= 3\frac{GMr_i r_j}{r^5}\left\{1 - \frac{J_2}{2}\left(\frac{a_e}{r}\right)^2\left[35\left(\frac{r_k}{r}\right)^2 - 5\right]\right\} \\
U_{xz} &= 3\frac{GMr_i r_k}{r^5}\left\{1 - \frac{J_2}{2}\left(\frac{a_e}{r}\right)^2\left[35\left(\frac{r_k}{r}\right)^2 - 15\right]\right\} \\
U_{yy} &= -\frac{GM}{r^5}\left\{r^2 - 3r_j^2 + \frac{3}{2}J_2 a_e^2\left[1 - 5\left(\frac{r_j}{r}\right)^2 - 5\left(\frac{r_k}{r}\right)^2 + 35\left(\frac{r_k r_j}{r^2}\right)^2\right]\right\} \\
U_{yz} &= 3\frac{GMr_j r_k}{r^5}\left\{1 - \frac{J_2}{2}\left(\frac{a_e}{r}\right)^2\left[35\left(\frac{r_k}{r}\right)^2 - 15\right]\right\} \\
U_{zz} &= -\frac{GM}{r^5}\left\{r^2 - 3r_k^2 + \frac{3}{2}J_2 a_e^2\left[3 - 30\left(\frac{r_k}{r}\right)^2 + 35\left(\frac{r_k}{r}\right)^4\right]\right\}.
\end{aligned}
\tag{6.26}
$$

The common practice is to integrate the STM simultaneously as the dynamical state. Therefore, by using the already mentioned ODE solver [17], the integration of six equations is expanded to 36 more for a total of 42.

6.2 Weighted Least Squares Estimate

One of the most popular methods, which is actually a more general form of the standard least squares method, is the *weighted least squares* (WLS). The problem to be solved is presented in the form that we reached in equation 6.17 with the addition of a weights matrix W

$$
\mathbf{y} = \mathrm{H}\mathbf{x}_0 + \boldsymbol{\varepsilon}, \quad \mathrm{W} \tag{6.27}
$$

where considering a set of l observations, we would have

$$
\mathbf{y} = \begin{pmatrix} \mathbf{y}_1 \\ \mathbf{y}_2 \\ \vdots \\ \mathbf{y}_l \end{pmatrix}, \quad \mathrm{H} = \begin{pmatrix} \mathrm{H}_1 \\ \mathrm{H}_2 \\ \vdots \\ \mathrm{H}_l \end{pmatrix}, \quad \boldsymbol{\varepsilon} = \begin{pmatrix} \boldsymbol{\varepsilon}_1 \\ \boldsymbol{\varepsilon}_2 \\ \vdots \\ \boldsymbol{\varepsilon}_l \end{pmatrix}, \quad \mathrm{W} = \begin{pmatrix} \mathrm{w}_1 & 0 & \dots & 0 \\ 0 & \mathrm{w}_2 & 0 & \vdots \\ \vdots & 0 & \ddots & 0 \\ 0 & \dots & 0 & \mathrm{w}_l \end{pmatrix}. \tag{6.28}
$$

As previously mentioned, $\mathbf{y}$ and $\boldsymbol{\varepsilon}$ have dimensions $m \times 1$ whereas $\mathbf{x}_0$ has $n \times 1$ and H maps both vectors so it has a shape of $m \times n$. Recalling that $m = p \times l$, where p is the number of observables in one observations, we must ensure that p or l are large enough to fulfill the condition of $m > n$. Regarding W, this is a block diagonal matrix where each sub matrix is given by the inverse of the *covariance matrix* of the measurement errors $\mathrm{w}_i = \mathrm{R}_i^{-1}$, where the covariance matrix is defined as $\mathrm{R}_i = E[\boldsymbol{\varepsilon}_\mathbf{i}\boldsymbol{\varepsilon}_\mathbf{i}^\top]$.

The goal of WLS is to find an estimate $\hat{\mathbf{x}}_0$ of $\mathbf{x}_0$ by minimizing the sum of the weighted squares, which is given by the following *performance index*

$$J(\mathbf{x}_0) = \frac{1}{2}\boldsymbol{\varepsilon}^\top \mathrm{W}\boldsymbol{\varepsilon} = \sum_{i=1}^{l} \frac{1}{2}\boldsymbol{\varepsilon}_i^\top \mathrm{w}_i \boldsymbol{\varepsilon}_i. \tag{6.29}$$

By replacing $\boldsymbol{\varepsilon}$ from equation 6.27, we get

$$J(\mathbf{x}_0) = \frac{1}{2}(\mathbf{y} - \mathrm{H}\mathbf{x}_0)^\top \mathrm{W}(\mathbf{y} - \mathrm{H}\mathbf{x}_0). \tag{6.30}$$

The minimization is achieved by taking the derivative with respect to $\mathbf{x}_0$ and setting it equal to zero

$$\frac{\partial J}{\partial \mathbf{x}_0} = -(\mathbf{y} - \mathrm{H}\mathbf{x}_0)^\top \mathrm{WH} \tag{6.31}$$

so $\hat{\mathbf{x}}_0$ is found from

$$\mathrm{H}^\top \mathrm{W}(\mathbf{y} - \mathrm{H}\hat{\mathbf{x}}_0) = \mathbf{0} \tag{6.32}$$

which can be rearranged in to the *normal equations* of a least squares formulation

$$(\mathrm{H}^\top \mathrm{WH})\hat{\mathbf{x}}_0 = \mathrm{H}^\top \mathrm{W}\mathbf{y} \tag{6.33}$$

where $\mathrm{H}^\top \mathrm{WH}$ is identified as the *normal matrix*, if this is positive definite, it will have an inverse and the estimate will be

$$\hat{\mathbf{x}}_0 = (\mathrm{H}^\top \mathrm{WH})^{-1}\mathrm{H}^\top \mathrm{W}\mathbf{y}. \tag{6.34}$$

A non weighted least squares would be equivalent to the one just presented, but considering W as the identity matrix.

When available, an *a priori* estimate of $\mathbf{x}_0$, denoted as $\bar{\mathbf{x}}_0$, along with its associated weighting matrix $\bar{\mathrm{W}}$ can be inserted into the performance index as

$$J(\mathbf{x}_0) = \frac{1}{2}(\mathbf{y} - \mathrm{H}\mathbf{x}_0)^\top \mathrm{W}(\mathbf{y} - \mathrm{H}\mathbf{x}_0) + \frac{1}{2}(\bar{\mathbf{x}}_0 - \mathbf{x}_0)^\top \bar{\mathrm{W}}(\bar{\mathbf{x}}_0 - \mathbf{x}_0). \tag{6.35}$$

This would then result in the estimate taking the following form

$$\hat{\mathbf{x}}_0 = (\mathrm{H}^\top \mathrm{W}\mathrm{H} + \bar{\mathrm{W}})^{-1}(\mathrm{H}^\top \mathrm{W}\mathbf{y} + \bar{\mathrm{W}}\bar{\mathbf{x}}_0). \tag{6.36}$$

6.2.1 Batch Processor

From the theory of the WLS method presented in t previous Section, we now move the actual algorithm that allows us to implement the method in our observations. The batch processor consists of applying WLS to a set (*batch*) of measurements after they have all been collected in a certain time span. An alternative to this would be a *sequential* processor, which would obtain a new updated estimate after each measurement is acquired.

To implement it we assume that we have a set of initial conditions $\mathbf{X}_0^*$ and an *a priori* estimate of the deviation $\bar{\mathbf{x}}_0$ with an associates error covariance matrix $\bar{\mathrm{P}}_0$ that yields $\bar{\mathrm{W}} = \bar{\mathrm{P}}_0^{-1}$. Recalling also $\mathrm{W} = \mathrm{R}^{-1}$, equation 6.36 is expressed as

$$(\mathrm{H}^\top \mathrm{R}^{-1}\mathrm{H} + \bar{\mathrm{P}}_0^{-1})\hat{\mathbf{x}}_0 = \mathrm{H}^\top \mathrm{R}^{-1}\mathbf{y} + \bar{\mathrm{P}}_0^{-1}\bar{\mathbf{x}}_0. \tag{6.37}$$

Here we must refer on how to accumulate both the normal matrix and the one containing the observations, i.e.

$$\mathrm{H}^\top \mathrm{R}^{-1}\mathrm{H} = \sum_{i=1}^{l} [\tilde{\mathrm{H}}_i \Phi(t_i, t_0)]^\top \mathrm{R}_i^{-1} \tilde{\mathrm{H}}_i \Phi(t_i, t_0) \tag{6.38}$$

$$\mathrm{H}^\top \mathrm{R}^{-1}\mathbf{y} = \sum_{i=1}^{l} [\tilde{\mathrm{H}}_i \Phi(t_i, t_0)]^\top \mathrm{R}_i^{-1} \mathbf{y}_i. \tag{6.39}$$

The initial state vector $\mathbf{X}_0^*$ is to be used to obtain the STM and $\tilde{\mathrm{H}}$ as it was described in Section 6.1.1 and relation 6.12 respectively. After solving the normal equations and finding a value for $\hat{\mathbf{x}}_0$, the state vector is updated by adding the estimation i.e. $(\mathbf{X}_0^*)_n =$

$(\mathbf{X}_0^*)_{n-1} + (\hat{\mathbf{x}}_0)_{n-1}$. From here, the process is repeated for the new state vector, resulting in an iterative process. Since the *a priori* estimate must be considered as an additional piece of information along with the measurements, the quantity $\mathbf{X}_0^* + \bar{\mathbf{x}}_0$ must be kept the same on each iteration. For this reason, we can establish

$$\begin{aligned} (\mathbf{X}_0^*)_n + (\bar{\mathbf{x}}_0)_n &= (\mathbf{X}_0^*)_{n-1} + (\bar{\mathbf{x}}_0)_{n-1} \\ (\mathbf{X}_0^*)_{n-1} + (\hat{\mathbf{x}}_0)_{n-1} + (\bar{\mathbf{x}}_0)_n &= (\mathbf{X}_0^*)_{n-1} + (\bar{\mathbf{x}}_0)_{n-1} \end{aligned} \tag{6.40}$$

meaning that $\bar{\mathbf{x}}_0$ gets updated as

$$(\bar{\mathbf{x}}_0)_n = (\bar{\mathbf{x}}_0)_{n-1} - (\hat{\mathbf{x}}_0)_{n-1}. \tag{6.41}$$

The iterative process is continued until convergence is achieved, typically verified when the RMS changes negligibly. The RMS is defined as

$$\mathrm{RMS} = \left[\frac{\sum_{i=1}^{l} \hat{\boldsymbol{\varepsilon}}_i^\top \mathrm{R}_i^{-1} \hat{\boldsymbol{\varepsilon}}_i}{m} \right]^{1/2} \tag{6.42}$$

where, as usual $m = p \times l$ and $\hat{\boldsymbol{\varepsilon}}_i$ is given by

$$\hat{\boldsymbol{\varepsilon}}_i = \mathbf{y}_i - \mathrm{H}_i \hat{\mathbf{x}}_0. \tag{6.43}$$

Although the method can be defined assuming that there are no observations on t_0 which is the timestamp of the state we want to estimate, we will follow a procedure that we have an observation for this time. In addition to this, we will also use the common practice of choosing $\mathbf{X}_0^*$ such that $\bar{\mathbf{x}}_0 = \mathbf{0}$, hence $\bar{\mathrm{P}}_0$* represents the relative accuracy of the elements on the initial condition vector $\mathbf{X}_0^*$. A visual representation of the followed algorithm is shown in the flowchart in Figure 6.1.

6.3 Initial Estimation with Least Squares

Following the unsatisfactory results of the IOD method presented in Chapter 5 for the estimation of non-purely Keplerian orbits, we here attempt the initial estimation using three observations in a batch LS processor. To test the least squares estimation, we per-

*If no *a priori* information exists, set to $\bar{\mathrm{P}}_0^{-1} = 0$

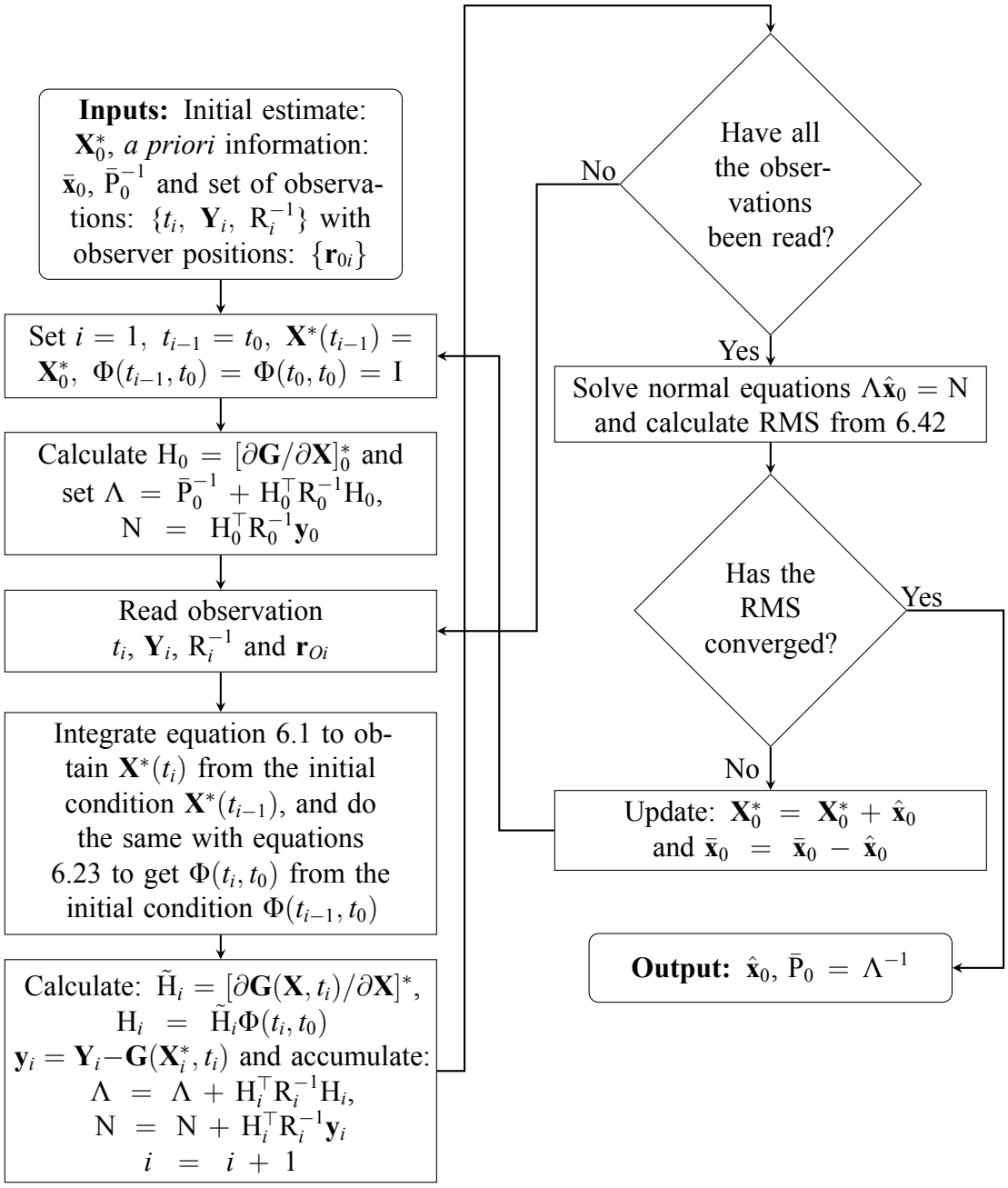

Figure 6.1: Algorithm for the batch processor. The algorithm describes how to implement a batch processor for a weighted least squares method as described in Section 6.2.1.

form the same time interval analysis done with IOD, on the same samples. For this case, we consider the zonal potential up to J_6 as the true model, while we fit the simplified J_2 model. The results are presented in Figure 6.2, where in addition to the position error, we also include the velocity error as it is part of the estimated state.

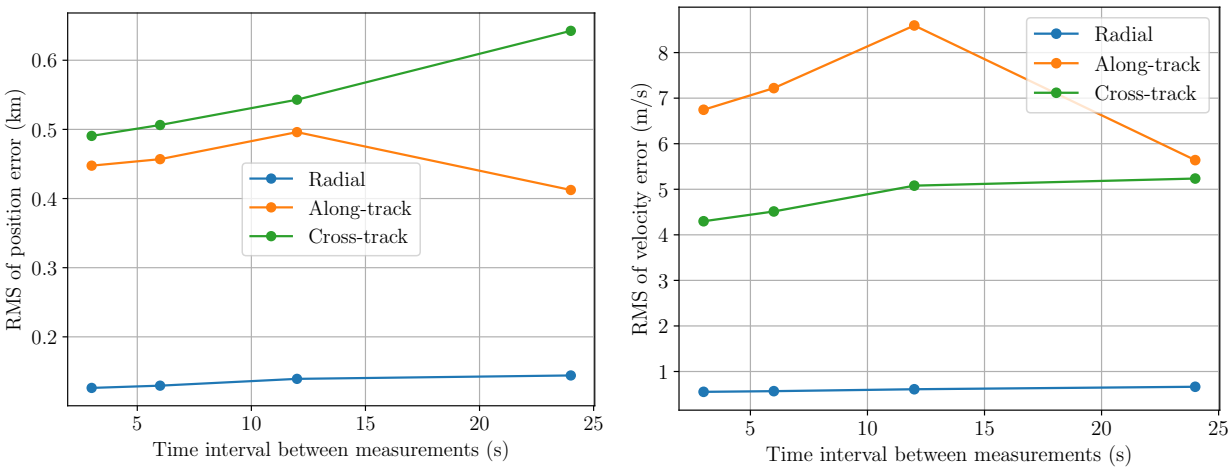

(a) Position errors.

(b) Velocity errors.

Figure 6.2: Least Squares Estimation Errors. RMS errors in the RTN frame with respect to the true trajectory. The J_2 model is fitted to three equally separated measurements, generated with the J_6 model, changing the time interval.

As seen in Figure 6.2, the errors are less than one kilometer, which is acceptable, and there is no relevant dependence on the time interval. As for the velocity errors, they are also well within acceptable boundaries, being in the meter per second level. As in IOD, considering our FOV size we also maintain the 6 second interval for the following results.

6.3.1 Effect of Measurement Errors

Similarly to how it was presented for IOD, we would like to understand the sensitivity of this method to the inevitable measurement errors. In contrast to the IOD case, where we corrupted the data with random Gaussian noise in the target's positions, here we corrupt the angular measurements (i.e. α and δ). To do so, we must consider some characteristics we have mentioned about our instrument.

As it was mentioned, our FOV is formed by a cone with a diameter of 4°, by then assuming that we would use a large 4096 $\times$ 4096 sensor, we would have a pixel instan-

taneous FOV (iFOV) of around 3.5 arc-seconds. With this information, the question of how precise can the angular measurements be, becomes how precise can we determine the position of the edge of our streaks, within a pixel in our detector. To understand this limit, we consider some of the main sources of error in astrometric measurements. To begin, due to the fact we are dealing with space-based observations, we can neglect all sources of error that come from atmospheric effects. Ignoring also the already mentioned relativistic effects such as aberration, and assuming that the effects of the spacecraft motion can be accounted for, we are left with the following main sources of error:

- Shot Noise: Poisson process associated with the discrete, particle-like nature of light.
- Flat Field: Calibration of the non-uniform responsiveness across the detector due to imperfections and other instrumental effects.
- Geometric Distortion: Optical aberration that must be handled with the pixel area correction.
- PSF (Point Spread Function) Model: An accurate model must be known to ensure the accuracy in the estimation of its center.

Recent papers such as Griggio et al. [56] and Libralato et al. [57], demonstrate how optimal conditions in a space-based telescope such as the JWST allow astrometric precisions close to 0.01 pixels. For our case however, we might prefer to be conservative, and assume that having short exposures, our signal to noise ratio (SNR) will be low. This would result in difficulties to control these errors and more realistically we would ideally achieve a precision closer to 0.1 pixels. With this in mind, and considering our lack of knowledge regarding the full description of our potential instrument, we opt to model the angular error with a Gaussian random noise acting independently on α and δ, changing the value of σ from 0.1 to 10^{-4} pixels. The results after 200 trials on each target are shown in Figure 6.3a with the noise σ in arc-seconds. Observing the results, it appears that a precision of 0.1 pixels produces large errors ($> 10^4$ km) while the ideal precision of 0.01 pixels keeps them below 100 km. In order to achieve errors under the kilometer level, a precision close to 10^{-4} pixels, which are around 0.35 mas considering our FOV.

An additional measurement error is the one associated to assigning a correct timestamp to each measurement. Considering the way streaks would form in our images, the straightforward assignment of the timestamps would correspond to the opening and closing times

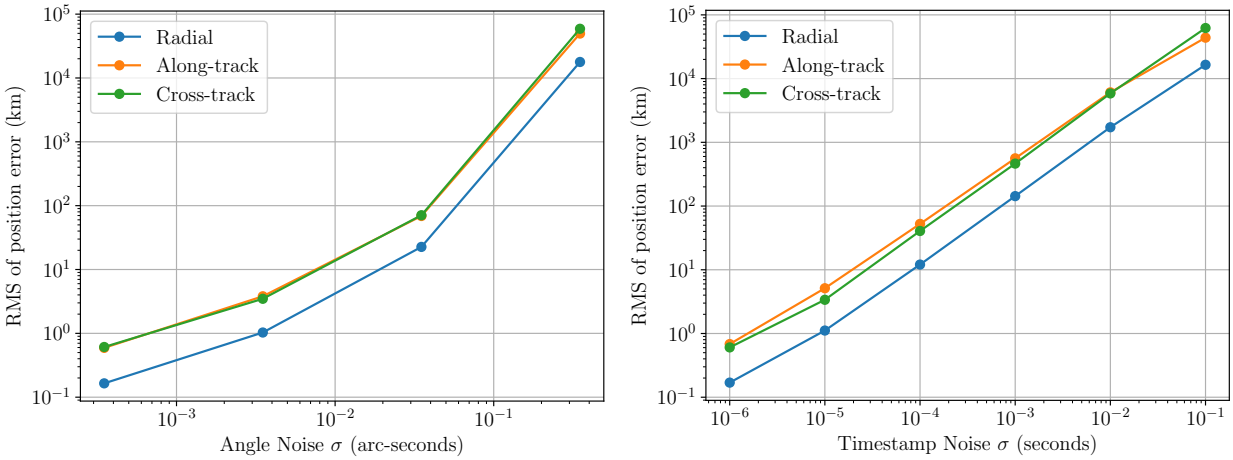

(a) Angle Noise.

(b) Timestamp Noise.

Figure 6.3: LS Estimation Errors with Noise on Measurements. RMS errors in the RTN frame with respect to the true trajectory. The J_2 model is fitted to three corrupted measurements separated by 6 seconds, generated with the J_6 model.

of the shutter. High precision of the knowledge of these times is not normally a need in most astronomical applications, hence instruments are usually not designed to offer this. Considering the fact that LEO satellites can move 1 km in a little over 0.1 seconds, we certainly would require a lower precision than this value. Achieving this, would likely involve a detailed study on the shutter mechanism, since depending on the way it uncovers the sensor, the different regions start being illuminated at different moments. To visualize the effects of this uncertainty, we perform the same Gaussian noise perturbation, but only for the observation times. Noise levels are evaluated from $\sigma = 0.1$ seconds, all the way to 1 microsecond, the results are shown in Figure 6.3b. In this case the subkilometric accuracy is only obtained for a σ of 1 microsecond. A similar study of these effects was conducted for ground-based IOD by Van den Abbeele [58] showing similar behavior.

6.4 Using More Than Three Observations for Estimation

A clear advantage of the least squares method over the Gaussian, is the ability to use more than three measurements to produce an estimate. In order to understand how the inclusion of more measurements affects the results, we consider the situation where the telescope acts on tracking mode and is capable to follow the target, taking up to 60 measurements with a cadence of 6 seconds. For the results in this Section and the one that follows, we

reduce our sample to 15 satellites that are well behaved and have guaranteed observation windows every half orbit for at leas 2 full orbits. Without any noise in the measurements, we obtain the results in Figure 6.4a. The same procedure with corrupted measurements using a σ of 0.01 pixels in angle and 1 microsecond in the timestamps as an RMS of 200 trials for each target yield the results in Figure 6.4b.

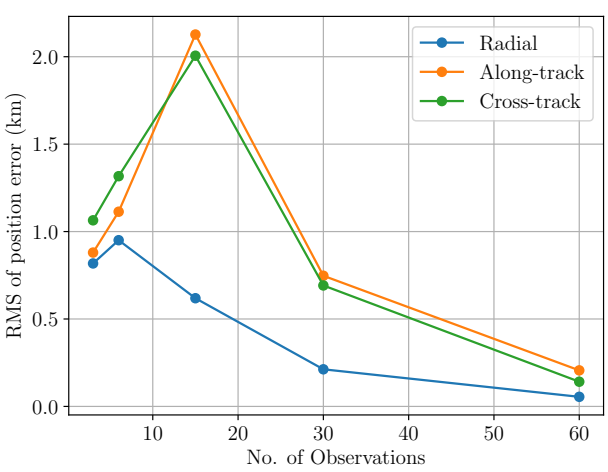

(a) Without Noise.

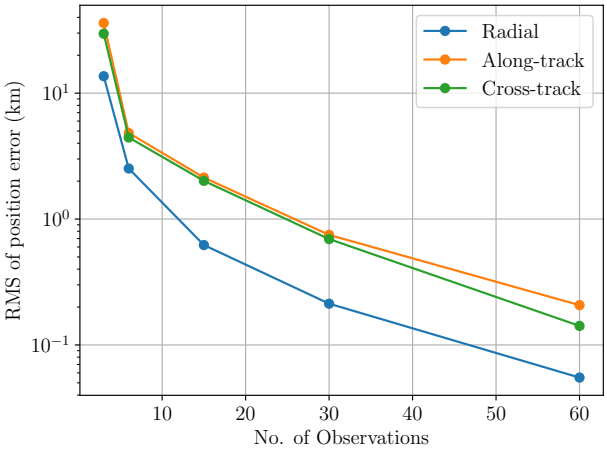

(b) With Angle Noise $\sigma = 0.035$ arc-seconds and Timestamp $\sigma = 10^{-6}$ seconds.

Figure 6.4: LS Estimation Errors with More than One Set of Three Measurements. RMS errors in the RTN frame with respect to the true trajectory. The J_2 model is fitted to multiple measurements separated by 6 seconds, generated with the J_6 model.

By looking at Figure 6.4 we see that in general, increasing the number of observations reduces the errors of the estimation. For the noise-free measurements, although there is an initial increment in the errors maximizing at 15 observations, at 60 it goes below 200 meters. On the contrary, with the noisy data, the errors continuously decrease as observations are added. At 15 observations errors go below 5 km and with 30 observations they are below 1 km, a level that suits safe distance for collision avoidance.

As mentioned in Section 4.1.4, follow-up observation of a given target are important to confirm and improve previous estimates. We now wish to evaluate the performance of the method when including measurements taken on different observations windows. We choose to take the three initial measurements and incorporate three new measurements after every half orbit, when the target is visible again. The task is executed on noise-free data separated by half an orbit and up to two full orbits. The results, shown in Figure 6.5

show that by including the second set of measurements, half an orbit after the initial, the errors decrease with and without noise. This suggests that the larger separation between this sets provides more significant information for the estimation. However, after this improvement, errors start to climb again as new sets are included. A logical explanation is that we are still fitting a J_2 model to data generated with a J_6 model, and as the orbits are propagated, the discrepancy between both models grows, making the data more difficult to fit.

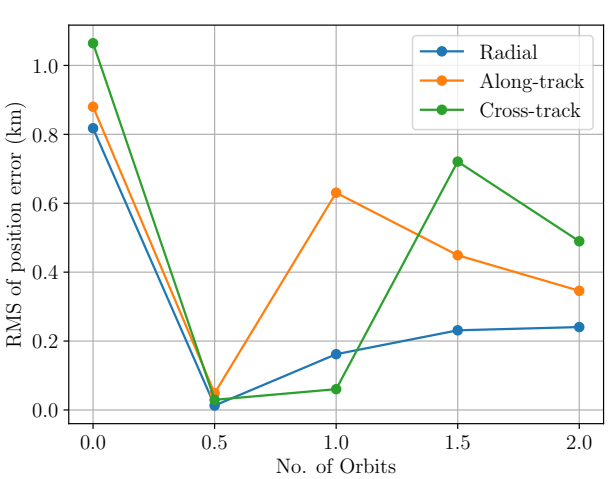

(a) Without Noise.

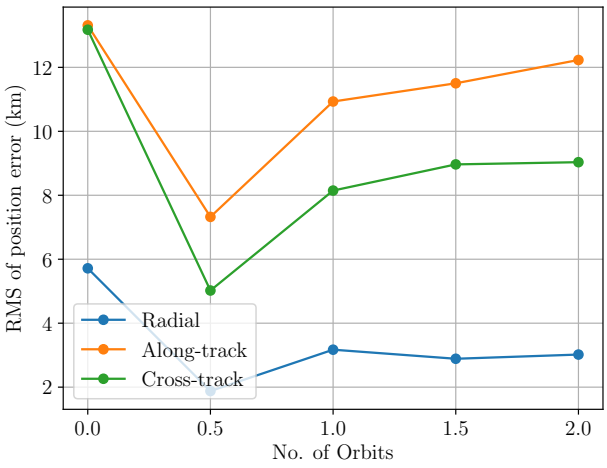

(b) With Angle Noise $\sigma = 0.035$ arc-seconds and Timestamp $\sigma = 10^{-6}$ seconds.

Figure 6.5: LS Estimation Errors with Measurements Separated by Half an Orbit. RMS errors in the RTN frame with respect to the true trajectory. The J_2 model is fitted to multiple observation windows (separated by half an orbit) of three measurements each, separated by 6 seconds, and generated with the J_6 model.

Although it would not be wise to fit many measurements separated by multiple orbits, the estimations are bound to improve when they are separated by half orbits or one full orbit.

6.4.1 Streak Association

A problem that arises when more than one observation window is used for an estimation, is the track to track association, also known as the linkage problem. The problem comes from the fact that assigning a given track, or in our case streak, to an already known target, although unnecessary in our simulations, is a non trivial task in real life. A wide variety

of methods have been developed in order to deal with this problem. Some common approaches are Bayesian and probabilistic methods such as those presented by Bar-Shalom and Blair [59]. Also, a method based on the use of two-body integrals to constrain the linkage between two short arcs was presented by Gronchi et al. [60]. More recent approaches involve the use of Machine Learning methods. Although the linkage problem is outside of the scope of this work, it is worth mentioning its relevance for future developments.

6.5 Propagation of The Covariance Matrix

As described at the beginning of this chapter, the weight matrix W used in the WLS method is obtained by inverting the associated covariance matrix of the measurements R^{-1}. When dealing with independent, angles-only measurements, we set a covariance matrix formed by a 2×2 identity matrix scaled by our measurement's uncertainty (i.e. 0.01 pixels or 0.035 arc-seconds) squared. Although the choice of this uncertainty results irrelevant to the obtained estimation, it directly affects the error covariance matrix $\bar{\mathrm{P}}_0$ that results from inverting the accumulated normal matrix of the problem (i.e. $\Lambda = \sum_i \mathrm{H}_i^\top \mathrm{W}_i \mathrm{H}_i$). The $\bar{\mathrm{P}}_0$ matrix represents the relative accuracy of the estimated state, but we can also propagate this matrix to a future time $\bar{\mathrm{P}}_k$ see how the relative accuracy of the estimate would evolve.For this, we begin by writing $\bar{\mathrm{P}}_k$ as

$$\bar{\mathrm{P}}_k = E[(\bar{\mathbf{x}}_k - \mathbf{x}_k)(\bar{\mathbf{x}}_k - \mathbf{x}_k)^\top]. \tag{6.44}$$

Considering the way the estimated variation is propagated

$$\bar{\mathbf{x}}_k = \Phi(t_k, t_0)\hat{\mathbf{x}}_0, \tag{6.45}$$

we can rewrite equation 6.44 as

$$\bar{\mathrm{P}}_k = E[\Phi(t_k, t_0)(\bar{\mathbf{x}}_0 - \hat{\mathbf{x}}_0)(\bar{\mathbf{x}}_0 - \hat{\mathbf{x}}_0)^\top \Phi^\top(t_k, t_0)]. \tag{6.46}$$

Finally, the STM being deterministic can be factored from the expected value, leaving the following expression

$$\bar{\mathrm{P}}_k = \Phi(t_k, t_0)\bar{\mathrm{P}}_0 \Phi^\top(t_k, t_0). \tag{6.47}$$

Given this, the covariance matrix of an estimate can be propagated along with the esti-

mate by integrating the STM additionally to the state vector.

To visualize this evolution in our estimations, we propagate the covariance matrix for a full orbit of the targets. The matrix is then transformed to the RTN frame for each time, which leaves the variance on each direction on the matrix diagonal. Therefore, taking the square root of the diagonal terms yields the standard deviation in each direction which can also be interpreted as the axes of the covariance ellipsoid, which is a representation of the target's position uncertainty. Without scaling it, the covariance ellipsoid establishes the target's position with a confidence level of 1-σ or 68.27%. Comparing the FOV size to the propagated ellipsoid's size helps determine the likelihood of observing the target at its expected location. When observing the results in Figure 6.6, we can see that while the radial and cross-track axes seem to oscillate in size, the along-track axis grows significantly.

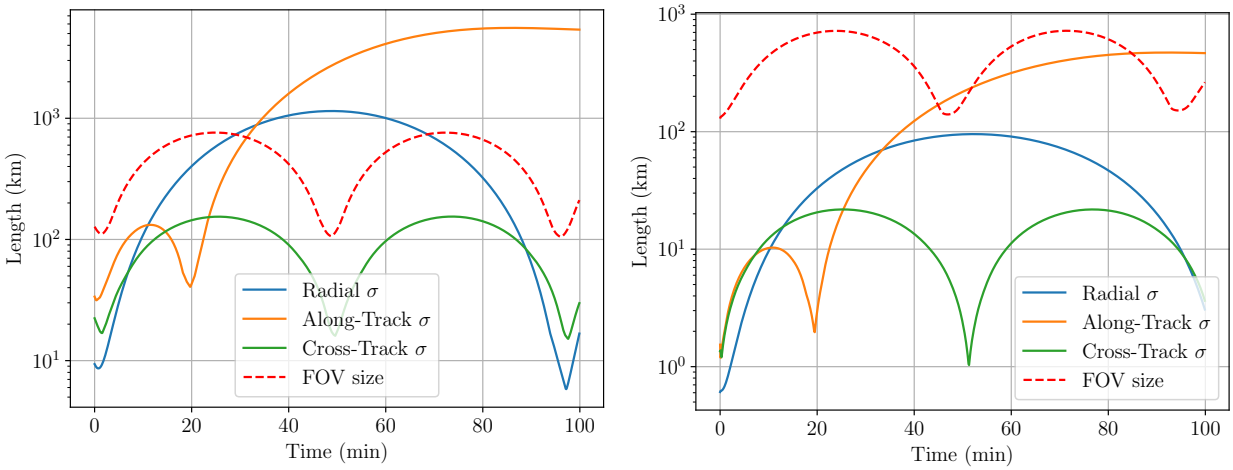

(a) Estimate using 3 measurements.

(b) Estimate using 9 measurements.

Figure 6.6: Propagation of Covariance Ellipsoid Axes. With a measurement uncertainty of 0.035 arcseconds, the covariance ellipsoid is propagated for a full orbit and compared to the diameter of the FOV at the target's location. Troughs in the FOV size represent close encounter where measurements can be performed.

In Figure 6.6a from an estimate using 3 measurements, we observe the evolution of the Covariance ellipsoid axes through time compared with the diameter of the FOV at the target's position. From what can be seen, the position of the target would be too uncertain to fall inside the FOV after half an orbit, but if the initial estimate is done with 9 measurements, as shown in Figure 6.6b, it is much more likely. Naturally with more

than 9 measurements, the uncertainty is further reduced, but if the observer is limited to only three measurements, then the measurement uncertainty would have to be lower than 0.0035 arc-seconds which corresponds to 0.001 pixels, and its is difficult to achieve with present technology.

7
Conclusions

Throughout the study here conducted, an optical SBSS satellite with a FOV of $4° \times 4°$ was simulated for the detection and orbit determination of LEO RSOs. The constraints that allow the observation of a target were described and considered in the design of a suitable orbit for an observer aiming at the Starlink constellation. From this orbit, the IOD Gauss method, along with a WLS implemented through a batch processor were evaluated on the Starlink targets. The following is an outline of the findings of this research:

- The propagation of the Starlink full constellation for 48 hours, using SGP4, allowed the evaluation of multiple possible orbits for the observer. In the end, the best performance in terms of number of valid observations and coverage of the constellation was obtained through a circular SSO at 450 km of altitude.

- Using the same procedure, an optimal pointing direction for the surveillance of the constellation's vicinity was determined. By using inertial pointing, an anti-solar direction was found to be optimal, while using a body-fixed pointing, the best direction was found to be inside the plane formed by the radial and along-track axes, 8° below the local horizon.

- When testing the Gauss method on multiple observing situations, highly accurate results were obtained when the propagated trajectories were purely Keplerian, achieving a minimum error below 1 millimeter when the observations were separated by 6 sec-

onds. This is a validation of the goodness of the model and the code implementation. However, the introduction of the J_2 perturbation yielded large errors, and a sensitivity analysis showed how even alterations of centimeter level to the Keplerian orbits resulted in errors in the order of hundreds of meters after the IOD.

- To prevent these errors, a batch processor was implemented to perform a WLS estimation. When fitting a J_2 model to three measurements, propagated using zonal perturbations up to the J_6 term, the errors were kept below 1 kilometer. Nevertheless, when considering the possible effects of measurement errors, the accuracy of the estimation drops, presenting errors on the order of tens of kilometers in position.
- A way of successfully lowering these errors is by including more measurements to the batch, or extending the observation interval. It was seen that processing 15 observations was enough to have errors below 5 km. The inclusion of measurements from different observation windows also proved to contribute to better estimations, but when using measurements separated by more than one orbit, there was a rising trend in the errors. This increase was likely caused by the growing divergence between the true model and the fitted one.
- Finally, an analysis of the propagated covariance matrix was performed. Interpreting this matrix as a covariance ellipsoid enabled an estimation of how measurement quality influenced the certainty of locating the target within a specific volume at a given time. It was found that for a precision of 0.01 pixels (35 mas) in the angle, at least nine measurements are required in order to find the target inside the FOV after half an orbit. As for the possibilities of achieving this with only three observations, it was found that the precision requirement is of 0.001 pixels (3.5 mas).

7.1 Future Work

Considering the broadness of this research field, there are multiple aspects to be considered in further studies.

- To begin, a better modeling of the observation errors would be required to improve the understanding of the system limitations. This may involve the complete design of the instrument, including its optical system and sensor. Simulating images could be valuable for examining streak effects and analyzing how their edges would be processed.

- Improving the true force model would be desired in order to resemble reality. This would include the use of a more complete geopotential field and the inclusion of additional perturbing forces such as residual drag, radiation pressure, and the effect of other bodies. However, the chosen model must balance accuracy with computational efficiency to enable rapid onboard integration.
- Evaluating the use of sequential processing, also known as Kalman filtering, instead of a batch processor is advised since for real applications it results more convenient. This is the case because the Kalman filter is more computationally efficient, analyzing the latest measurements in order to update the estimates in real time.
- Another improvement to the work would be to consider longer term simulations. This would give the possibility of analyzing the optimization of the observation procedures. By defining protocols to efficiently decide what targets to track or what regions to perform surveillance on, we could understand the capabilities of such a system not only for LEO, but for other orbital regimes. This type of analysis is also relevant for expanding to multiple observers and studying the SBSS system as a satellite constellation.

References

[1] J. Utzmann and A. Wagner, "Sbss demonstrator: A space-based telescope for space surveillance and tracking," *International Astronautical Federation: Paris, France*, 2015.

[2] Z. Zhang, G. Zhang, J. Cao, C. Li, W. Chen, X. Ning, and Z. Wang, "Overview on space-based optical orbit determination method employed for space situational awareness: From theory to application," in *Photonics*, vol. 11, no. 7. MDPI, 2024, p. 610.

[3] D. C. Harrison and J. C. Chow, "The space-based visible sensor," *Johns Hopkins APL Technical Digest*, vol. 17, no. 2, p. 227, 1996.

[4] J. Sharma, G. H. Stokes, C. von Braun, G. Zollinger, and A. J. Wiseman, "Toward operational space-based space surveillance," *Lincoln Laboratory Journal*, vol. 13, no. 2, pp. 309–334, 2002.

[5] L. M. Simms, W. D. Vries, V. Riot, S. S. Olivier, A. Pertica, B. J. Bauman, D. Phillion, and S. Nikolaev, "Space-based telescopes for actionable refinement of ephemeris pathfinder mission," *Optical Engineering*, vol. 51, no. 1, pp. 011 004–011 004, 2012.

[6] R. Scott, B. Wallace, D. Bedard *et al.*, *Space-based observations of satellites from the most microsatellite*. Citeseer, 2006.

[7] P. Maskell and L. Oram, "Sapphire: Canada's answer to space-based surveillance of orbital objects," in *Advanced Maui Optical and Space Surveillance Conference*, 2008.

[8] V. Abbasi, S. Thorsteinson, D. Balam, J. Rowe, D. Laurin, L. Scott, and M. Doyon, "The neossat experience: 5 years in the life of canada's space surveillance telescope," in *1st NEO and Debris Detection Conference*, vol. 22, 2019.

[9] J. Virtanen, J. Poikonen, T. Säntti, T. Komulainen, J. Torppa, M. Granvik, K. Muinonen, H. Pentikäinen, J. Martikainen, J. Näränen *et al.*, "Streak detection and analysis pipeline for space-debris optical images," *Advances in Space Research*, vol. 57, no. 8, pp. 1607–1623, 2016.

[10] M. Michel, H. Ceeh, J. Utzmann, and S. Kraft, "The space-based optical component (sboc) instrument for passive optical in-situ detection of small space debris," *LPI Contributions*, vol. 2852, p. 6130, 2023.

[11] J. Rainbow, "Vyoma orders pilot satellites for debris-monitoring constellation," Aug 2023. [Online]. Available: https://spacenews.com/vyoma-orders-pilot-satellites-for-debris-monitoring-constellation/

[12] G. Sciré, F. Santoni, and F. Piergentili, "Analysis of orbit determination for space based optical space surveillance system," *Advances in Space Research*, vol. 56, no. 3, pp. 421–428, 2015.

[13] F. Stechowsky, S. Setty, and A. Pastor, "Achievable orbit estimation accuracy through space-based passive optical observations: a sensor requirement analysis," in *2nd NEO and Debris Detection Conference*, 2023, p. 11.

[14] D. Spiller, E. Magionami, V. Schiattarella, F. Curti, C. Facchinetti, L. Ansalone, and A. Tuozzi, "On-orbit recognition of resident space objects by using star trackers," *Acta Astronautica*, vol. 177, pp. 478–496, 2020.

[15] S. Casotto, *Lecture Notes on Celestial Mechanics*. University of Padua, 2022.

[16] H. Schaub and J. L. Junkins, *Analytical mechanics of space systems*. Aiaa, 2003.

[17] L. F. Shampine, "Computer solution of ordinary differential equations," *The initial value problem*, 1975.

[18] B. D. Tapley, M. Watkins, J. Ries, G. Davis, R. Eanes, S. Poole, H. Rim, B. Schutz, C. Shum, R. S. Nerem *et al.*, "The joint gravity model 3," *Journal of Geophysical Research: Solid Earth*, vol. 101, no. B12, pp. 28 029–28 049, 1996.

[19] M. Lane, "The development of an artificial satellite theory using a power-law atmospheric density representation," in *2nd Aerospace Sciences Meeting*, 1965, p. 35.

[20] M. H. Lane and F. R. Hoots, "General perturbations theories derived from the 1965 lane drag theory," *NASA STI/Recon Technical Report N*, vol. 80, p. 23347, 1979.

[21] F. R. Hoots, "Spacetrack report no. 3, models for propagation of norad element sets," *http://www. itc. nl/-bakker/orbit. html*, 1980.

[22] D. Brouwer, "Solution of the problem of artificial satellite theory without drag," *Astronomical Journal, Vol. 64, p. 378 (1959)*, vol. 64, p. 378, 1959.

[23] F. R. Hoots, P. W. Schumacher Jr, and R. A. Glover, "History of analytical orbit modeling in the us space surveillance system," *Journal of Guidance, Control, and Dynamics*, vol. 27, no. 2, pp. 174–185, 2004.

[24] D. Vallado, P. Crawford, R. Hujsak, and T. Kelso, "Revisiting spacetrack report# 3," in *AIAA/AAS Astrodynamics Specialist Conference and Exhibit*, 2006, p. 6753.

[25] DMA, "The department of defense world geodetic system 1984, its definition and relationships with local geodetic systems." *DMA Technical Report*, 1991.

[26] D. A. Vallado, *Fundamentals of astrodynamics and applications*. Springer Science & Business Media, 2001, vol. 12.

[27] T. Kelso, "Validation of sgp4 and is-gps-200d against gps precision ephemerides, 17th aas," in *AIAA Spaceflight Mechanics Conference, Sedona, AZ, USA*, 2007.

[28] J. Seago and D. Vallado, "Coordinate frames of the us space object catalogs," in *Astrodynamics Specialist Conference*, 2000, p. 4025.

[29] IAU SOFA Board, "Iau sofa software collection." [Online]. Available: http://www.iausofa.org

[30] B. W. Carroll and D. A. Ostlie, *An introduction to modern astrophysics*. Cambridge University Press, 2017.

[31] G. A. McCue, J. G. Williams, and J. M. Morford, "Optical characteristics of artificial satellites," *Planetary and Space Science*, vol. 19, no. 8, pp. 851–868, 1971.

[32] H. N. Russell, "On the albedo of the planets and their satellites," *Proceedings of the National Academy of Sciences*, vol. 2, no. 2, pp. 74–77, 1916.

[33] M. Liu, H. Wang, H. Yi, Y. Xue, D. Wen, F. Wang, Y. Shen, and Y. Pan, "Space debris detection and positioning technology based on multiple star trackers," *Applied Sciences*, vol. 12, no. 7, p. 3593, 2022.

[34] S. Casotto, "The equations of relative motion in the orbital reference frame," *Celestial Mechanics and Dynamical Astronomy*, vol. 124, no. 3, pp. 215–234, 2016.

[35] T. Pultarova and E. Howell, "Starlink satellites: Facts, tracking and impact on astronomy," Apr 2022. [Online]. Available: https://www.space.com/spacex-starlink-satellites.html

[36] J. C. McDowell, "The low earth orbit satellite population and impacts of the spacex starlink constellation," *The Astrophysical Journal Letters*, vol. 892, no. 2, p. L36, 2020.

[37] T. S. Kelso, "Norad gp element sets current data," Apr 2024. [Online]. Available: https://celestrak.org/NORAD/elements/

[38] J. G. Walker, "Satellite constellations," *Journal of the British Interplanetary Society*, vol. 37, p. 559, 1984.

[39] J. McDowell, "Jonathan's space report," 2019. [Online]. Available: https://planet4589.org/

[40] G. D. Krebs, "Gunter's space page," 2024. [Online]. Available: https://space.skyrocket.de/

[41] R. J. Boain, "A-b-cs of sun-synchronous orbit mission design," *Proc. 14th AAS/AIAA Space Flight Mech. Conf*, 2004.

[42] A. Iemole, "Spacex launches first mission to third shell of starlink constellation - nasaspaceflight.com," Jul 2022. [Online]. Available: https://www.nasaspaceflight.com/2022/07/starlink-3-1/

[43] SpaceX, "Application for fixed satellite service by space exploration holdings, llc," Aug 2019. [Online]. Available: https://fcc.report/IBFS/SAT-MOD-20190830-00087/1877764.pdf

[44] M. Oswald, S. Stabroth, and A. Wagner, "Satellite-based solutions for beyond-leo space surveillance," in *5th European Space Debris Conference. Darmstadt, Germany: European Space Agency*, 2009.

[45] H. Yunpeng, L. Kebo, L. Yan'gang, and C. Lei, "Review on strategies of space-based optical space situational awareness," *Journal of Systems Engineering and Electronics*, vol. 32, no. 5, pp. 1152–1166, 2021.

[46] S. Casotto, "A new approach to gaussian initial orbit determination," *Adv. Astron. Sci*, vol. 152, pp. 1313–1336, 2014.

[47] H. Bucerius, "Vorlesungen ueber himmelsmechanik; vol. 1," *Mannheim: Bibliographisches Institut*, 1966.

[48] O. Montenbruck and T. Pfleger, *Astronomy on the personal computer*. Springer, 2013.

[49] C. V. Charlier, "Orbits, on multiple solutions in the determination of orbits from three observations," *Monthly Notices of the Royal Astronomical Society, Vol. 71, p. 120*, vol. 71, p. 120, 1910.

[50] J. Danby and T. Teichmann, *Fundamentals of celestial mechanics*. American Institute of Physics, 1963.

[51] B. Wie and J. Ahn, "On selecting the correct root of angles-only initial orbit determination equations of lagrange, laplace, and gauss," *The Journal of the Astronautical Sciences*, vol. 64, pp. 50–71, 2017.

[52] A. Celletti and G. Pinzari, "Dependence on the observational time intervals and domain of convergence of orbital determination methods," in *Periodic, Quasi-Periodic and Chaotic Motions in Celestial Mechanics: Theory and Applications: Selected papers from the Fourth Meeting on Celestial Mechanics, CELMEC IV San Martino al Cimino (Italy), 11–16 September 2005*. Springer, 2006, pp. 327–344.

[53] M. J. Dichter and J. J. Wojcik, "Characterizing the convergence behavior of gauss's method of initial orbit determination," *Journal of Guidance, Control, and Dynamics*, vol. 43, no. 5, pp. 998–1002, 2020.

[54] B. Schutz, B. Tapley, and G. H. Born, *Statistical orbit determination*. Elsevier, 2004.

[55] F. Darugna, S. Casotto, M. Bardella, M. Sciarratta, and P. Zoccarato, "Sub-decimeter onboard orbit determination of leo satellites using ssr corrections: A galileo-based case study for the sentinel-6a satellite," *Remote Sensing*, vol. 14, no. 23, p. 6121, 2022.

[56] M. Griggio, D. Nardiello, and L. Bedin, "Photometry and astrometry with jwst-ii: Nircam distortion correction," *Astronomische Nachrichten*, vol. 344, no. 3, p. e230006, 2023.

[57] M. Libralato, I. Argyriou, D. Dicken, M. G. Marín, P. Guillard, D. C. Hines, P. J. Kavanagh, S. Kendrew, D. R. Law, A. Noriega-Crespo *et al.*, "High-precision astrometry and photometry with the jwst/miri imager," *Publications of the Astronomical Society of the Pacific*, vol. 136, no. 3, p. 034502, 2024.

[58] B. van den Abbeele, "Initial orbit determination using angle measurements: Comparing iod methods on very short arc observations of geo objects from the meerlicht telescope," *Delft University of Technology*, 2021.

[59] Y. Bar-Shalom and W. D. Blair, *Multitarget-multisensor tracking: applications and advances*, 1992.

[60] G. F. Gronchi, L. Dimare, and A. Milani, "Orbit determination with the two-body integrals," *Celestial Mechanics and Dynamical Astronomy*, vol. 107, pp. 299–318, 2010.

Appendices

A

Zonal Terms of the Geopotential

The following expressions taken from Schaub and Junkins [16], are used in equation 2.16 to express the partial derivatives of a zonal geopotential.

$$\mathbf{a}_{J_2} = -\frac{3}{2}J_2\left(\frac{GM}{r^2}\right)\left(\frac{a_e}{r}\right)^2\begin{pmatrix}\left(1-5\left(\frac{r_k}{r}\right)^2\right)\frac{r_i}{r}\\ \left(1-5\left(\frac{r_k}{r}\right)^2\right)\frac{r_j}{r}\\ \left(3-5\left(\frac{r_k}{r}\right)^2\right)\frac{r_k}{r}\end{pmatrix} \tag{A.1}$$

$$\mathbf{a}_{J_3} = \frac{1}{2}J_3\left(\frac{GM}{r^2}\right)\left(\frac{a_e}{r}\right)^3\begin{pmatrix}5\left(7\left(\frac{r_k}{r}\right)^3-3\left(\frac{r_k}{r}\right)\right)\frac{r_i}{r}\\ 5\left(7\left(\frac{r_k}{r}\right)^3-3\left(\frac{r_k}{r}\right)\right)\frac{r_j}{r}\\ 3\left(1-10\left(\frac{r_k}{r}\right)^2+\frac{35}{3}\left(\frac{r_k}{r}\right)^4\right)\end{pmatrix} \tag{A.2}$$

$$\mathbf{a}_{J_4} = \frac{5}{8} J_4 \left(\frac{GM}{r^2} \right) \left(\frac{a_e}{r} \right)^4 \begin{pmatrix} \left(3 - 42 \left(\frac{r_k}{r} \right)^2 + 63 \left(\frac{r_k}{r} \right)^4 \right) \frac{r_i}{r} \\ \left(3 - 42 \left(\frac{r_k}{r} \right)^2 + 63 \left(\frac{r_k}{r} \right)^4 \right) \frac{r_j}{r} \\ \left(51 - 70 \left(\frac{r_k}{r} \right)^2 + 63 \left(\frac{r_k}{r} \right)^4 \right) \frac{r_k}{r} \end{pmatrix} \tag{A.3}$$

$$\mathbf{a}_{J_5} = \frac{1}{8} J_5 \left(\frac{GM}{r^2} \right) \left(\frac{a_e}{r} \right)^5 \begin{pmatrix} 3 \left(35 \left(\frac{r_k}{r} \right) - 210 \left(\frac{r_k}{r} \right)^3 + 231 \left(\frac{r_k}{r} \right)^5 \right) \frac{r_i}{r} \\ 3 \left(35 \left(\frac{r_k}{r} \right) - 210 \left(\frac{r_k}{r} \right)^3 + 231 \left(\frac{r_k}{r} \right)^5 \right) \frac{r_j}{r} \\ \left(693 \left(\frac{r_k}{r} \right)^6 - 945 \left(\frac{r_k}{r} \right)^4 + 315 \left(\frac{r_k}{r} \right)^2 - 15 \right) \end{pmatrix} \tag{A.4}$$

$$\mathbf{a}_{J_6} = -\frac{1}{16} J_6 \left(\frac{GM}{r^2} \right) \left(\frac{a_e}{r} \right)^6 \begin{pmatrix} \left(35 - 945 \left(\frac{r_k}{r} \right)^2 + 3465 \left(\frac{r_k}{r} \right)^4 - 3003 \left(\frac{r_k}{r} \right)^6 \right) \frac{r_i}{r} \\ \left(35 - 945 \left(\frac{r_k}{r} \right)^2 + 3465 \left(\frac{r_k}{r} \right)^4 - 3003 \left(\frac{r_k}{r} \right)^6 \right) \frac{r_j}{r} \\ \left(245 - 2205 \left(\frac{r_k}{r} \right)^2 + 4851 \left(\frac{r_k}{r} \right)^4 - 3003 \left(\frac{r_k}{r} \right)^6 \right) \frac{r_k}{r} \end{pmatrix} \tag{A.5}$$

B

Orbital Planes in the Starlink Constellation

Group 1 is shown in figure 3.4.

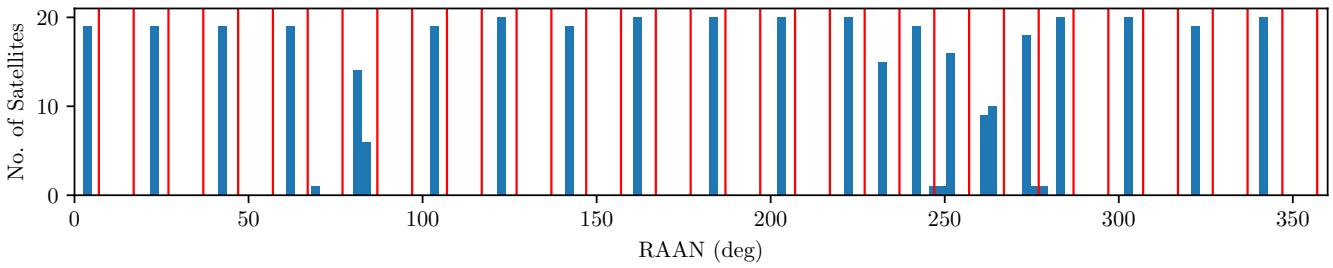

Figure B.1: Group 2 RAAN histogram. Group 2 Stalink satellites, which correspond to an inclination of 70°, are divided according to their RAAN in to orbital planes, a total of 36 equally spaced orbital planes are found, of which 21 are occupied with an average of $\sim$ 18 satellites each.

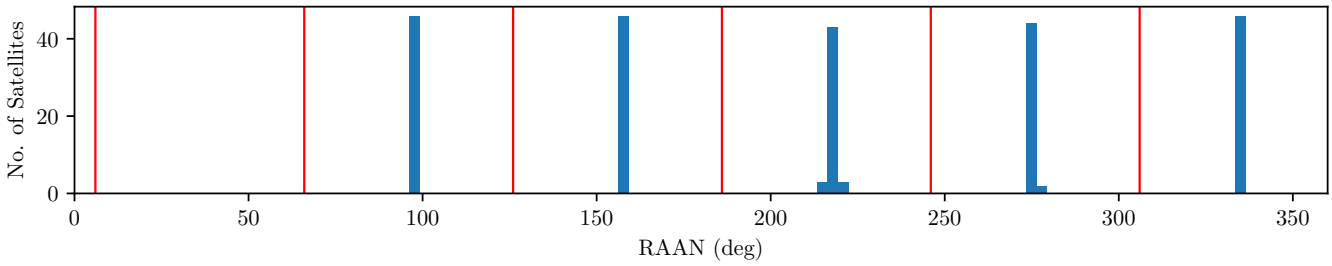

Figure B.2: Group 3 RAAN histogram. Group 3 Stalink satellites, which correspond to an inclination of 97.66°, are divided according to their RAAN in to orbital planes, a total of 6 equally spaced orbital planes are found, of which 5 are occupied with an average of $\sim$ 47 satellites each.

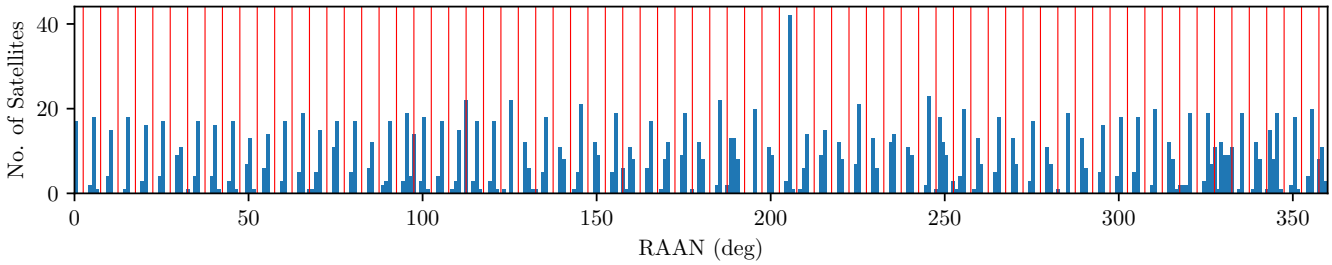

Figure B.3: Group 4 RAAN histogram. Group 4 Stalink satellites, which correspond to an inclination of 53.21°, are divided according to their RAAN in to orbital planes, a total of 72 equally spaced orbital planes are found with an average of $\sim$ 22 satellites each.

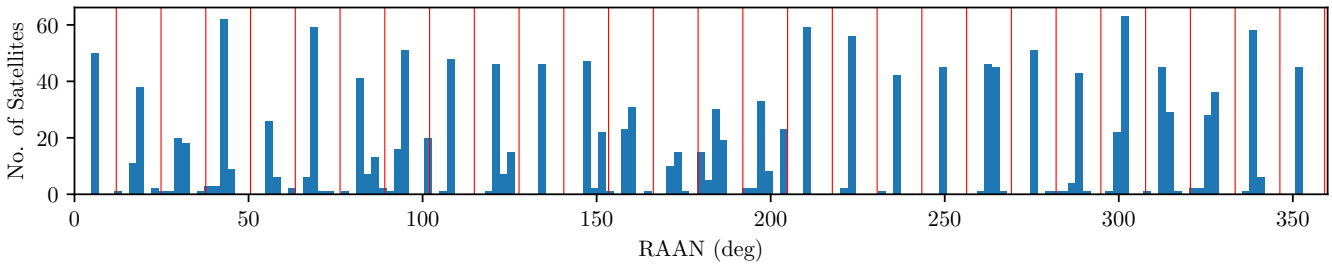

Figure B.4: Group 5 RAAN histogram. Group 5 Stalink satellites, which correspond to an inclination of 43°, are divided according to their RAAN in to orbital planes, a total of 28 equally spaced orbital planes are found with an average of $\sim$ 60 satellites each.